**Czech Technical University in Prague**

**Faculty of Nuclear Sciences and Physical Engineering**

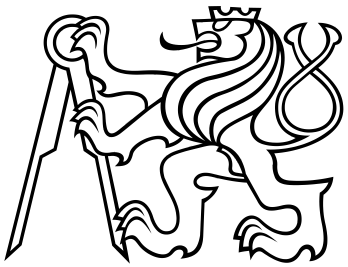

# DISSERTATION

# Modification of bandgap materials by ultra-short laser pulses

Prague 2023 Juraj Sládek

## Bibliografický záznam

| | |
|---|---|
| Autor práce: | Ing. Juraj Sládek,<br>České vysoké učení technické v Praze,<br>Fakulta jaderná a fyzikálně inženýrská,<br>Katedra inženýrství pevných látek |
| Název práce: | Modifikace materiálů se zakázaným pásem pomocí ultrakrátkych laserových pulzů |
| Studijní program: | Aplikace přírodních věd |
| Studijní obor: | Fyzikální inženýrství |
| Školitel: | prof. Ing. Zdeněk Bryknar, CSc.<br>České vysoké učení technické v Praze,<br>Fakulta jaderná a fyzikálně inženýrská,<br>Katedra inženýrství pevných látek |
| Školitel specialista: | Dr. Yoann Levy<br>Fyzikální ústav AV ČR, v. v. i.,<br>HiLASE Centrum |
| Akademický rok: | 2022/2023 |
| Počet stran: | 130 |
| Klíčová slova: | femtosekundový laser, křemík, laserem vyvolané periodické povrchové struktury, skenování povrchu, tavený křemen |

## Bibliographic Entry

| | |
|---|---|
| Author: | Ing. Juraj Sládek<br>Czech Technical University in Prague,<br>Faculty of Nuclear Sciences and Physical Engineering,<br>Department of solid state engineering |
| Title of Dissertation: | Modification of bandgap materials by ultra-short laser pulses |
| Degree Programme: | Applications of Natural Sciences |
| Field of Study: | Physical engineering |
| Supervisor: | prof. Ing. Zdeněk Bryknar, CSc.<br>Czech Technical University in Prague,<br>Faculty of Nuclear Sciences and Physical Engineering,<br>Department of solid state engineering |
| Supervisor specialist: | Dr. Yoann Levy<br>Czech academy of sciences, Institute of physics,<br>HiLASE Centre |
| Academic Year: | 2022/2023 |
| Number of Pages: | 130 |
| Keywords: | femtosecond laser, fused silica, laser induced periodic surface structures, silicon, surface scanning |

## Acknowledgments

I would like to express my gratitude to those, who have supported me during my postgraduate studies and who made it possible to write this dissertation. Namely to Prof. N. M. Bulgakova for giving me the opportunity to join her research group at HiLASE, for her continuous support and guidance, and an opportunity to visit world-class foreign research institutes (FTMC, Vilnius; Riken, Tokyo; and The University of Tokyo, Tokyo); to Prof. Z. Bryknar for his support and help; to Dr. I. Mirza for introducing me to the ultra-fast science and experimental support; to Dr. Y. Levy for valuable comments, detailed feedback and positive motivation; to T. J.-Y. Derrien for theoretical support and fruitful discussions; to N. Goodfriend and J. Hrabovský for introduction to AFM microscopy and Raman spectroscopy; and to J. Beránek for introduction to SEM microscopy. Last but not least, I would like to thank my family for their patience and support.

In addition, contributions of my colleagues, whose collaboration on several experiments made it possible to achieve some of the presented results, is acknowledged as follows. Author is denoted as JS. Section 3.1.3: JS – preparation of the initial experiment, A. V. Bulgakov and O. Gatsa – experimental investigation, A. V. Bulgakov and J. Hrabovský – data evaluation; Section 3.1.5: JS – experimental investigation, J. Hrabovský – post-irradiation analysis; Section 3.4.1: JS – experimental investigation, post-irradiation analysis, I. Mirza – experimental investigation, P. Kovaříček – AFM measurement (Fig. 54); Section 4.1: JS and J. Hrabovský – post-irradiation analysis, M. Zukerstein – experimental investigation; Section 4.2: JS – experimental investigation, post-irradiation analysis, data processing, Y. Levy – post-irradiation analysis, DLOA processing; Section 5: JS – experimental investigation, data acquisition and processing, Y. Levy, I. Mirza, J. Beránek, C. Liberatore, W. Marine and A. V. Bulgakov – experimental investigation.

This work was supported by the European Regional Development Fund and the state budget of the Czech Republic (project BIATRI: CZ.02.1.01/0.0/0.0/15 003/0000445). Partial support from the Grant Agency of the Czech Technical University in Prague (No. SGS 22/182/OHK4/3T/14) and the European Structural and Investment Funds and the state budget of the Czech Republic (CZ.02.1.01/0.0/0.0/16 019/0000778) are also acknowledged.

I thank also Dr. J. Bonse and Doc. J. Martan for agreeing to be the opponents and for their time reviewing the manuscript. This version of the dissertation includes several formal corrections of the text, figures and two added citation, that are based on their throughout reviews.

## Abstrakt

Tato práce popisuje experimentální výzkum povrchových modifikací materiálů se zakázaným pásem vyvolaných infračervenými ultra-krátkými laserovými pulzy, a převážně vytvářením pravidelných laserem-indukovaných periodických povrchových struktur (LIPSS). Zatímco vytváření struktur LIPSS bylo demonstrováno na široké škále materiálů, vytváření vysoce pravidelných LIPSS na polovodičích, a převážně dielektrikách, zůstává výzvou. Tato výzva je zde řešena pomocí laserového skenování povrchů křemíku a taveného křemene. Systematickým vyhledáváním v parametrickém prostoru podmínek zpracování byli nalezeny oblasti pro oba materiály, kde je možné tyto pravidelné struktury vytvořit. Kromě prostorově Gaussovských pulzů, pulzy s konstantní intenzitou a pulzy fokusované cylindrickou čočkou, které vedly ke vzniku struktur se dvourozměrnou periodicitou, byly taktéž zkoumány. Bylo zjištěno, že precizní kontrola parametrů zpracování a jejich stabilita jsou klíčové pro úspěšné vytvoření LIPSS. Proto jsou také diskutovány některé jevy způsobující změny prahu poškození materiálů. Tyto zahrnují inkubační efekt, orientaci krystalu křemíku vůči polarizaci, ozařování dvou-barevnými pulzy, přítomnost oxidové vrstvy na křemíku a ablační efekty na polymerech. Navíc je prezentován specifický proces formace LIPSS v pravidelných sloupcích na křemíku a LIPSS na taveném křemeni s proměnnou orientací. Metodika laserového ozařování a také způsoby vyhodnocení jsou detailně popsány.

---

## Abstract

This work presents experimental investigations on surface modification of bandgap materials induced by infrared ultra-short laser pulses, and predominantly on fabrication of regular laser-induced periodic surface structures (LIPSS). While generation of the LIPSS has already been demonstrated on a broad range of materials, generation of highly regular structures on semiconductors, and dielectrics in particular, is still a challenging task. This challenge is addressed here for silicon and fused silica by surface laser scanning. Systematic search in the parametric space of the processing conditions reveals regions where regular structures on both materials are produced. Besides the spatially Gaussian pulses, flat-top and pulses focused by a cylindrical lens, resulting in structures with two-dimensional periodicity, were also investigated. It is found that perfect control of the processing parameters and their stability is critical for successful LIPSS fabrication. Therefore, several effects causing variation of the material damage threshold are discussed. These include incubation effect, orientation of the silicon crystal with respect to the polarization, double-pulse bi-color irradiation, presence of oxide layer on silicon and ablation effects on polymers. In addition, specific processes leading to formation of LIPSS in regular stripes on silicon and LIPSS with variable orientation on fused silica are presented. Methodology of the laser processing as well as evaluation methods are described in detail.

# Table of contents

# Introduction

Laser material processing is a well established technology for achieving controlled cutting, drilling and surface modifications of high quality. The field of laser applications is steadily extending, partially due to an increase in commercial availability of ultrashort pulsed laser sources in the past two decades. The advantage of the ultrashort laser pulses lies in the rapid energy delivery to the material which reduces the heat-affected zone and minimizes interaction with ablation products. The resulting controlled and localized energy deposition enables high precision surface and volumetric processing.

The surface processing (patterning) is possible not only by directly written structures, but also by fabrication of laser-induced periodic structures (LIPSS). These are spontaneously formed (pseudo-) periodic surface modulations, often topographically pronounced, usually with spatial periods in the order of the irradiation wavelength. The presence of such micro/nano-scale structures significantly modifies optical and mechanical surface properties, which can be engineered for specific applications.

Indeed, the possibility to generate nanostructures relatively easily on large areas have found applications where LIPSS are used to alter surface hydrophobicity for self-cleaning surfaces, reflectivity for material coloration and enhanced light absorption, biocompatibility for cell growth or antibacterial surfaces, tribology and more. Generating LIPSS is a straight forward process, however, generation of highly regular structures, which would be beneficial for controlled and deterministic modulation of the surface properties, is more complex. Achieving high LIPSS regularity, which is in particular challenging for semiconductors and dielectrics, remains one of the open questions [1] in the field of LIPSS even after six decades since their discovery.

In this work, surface modifications of silicon and fused silica, materials important for many opto-electronics components, are studied experimentally. This includes LIPSS formation, with a special focus on the parameters affecting their regularity.

The presented work starts with an overview of ultra-fast laser-matter interaction theoretical background and discusses the state of the art of the LIPSS. The Section 2 then gives an overview of laser surface processing as well as post-irradiation characterization techniques used in the experimental parts. Methods for evaluation of the laser-induced damage, beam shaping, laser scanning and synchronization with a laser are presented.

The following Section 3 starts by reporting results on several effects affecting the damage threshold and an efficiency of surface modification, which are important for understanding of fine parameter tuning necessary for regular LIPSS fabrication presented later in the Section. Here, LIPSS are produced on silicon and fused silica by scanning with a spatially Gaussian beam. The investigation of surface patterning continues in the Section 4, where additional beam shaping is employed. This includes doughnut shaped, variable size Gaussian, flat-top and cylindrical lens focused beams. In both sections regular structuring by LIPSS is achieved. In the end, Section 5 summarizes attempts on silicon modification and non-linear effects in the mid-IR spectral range.

## Aims of the dissertation

The main goals set in this dissertation can be summarized as follows:

- Fabricate regular laser-induced periodic surface structures on silicon and fused silica by irradiation with ultra-short laser pulses in the VIS-IR spectral range. Design and build an experimental setup. Find and optimize the key parameters of the structuring process for controlled generation of regular structures on large-area surface under surface scanning conditions.
- Apply spatial and temporal pulse shaping in order to study a possibility of increased control over the surface structuring and improved properties of the realized nanostructures.
- Attempt volumetric modification of semiconductors in the mid-IR spectral range with the Perla-C laser available in HiLASE Centre.
- Describe the methodology used to achieve the presented results. Get expertise in ultra-fast laser ablation process; in-situ imaging; ex-situ characterization methods including optical, confocal, atomic force and scanning electron microscopy; and chemical composition analysis of materials via energy dispersive x-ray spectroscopy and $\mu$-Raman spectroscopy.

# 1 State of the art

When the laser light comes into contact with condensed matter, it initially interacts with the electronic subsystem. Depending on laser intensity, such interaction may lead to different kinds of physical mechanisms, including melting, ablation, temporal and permanent change of optical, mechanical and chemical properties of the irradiated material. With a proper choice of irradiation conditions (wavelength, pulse duration, laser energy fluence, laser field polarization, etc.), laser action allows wide range of material modification possibilities ranging from highly localized gentle changes to strongly damaged material sites. This work contains mainly experimental investigation of the ultra-short pulsed laser-material processing. However, this section will try to provide a theoretical background and insight into the topic of ultrashort-pulse laser-matter interaction phenomena which is experimentally presented in later sections.

## 1.1 Ultra-short pulsed laser-matter interaction

Uniqueness of the ultra-short pulsed laser material processing is based on two aspects. First, during laser energy coupling, heat transfer away from the energy deposition zone is reduced compared to the case of several ps and longer pulses. This significantly increases localization of the deposited energy and lowers modification threshold of materials. Secondly, energy deposition terminates before the onset of shielding effects from laser-induced plasma and ablation products. Consequently, such a fast and highly concentrated energy deposition into the material is dissipated in a cascade of processes which are illustrated in Fig. 1.

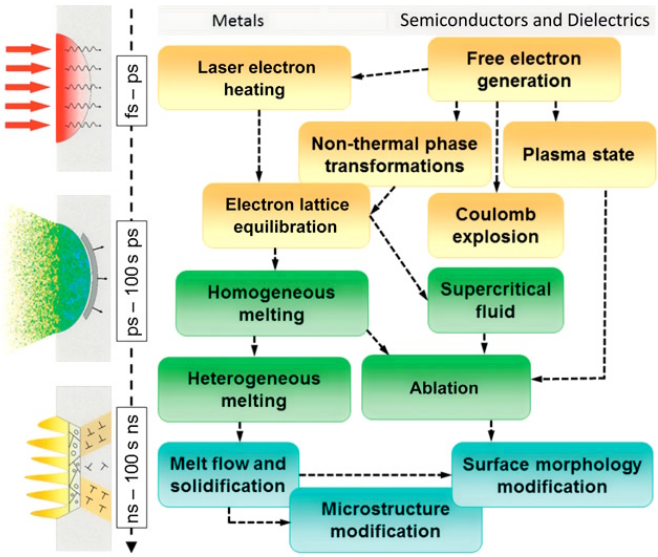


Figure 1: Typical pathways of energy dissipation and phase transformations following the excitation of material by an ultra-short laser pulse. Reproduced from [2].

In the following text, a basic theoretical model of the laser-material interaction is described. Some of the processes will be referenced in the manuscript later. The theoretical description of laser-matter interaction usually starts from laser-metal interaction. Later

on, by defining additional properties of the laser light interaction with semiconductors and dielectrics (which may be turned into a metal-like state by nonlinearly generated free electron plasma) further calculations are performed. The theoretical description presented in this chapter will follow a similar sequence.

### 1.1.1 Metals

Ultrafast laser energy deposition to metals is mediated by free electrons. Interaction of the free electrons with an incoming electromagnetic wave through inverse Bremsstrahlung results in rapid increase of their temperature, while the lattice ions remain relatively cold. Such a strongly non-equilibrium material state of hot electron gas and cold lattice thermalizes by electron-electron and electron-lattice collisions to achieve a final common temperature. The idea of two subsystems with different temperatures was a basis for development of the relatively simple, yet predictive Two Temperature Model (TTM) [3].

The TTM belongs to continuum type models with applications in regimes below material disintegration. Simulations for the high fluence conditions, where vapor phase or fractures may form, are mostly based on hydrodynamics and molecular dynamic models.

The TTM is expressed in the form of the heat flow equations for electrons absorbing laser radiation and lattice heated due to heat exchange with the electrons [3]:

$$C_e(T_e)\frac{\partial T_e}{\partial t} = \frac{\partial}{\partial z}\left(k_e(T_e)\frac{\partial T_e}{\partial z}\right) - G(T_e)(T_e - T_l) + S(z,t)\,, \tag{1}$$

$$C_l(T_l)\frac{\partial T_l}{\partial t} = \frac{\partial}{\partial z}\left(k_l(T_l)\frac{\partial T_l}{\partial z}\right) + G(T_e)(T_e - T_l)\,, \tag{2}$$

where $C_e$, $C_l$, $k_e$ and $k_l$ are the volumetric heat capacity and thermal conductivity for electrons ($e$) and lattice ($l$) respectively. $T_e$ and $T_l$ are the electron and lattice temperatures, $G$ is the electron-phonon coupling factor and $S(z,t)$ is the laser source term, which defines the local laser energy transfer by the laser pulse.

TTM equations are usually written in one dimensional form with the coordinate $z$ perpendicular to surface, which is justified by the fact that in highly absorbing solids effective absorption depth is much smaller than typical irradiation spot size.

The lattice conduction term in Eq. 2 is usually omitted, as the lattice conductivity is negligible on the timescale when the thermal equilibrium between electrons and lattice is establishing after ultra-fast laser excitation (typically several to tens of ps) [4]. To find the temporal variation of $T_e$ and $T_l$, the above coupled differential equations are solved numerically, but under certain approximations, an analytical solution can be derived as well.

In metals, laser energy is absorbed only by a fraction of the free electrons what leads to pronounced deviation of the electron energy distribution from a Fermi–Dirac distribution [4]. Two populations of electrons result in this way: ballistic and thermal. The non-thermalized ballistic electrons efficiently transfer energy to deeper layers while exchanging energy with non-excited electrons and partially with lattice and thermal electrons. The thermal electrons transfer energy gained from the non-thermalized electrons to the lattice and deeper into the bulk. Therefore, a third coupled equation may be added to the TTM to account for the two electron subsystems [5].

Material parameters found in the TTM equations are strongly temperature dependent and therefore exhibit significant variations during and after the interaction with the laser pulse. In metals, transient change of the optical response is usually reasonably described by the Drude model through complex dielectric function [6]. However, several fitting parameters that vary upon excitation are included in the calculations. Hence, application of this model provides good understanding of the main trends of the optical response, but quantitative analysis may be problematic.

### 1.1.2 Semiconductors

Free electrons are already present in metals, while in wide bandgap materials, these must be first generated. In this case, evolution of the free electron density $n_e(t)$ can be described by the following simplified rate equation [7]:

$$\frac{\partial n_e(t)}{\partial t} = \sigma_k I^k(t) + \delta I(t)\, n_e(t)\,, \tag{3}$$

where $\sigma_k$, $\delta$ and $k$ are the multiphoton ionization cross section, the avalanche coefficient and a number of photons required for photo-ionization respectively. Similar rate equation applies also to the free carrier dynamics in semiconductors.

In semiconductors, generation of free electrons usually starts by one- or two-photon absorption, in the wavelength range around visible spectral region. After certain electron density is reached, this mechanism is superseded by collisional ionization. Excitation is followed by electron recombination, which in semiconductors is preferably by Auger recombination [8]. Therefore, carrier density evolution can be expressed as follows [4]:

$$\frac{\partial n_e}{\partial t} = \left[\left(\sigma_1 + \frac{1}{2}\sigma_2 I\right)\frac{I}{\hbar\omega} + \delta n_e\right]\frac{n_0 - n_i}{n_0} - R_e\,, \tag{4}$$

where $n_e$, $n_i$ and $n_0$ denotes densities of electrons, ions and undisturbed lattice respectively. $I$ is the laser intensity, $\sigma_1$ and $\sigma_2$ are the one- and two-photon ionization coefficients, $\delta$ is a temperature dependent collisional multiplication coefficient and $R_e$ is the loss term determined by the Auger recombination [8]. Electron and ion densities are assumed equal, even though in a surface layer where effective photoemission occurs this can be violated and may result in a Coulomb explosion.

This equation also implies the generation of an inhomogeneous free electron density profile decreasing toward the bulk depth, due to attenuation of the beam propagating through absorbing medium [9]. Moreover, because of a dynamic behavior of free electron density governed by a highly nonlinear avalanche process, optical response of laser-excited semiconductors is strongly varying already during the laser pulse [4].

The problems known from laser-excited metals as incomplete thermalization within the electronic subsystem, superheating of the solid phase and insufficient knowledge about behavior of several physical properties stay valid also for semiconductors.

### 1.1.3 Dielectrics

In dielectrics, ultra-short pulsed laser irradiation can start a variety of mechanical and chemical modifications such as change of density and refractive index [10], formation

of voids [11], periodic surface and volume structures [12, 13], phase transformation or amorphization [14].

The modification process in wide bandgap dielectrics is usually initiated by multiphoton ionization [15], order of which is determined by the ratio between the bandgap width $E_g$ and photon energy $\hbar\omega$. However, at high laser intensities, the tunneling ionization may dominate over multiphoton ionization. This applies especially to wavelengths toward the mid-IR range. Which type of ionization is dominant can be estimated by the *Keldysh* parameter $\gamma = \omega\sqrt{2m_{\text{eff}}E_g/(eE_L)}$, where $\omega$, $E_L$, $m_{\text{eff}}$, $E_g$ and $e$ are the frequency and electric field of the laser wave, the electron effective mass, band gap energy and the unit charge respectively. Multiphoton ionization dominates the excitation process ($\gamma \gg 1$) in most cases of laser-material interactions with dielectrics in the regime of laser processing [16].

After a certain free electron density is reached, free electrons start to absorb laser radiation by themselves and avalanche electron ionization may develop. Similarly as in semiconductors, this results in a considerable alteration of the optical response of the irradiated region toward metallization. The following electron recombination may result in trapping them in localized states with a characteristic recombination time $\tau_{\text{tr}}$, accompanied by creation of color centers, excitons and other defects [16, 17]. Defect generation further leads to incubation effects observed as decrease of the damage threshold in multipulse irradiation regimes [18].

The rate equation in dielectrics should contain multiphoton and avalanche ionization terms. For materials with short recombination times, also a recombination term must be included due to possibility of re-excitation. This results in an equation in the following form:

$$\frac{\partial n_{\text{e}}(z,t)}{\partial t} = \left[\sigma_{\text{k}} I^{\text{k}}(t) + \delta I(t)\, n_{\text{e}}\right] \frac{n_0 - n_{\text{i}}}{n_0} - \frac{n_{\text{e}}}{\tau_{\text{tr}}}\,, \tag{5}$$

where notation corresponds to the Eq. 4.

After the electronic excitation, a swift recombination follows, heating the material and triggering a series of effects over a broad time scale. These are summarized in Fig. 2.

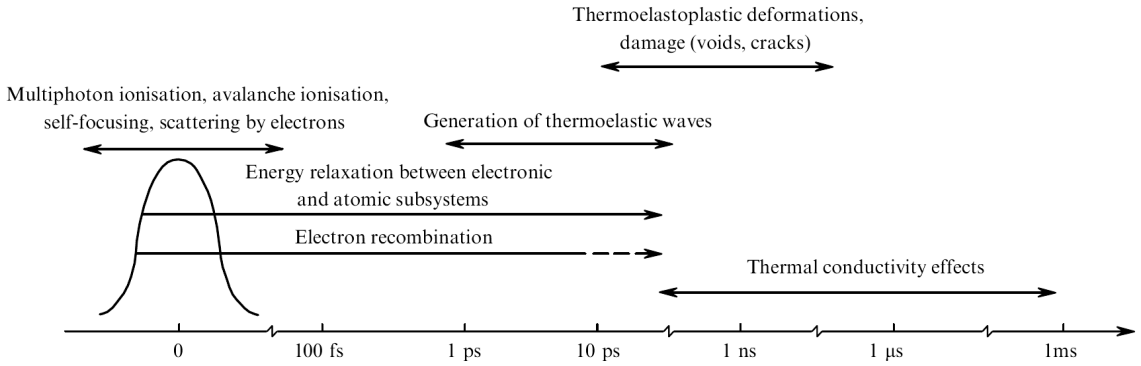


Figure 2: Characteristic time scales of various processes caused by irradiation of a transparent dielectric by a femtosecond laser pulse. Reproduced from [19].

### 1.1.4 Melting and ablation

Deposition of laser energy into material results in its heating, which may lead to melting, vaporization or generation of plasma. When melting conditions are reached, depending on energy deposition rate, normal heterogeneous or homogeneous melting takes place. Material melting results in changes of optical properties, redistribution of material or emission of pressure waves. Afterwards during resolidification, initially crystalline materials can recrystalize, or can turn amorphous, if the cooling rate is higher than the kinetically limited phase transformation [20]. In laser microprocessing, (partial) material melting in the vicinity of the irradiation spot is one of the main reasons for the heat affected zone.

Rapid energy delivery into the material by ultra-short laser pulse causes not only material modification, but is often connected with ejection of particles and clusters from the surface, i.e. laser ablation. It consists of several mechanisms, such as Coulomb explosion, phase explosion, spallation or fragmentation, taking place at different timescales [19, 21–23].

In the case when material excitation occurs via multiphoton absorption, it is likely that the energy of $N$ photons absorbed by an electron is slightly higher than necessary to overcome the bandgap. This excessive energy will be added to the electron kinetic energy. As a lower edge of the conduction band is close to the vacuum level, the electrons located near the laser target surface, at a depth less than their mean free path, can leave the surface.

Emitted electrons leave positive holes in the irradiated region near the surface. In dielectrics, and even in semiconductors [24], it takes about a picosecond or longer for bulk electrons to fill these holes. During this time the positively charged surface may become electrostatically unstable and, at a sufficiently high hole density, breaks apart by emitting positive particles which are accelerated by the residual field. This effect, which takes place during the first hundreds of fs [25], is known as a Coulomb explosion. Effect of Coulomb explosion depends inversely on free electron mobility. Therefore, it can be observed in dielectrics even when other ablation mechanisms are not yet present [26].

In semiconductors, an effect of ultra-fast (nonthermal) melting, or order-disorder transition is observed. When a significant portion ($\sim$10 %) of the valance electrons is excited to the conduction band, the lattice loses crystalline order, even though being at a temperature well below the melting point [27, 28]. In silicon, this transition is observed in a few hundreds of fs after excitation [28] at a fluence three times higher than necessary for normal melting [27]. However, melting depth of 20–40 nm [28] is an order of magnitude smaller than for normal melting after electron-lattice thermalization [4].

Consequently, a layer beneath the region disintegrated by the Coulomb explosion, as well as in the case of directly irradiated top surface layer in metals and semiconductors, will be heated up to extremely high temperatures. This induces layer fragmentation into an atomic phase that will expand away from the surface. The fragmentation process depends on the electron–phonon coupling time, and therefore on the material, but can occur already in first dozens of ps [4].

The underlying layer, heated by the hot electrons, is unable to boil, because the timescale does not permit the necessary heterogeneous nuclei to form. Instead, bulk superheating will occur. This layer may approach the thermodynamic critical temperature at

which homogeneous nucleation develops at a very high rate. The material of now surface region explosively decomposes into a mixture of vapor and equilibrium liquid droplets. Such explosive decomposition (phase explosion) is delayed with respect to the atomic phase ejection and can take from tens to hundreds of ps [22].

Finally, after a few ps, a sharp increase in the lattice temperature in a confined surface region results in formation of thermoelastic waves that can cause material spallation as a final step of the ablation process [23].

## 1.2 Surface modification induced by ultra-short pulsed lasers

Prior to going into detailed discussion of laser based surface modification and nano/micro structuring of solids, it is useful to elaborate the following important effects:

- Accumulation effects - in multi laser shot and high repetition rate processing;
- Environmental effects - induced during processing of materials in air at atmospheric condition.

### 1.2.1 Effects in energy deposition

***Incubation effect***

Laser processing of each material can be characterized by a threshold fluence, at which a single-shot ablation occurs. However, when irradiated by multiple high power laser pulses with single pulse fluence well below the materials ablation threshold, material surface can become modified anyway. This is an important aspect to be considered for all high power laser components and material processing under overlap of successive laser pulses.

Decrease of the material damage threshold as a function of number of applied laser pulses (see Section 3.1.1) is a well-known behavior called incubation (or accumulation) effect. The decrease in ablation threshold with increasing number of applied laser shots follows approximately a power law equation [29]

$$F_N = F_1 N^{s-1} \,. \tag{6}$$

where $F_N$ is the damage threshold fluence of $N$-pulses, $F_1$ is the single pulse damage threshold fluence, $N$ is the number of applied laser pulses and $s$ is called an incubation factor. The $s$ factor, which can be obtained experimentally for every material, describes the importance of the incubation effect. The physical reason of this material behavior was proposed to be an accumulation of plastic deformations in metals and laser-induced defects, such as color centers, in semiconductors and dielectrics [30].

***Two ablation regimes vs damage thresholds***

Ablation threshold can be determined by one of the laser-ablation crater properties. Usually, the crater diameter is a parameter of a choice because of the ease of its measurement. In some cases, particularly when ablation efficiency is studied, volume of the ablation crater or depth is investigated instead. For metals it was shown [30, 31] that the ablation depth is linearly proportional to a logarithm of the pulse fluence (i.e. energy per

area [J/cm$^2$]). It was also shown that two regimes with two threshold fluences could be observed for laser pulses shorter than ∼1 ps, as it is demonstrated in Fig. 3. The first regime of the "weak" ablation correlates well with an optical penetration depth, defined as an inverse of light absorption coefficient at irradiation wavelength. The other regime of "strong" ablation is characterized by the electron heat diffusion length, defined as a distance through which the heat energy is transported by the hot electrons in the material. This signifies the necessity of a careful choice of the pulse energy range for the damage threshold estimation.

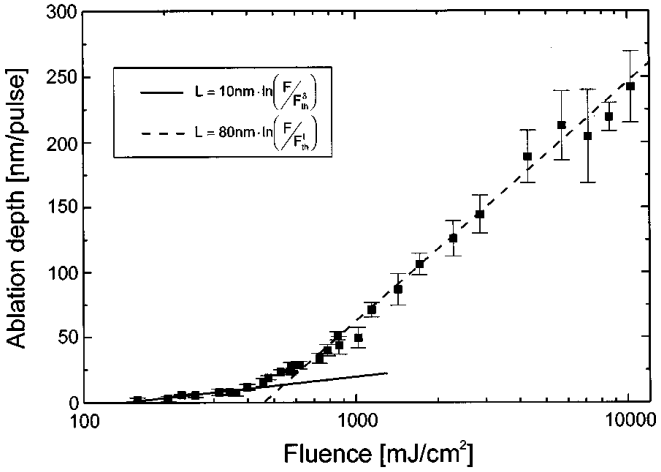


Figure 3: Dependence of the ablation depth per pulse of copper on laser pulse fluence. The solid and the dashed lines represent fits for weak and strong ablation regimes. Reproduced from [31].

***Pulse bursts***

The full potential of precise material ablation by ultra-short laser pulses with negligible thermal damage is limited by the material removal speed. Figure 3 hints, an increase of the laser power to be a direct way of enhancing ablation efficiency. However, larger pulse energy amplifies also unwanted effects, such as plasma shielding or collateral damage.

One of the proposed solutions is the so called laser ablation cooling technique [32], which is based on an idea of ablating the heated material before the residual heat from previous pulse diffuses away from the processed region. Because the ablated material is physically carried away, the thermal energy contained within the ablated mass is also removed, thus reducing the average temperature of the remaining material.

Considering the speed at which the diffusion occurs, this regime requires extremely high laser repetition rate. Typically, several hundreds of MHz is sufficient, but metals with high thermal conductivity may require even higher rates [33]. Lasers themselves are not continuously operating at such intra-burst repetition rates, but, instead trains of pulses (bursts, Fig. 4) can be produced at lower repetition rates. In addition, other options for burst generation exist, such as splitting a single pulse by birefringent crystals, using interferometers or cascaded beam dividers.

As a consequence of ablation cooling, not only heat affected zone and collateral damage is reduced, but apparently also necessary pulse energy (required for ablation) decreases and ablation rate is enhanced [32]. Burst mode ablation promises advantages as compared

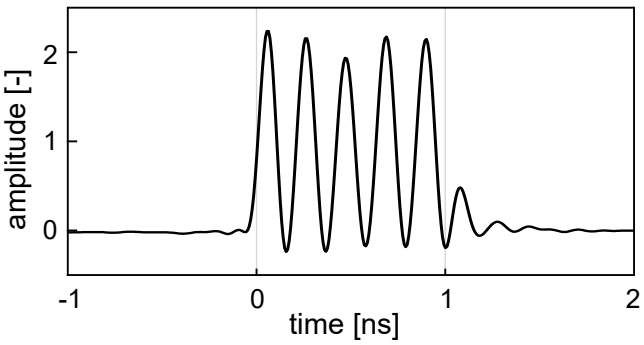


Figure 4: A fast photodiode signal of a 5-pulse burst at an intraburst frequency of 5 GHz used during experimental investigation of material ablation efficiency [34, 35].

to lower repetition rate processing. This was already demonstrated for metals and semiconductors in a narrow region of low fluence range [33]. However, at higher fluences, single high-energy pulses with low repetition rates still outperform burst ablation in ablation efficiency, what raises doubts about real applicability of this developing method.

### 1.2.2 The role of ambient gas in material processing

A majority of scientific and application specific laser-material processing is performed in an ambient environment, mainly in air under atmospheric conditions. The role of ambient gases in laser-material processing is usually neglected. It is still insufficiently understood due to the complexity of laser beam propagation in an ionizable media and a variety of involved physical processes [36, 37].

In the past decades, power of the ultrafast laser systems as well as their repetition rates have been continuously increasing and lasers with power above 10 W and repetition rates above tens of MHz are now commercially available. However, such high repetition rates and the typically high intensity employed signifies the problem of laser-air interaction. The study on the role of nitrogen metastable states [37] clearly shows the air breakdown mechanism and accumulation effects are observable at repetition rates as low as 10 Hz.

It is known that the ambient air can have a negative impact on metal microprocessing, compared to the vacuum environment [38]. A slight dependence of the processing environment on glass ablation can also be observed [39]. In a single-pulse regime, a lower fluence was required to initiate material ablation in air as compared to the high vacuum conditions. On the other hand, there is no significant dependence in a multi-pulse regime. The lower single-pulse ablation threshold in air may be attributed to a modified absorption process. First, the reactive environment (e.g. air) could accelerate the ablation chemistry. Second, the hot material plasma expands at a slower speed in air than in vacuum. Slower expansion provides a longer time for the energy to couple from plasma radiation back into the target.

## 1.3 Laser–induced periodic surface structures

LIPSS are (quasi-) periodic micro- to nano-scale structures that are spontaneously formed after irradiation of solids with polarized laser pulses. Fabrication of LIPSS is a technologi-

cally simple, single-step process, which can be conducted under ambient conditions and on almost any material, including metals [40], semiconductors [41–44] and dielectrics [45–48]. LIPSS were also observed in a broad range of pulse duration ranging from continuous beam [49] to a few fs pulses [50].

Features of the LIPSS depend on laser parameters, such as laser fluence, pulse duration, polarization orientation, number of pulses, angle of incidence and on type of surface material. LIPSS period $\Lambda$, the main property, is linearly dependent on the laser wavelength $\lambda$. It is also known that for typically used processing conditions on metals and semiconductors, the period tends to decrease with increasing number of pulses [51]. This effect is attributed to variation in grating-assisted plasmon coupling on LIPSS on their increasing depth. However, on semiconductors this trend can be opposite for high fluences [52, 53]. Similarly, the opposite trend is usually observed on dielectrics [45, 47]. High number of applied pulses ($\geq$1000) can also change the groove/ripple structures into columnar microstructures and spikes.

LIPSS spatial period is typically close to or slightly shorter than the laser wavelength at normal laser incidence. The period can be additionally manipulated by changing the incidence angle $\theta$. On strongly absorbing materials an angular dependency $\Lambda_\mathrm{p} \sim \lambda/(1 \pm \sin\theta)$ and $\Lambda_\mathrm{s} \sim \lambda/(\cos\theta)$, depending on the polarization (s, p), was predicted [54, 55]. Normal laser incidence is assumed in the rest of this work.

Two major types of LIPSS can be distinguished: low spatial frequency LIPSS (LSFL) with periods $\lambda/2 \leq \Lambda_\mathrm{LSFL} \leq \lambda$ (Fig. 5a,c) and high spatial frequency LIPSS (HSFL) with periods that are a fraction of the irradiation wavelength ($< \lambda/2$, Fig. 5b,c). Based on Bonse *et.al.* [56], further subdivision of both types is proposed, but we will focus on the LSFL (Fig. 6). Reviews on LIPSS types [57], or period and orientation for various materials [58] provide additional detailed information.

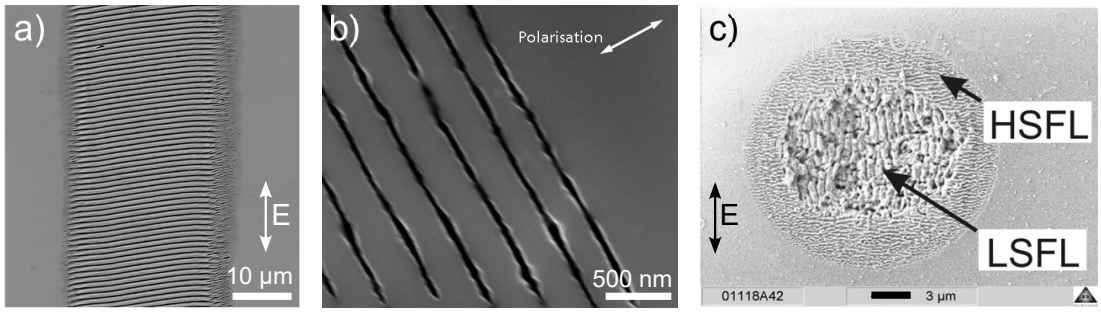


Figure 5: LIPSS on dielectrics: a) LSFL (sapphire), b) deep HSFL grooves (fused silica) and c) coexistence of HSFL and LSFL (c-$SiO_2$). Adapted from a) [47], b) [59] and c) [45].

LSFL on strongly absorbing materials (metals, semiconductors) are typically oriented perpendicular to the linear polarization with a period close to the irradiation wavelength (Fig. 5a). This LSFL-I type of structures are understood to be created by interaction of direct laser beam with a scattered electromagnetic surface waves which may include surface plasmon polaritons (SPP) [53, 55]. It should be noted that with ultra-short laser pulses, photogenerated free electrons can reach a density when initially plasmonically non-active materials can be transiently turned into a metallic state supporting direct excitation of SPP [52, 53, 60]. On materials where single photon energy is lower than its band gap,

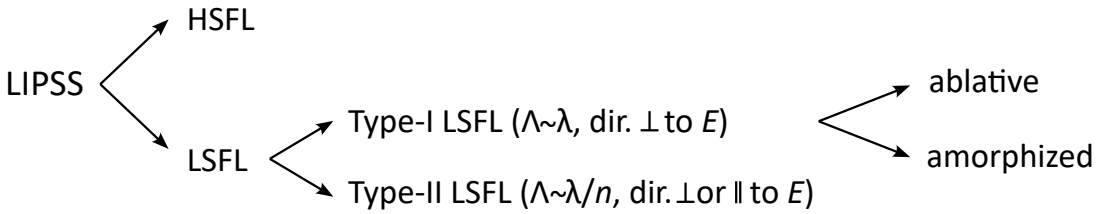


Figure 6: LIPSS classification diagram: laser wavelength $\lambda$, LIPSS period $\Lambda$ and light polarization $E$. Based on [56].

LSFL-II type of structures, oriented parallel to the polarization and with a spatial period $\Lambda_{\mathrm{LSFL-II}} \sim \lambda/n$ where $n$ is a real part of the material refractive index [45,55], are observed. In this case, the interaction occurs between incident laser beam and so-called *radiation remnants* [61], representing non-propagating surface electromagnetic mode. In addition, LSFL-I may appear in two regimes. The LSFL are fabricated mainly in an ablative regime, when the incident pulse energy is above the material ablation threshold, resulting in topographically pronounced structures. However, for lower pulse energies, local (partial) melting of the surface followed by rapid resolidification occurs, leaving only a thin surface layer altered. On monocrystalline silicon, for example, amorphous regions created by such process can organize into periodic amorphous-crystalline LIPSS [44, 62–65].

HSFL structures, that renewed interest in the LIPSS topic three decades after the discovery of the LSFL, occur close to material damage threshold and are predominantly observed for the ultra-short laser pulses. Depending on the material, orientations parallel or perpendicular to the polarization exist. So far, several theories describing HSFL exist, but there is no general agreement on their origin.

LIPSS were first described by Birnbaum in 1965 [66] while investigating damage of semiconductors, in particular monocrystalline germanium, by a ruby laser. Their formation was attributed to diffraction effects on the lens aperture.

This explanation was corrected in 1973 by Emmony *et al.* [54] who had studied laser damage of Ge mirrors on a $CO_2$ laser. They elaborated an interference model assuming an interference of the direct beam with surface-scattered waves and predicted a dependency of the LIPSS period on an angle of incidence. However, the assumed scattering on surface centers would lead to a circular interference pattern instead of periodic lines. Therefore, creation of the initial interference fringes based on geometrical layout of the laser were considered. These would then diffract light along the surface, causing a positive feedback for the anisotropic surface damage.

Further major step in the theoretical development came from Sipe and coworkers in 1983. Their generalized model, nowadays often referred to as the *Sipe theory*, predicts the possible inhomogeneous energy absorption induced by surface roughness [55]. The absorption depends on an *efficacy factor* $\eta(k)$, which describes an efficacy of energy absorption by the surface roughness at a given wave vector $k$, and a factor $b(k)$, describing initial surface roughness. LIPSS are predicted to form at spatial frequencies, with the highest absorbed energy, i.e. where the $\eta$ experiences sharp peaks. While the initial theory was later reformulated by Bonse and coworkers in 2005 [42] to ease calculation of the efficacy factor, the drawbacks, such as omitting feedback from forming LIPSS or

neglecting transient changes of the material dielectric function $\eta$, remained.

The latter problem was addressed by Bonse *et. al* a few years later [53,67]. Irradiation of material, in particular semiconductors and dielectrics, by ultra-short pulses, can lead to significant changes of the conduction band occupancy, eventually turning the material transiently into metallic state. To account for this, the Sipe theory was combined with a Drude model, predicting variations of $\eta$ based on the excited electron density, resulting in a so called *Sipe-Drude model*. Metalization and possibility of surface plasmon generation helped to explain several features in LIPSS formation on semiconductors such as their orientation, periodicity or narrow window of the fluence range [52].

The Sipe theory was proven to be correct experimentally [68] and an agreement was found also with a numerical FDTD approach [69, 70]. The FDTD additionally allowed to introduce inter-pulse feedback by material ablation and, unlike the Sipe theory, is able to predict formation of the HSFL.

Currently, there are several electromagnetic models describing the occurrence of the LIPSS as a result of interference between laser and surface electromagnetic waves. These models assume the LIPSS signature is seeded already during the laser irradiation. In addition, other types of models were developed, which are based on material redistribution, which progresses after the action of the laser pulse. These include hydrodynamic instabilities [71], self-organization [72] and other. It was, and partially still is, controversial, which description approach is correct. Fortunately, with availability of ultra-short lasers it is possible to distinguish these approaches, based on their timescales. Indeed, this controversy of LIPSS origin was addressed in experiments with double-pulse irradiation [73] and fs time-resolved pump-probe experiments [64,74], which both prove that the ultrafast excitation stage of the electromagnetic models is essential for the LIPSS formation. However, recent improvements in the theoretical modeling by electromagnetic FDTD [69,75], hydrodynamics [71] and molecular dynamics [76], which involve material reorganization, show that both approaches can contribute to the final structure. An extended review on the models of LIPSS can be found in Bonse and Gräf [57]. Due to a variety of involved mechanisms and several unsolved questions on the LIPSS formation, a comprehensive theory of LIPSS is not yet available.

Even though imprinting of periodic features on rough surface can be observed after a single laser pulse (Fig. 7a,b), formation of pronounced and regular LIPSS typically requires a multi-pulse action. This is due to a positive feedback of the successive pulses, which includes intra-pulse (transient change of optical properties, creation of defect states, ... ) and inter-pulse (topographical changes at specific frequencies, roughness generation, defect incubation, ... ) effects. As a result, surface nanostructuring by LIPSS typically shows a build-up phase with increasingly pronounced structures.

Importantly, by a structural feedback from already existing LIPSS, the LIPSS can coherently extent to adjacent partially overlapping irradiation spots [41]. By this way, upon laser scanning of the surface, LIPSS can be continuously extended along the scanning line (Fig. 5a). Subsequent overlapping of individual scanning lines eventually results in a large surface covered with homogeneous LIPSS [77, 78].

The mentioned single-pulse formation of periodic structures is possible in particular when scattering on a preexisting surface features (particles, scratches, ablation crater edges) occurs [53, 59, 79]. These have a tendency to be an origin of the local periodic

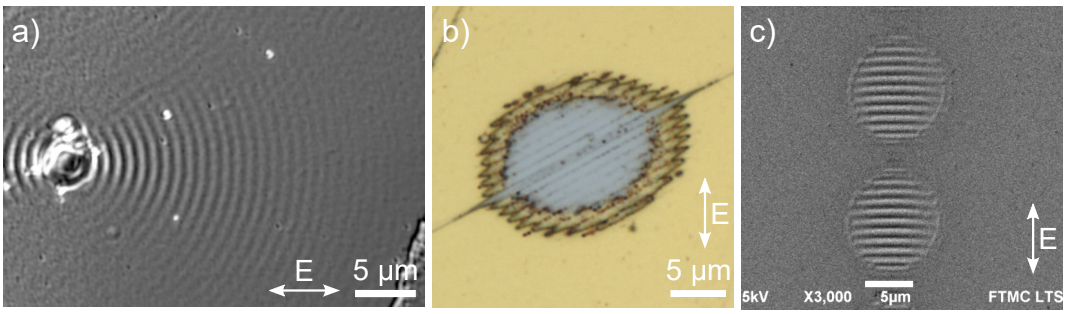


Figure 7: Single-pulse inscription of interference waves from scattering on defects: a) a microparticle, b) a surface scratch and c) LIPSS coupling between adjacent pulse positions with a pristine separating area (two times overscan).

structures, as demonstrated in Fig. 7a-b. If several such defects are acting in parallel in a single area, the resulting pattern will be a superimposition of all scattered waves. Periodic structures from scattered waves show a clear tendency to follow a boundary of the particular defect which is especially visible on a line defect. This behavior can be actually used to generate artificial seeds for predefined periodic structures [80]. All of these localized periodic structures can be coherently extended by the beam scanning what can disrupt attempts for highly-regular large-area structures. Therefore, using a microscopically clean and smooth surface is a good step towards high structure regularity.

Interestingly, as shown in the Fig. 7c on a twice scanned line of spots on Si, as well as in literature [65], coherent extension of the periodicity is possible even if the periodically modified area is not in a direct contact with the scattering feature.

Presence of nanostructures on the surface of a material will modify its macroscopic optical, mechanical or even chemical properties. The ease of the LIPSS fabrication for engineered surface properties by controlled nanopatterning predicts their use in a variety of applications. These include surface structural colorization [81, 82], wettability control [83,84], control of the cell growth and adhesion [85], biomimetic surfaces [86], friction reduction [87, 88], nanopatterning and periodic chemical functionalization of 2D materials [89, 90] or enhancement of the surface enhanced Raman scattering [91]. For use in applications, it is of interest to predict an area of parameters where the desired type of LIPSS is generated, which often requires an experimental study.

The sub-micrometer feature sizes of the LIPSS may evoke a slow processing throughput. However, recent advances in high-power, high-repetition rate lasers in combination with fast polygon scanners and diffractive optical elements (DOE) show that processing speed up to 0.5 $m^2$/min [43,63,92] for practical applications and relatively large areas are already possible.

However, high processing speed does not necessarily coincide with high structure quality. Therefore, the next logical step is to focus on fabrication of large areas of highly regular LIPSS (HR-LIPSS). Such works on nanostructuring with LIPSS indeed progressed with an additional emphasis on the uniformity [44, 63, 93–96] and the structure regularity [43, 78, 97–99]. The best results seems to be obtained at metallic and semiconductor thin films and/or with a line focus. On the other hand, on dielectrics, where nonlinear absorption is needed, uniform structuring of uncoated material with LIPSS remains

difficult.

Recently, fabrication of LIPSS can be often seen in conjunction with a competing method of direct laser interference patterning (DLIP), which generates similar types of structures. In DLIP, two or more focused beams are interfering and producing a surface pattern by ablation in the interference maxima. Periods are given by an angle of incidence and in general are larger than that of LIPSS. DLIP is also typically limited to ps and longer pulses in order to maintain interference volume. On the other hand, structure depth can be controlled independently of the period.

## 1.4 Volumetric modification of bandgap materials

Practical outcomes of material irradiation by ultra-short laser pulses are not bound only to the material surface. Focusing of the ultra-short pulses inside of transparent materials may lead to controllable volumetric modifications. The main focus is typically to manipulate the refractive index, with an aim to create waveguiding structures [100] or to store data, and fabrication of microfluidic devices [101, 102].

Volumetric material modification is caused by the rearrangement of bonds and displacement of atoms in the target volume. These lead to a change in density, composition and stress accumulation within the interaction volume, all of which are also strongly dependent on accumulation effects.

After the laser beam enters the media, its propagation can be described by nonlinear Schrödinger equation (NLSE), while accounting for effect such as diffraction, optical Kerr effect, plasma defocusing and energy absorption. In case of tight focusing (violation of the slowly varying envelope) a rigorous description by Maxwell equations must be used instead [103].

Figure 8 shows simulation results of deposited energy into fused silica by an ultra-short laser pulse. The four left sequential graphs of the energy absorption (over four successive time domains) demonstrate that highly efficient pulse absorption occurs only for the leading edge of the laser pulse; which is mostly absorbed in front of the geometrical focus due to self-focusing. Generated electron plasma strongly defocuses the remaining parts of the pulse. As a result, these deposit their energy even further before the geometrical focus or behind the focus due to self-focusing after scattering. Characteristic distribution of the deposited energy is than shown in the rightmost graph.

Volumetric writing of phase structures in glass is performed in a gentle manner by using a large number of pulses with low intensity. This leads to a significant accumulation effects where heat accumulation plays a major role [106]. At high repetition rates, heat does not have enough time to diffuse away before arrival of the subsequent pulse and temperature rises. As a result, a region of modification can form around the focusing spot. In this case, two distinct zones can be recognized: the zone of molten material and the zone that has reached the softening temperature [107]. At higher pulse energies, stress waves, cracks and void formation are usually observed. Such regime finds applications typically in the field of direct microfabrication, for example of microfluidic devices.

Another interesting volumetric phenomenon is self-assembled volume nanogratings [13]. These are spontaneously formed periodic layered structures of subwavelength periodicity, which are created in transparent materials, perpendicular to light polarization,

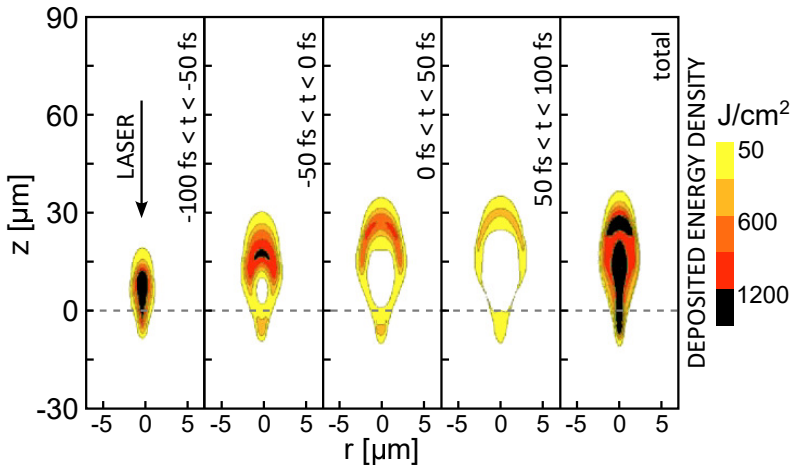


Figure 8: Sequential energy deposition in free carriers in an irradiated a-$SiO_2$ for a laser energy input of 1 $\mu$J and 120 fs duration. The graph on the right, showing total absorbed energy integrated by the end of the laser pulse, is preceded by sequential energy absorption over the four time domains. Modified from [104].

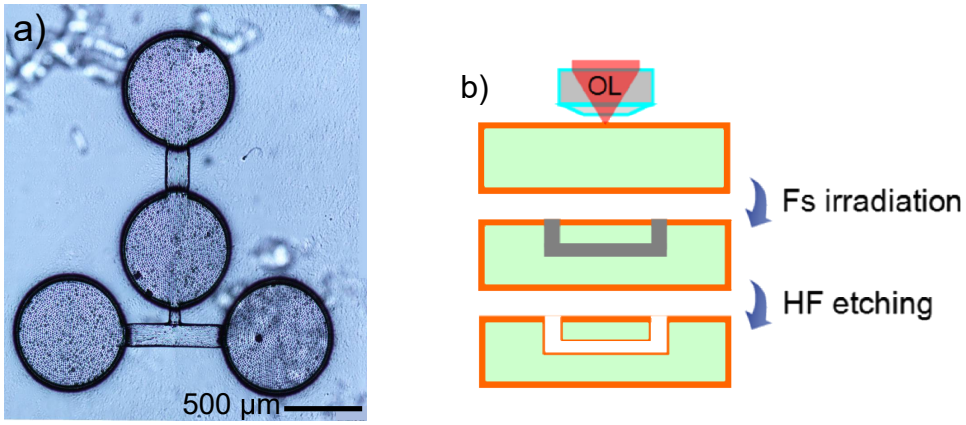


Figure 9: a) A microfluidic device fabricated during an internship (RIKEN, Tokyo, Japan) in photosensitive Foturan® glass. Four round inlets with interconnecting channels of 100 and 200 $\mu$m in diameter are visible. b) Schematic illustration of the fabrication procedure (see text). b) modified from [105].

at irradiation conditions at the onset of thermal material modification. Material birefringence induced by the nanograting can be used to fabricate polarization modifying optical elements [108], or the open voids can serve as microfluidic channels [109].

Further, additional direct and indirect volumetric nanofabrication methods exist. Figure 9a shows an example, a successful attempt to fabricate a microfluidic device in photosensitive glass with four vertical inlets interconnected by horizontal channels 100 and 200 $\mu$m wide. Figure 9b illustrates three main steps to fabricate this type of microdevice. First, the photosensitive glass is irradiated by high intensity laser pulses and is heat treated, what causes the glass to locally crystallize. Crystallization modifies material etching rate. Consequently, the processed area can be etched away chemically in a diluted HF resulting in high aspect ratio, microscopic, smooth structures.

# 2 Experimental methods

To achieve the presented experimental results, a wide range of irradiation and analysis methods was employed. A basic description of these will be the content for the following section. Additional information on the laser hardware and methodology used in ultrashort laser-material processing can be found in our published paper [110]. Furthermore, a detailed description of the hardware built for scanning and one of the data evaluation procedure are given in the Appendices B, D, E, F.

## 2.1 Lasers and surface scanning

### 2.1.1 Lasers used

During the laser-material interaction experiments presented later in this work, several laser systems were used. Table 1 summarizes their parameters. Tunability of the repetition rate is understood here as a possibility to arbitrarily divide the maximum repetition rate of the laser.

The Pharos laser was used for a majority of the experiments. The Astrela laser was used for the polarization damage threshold experiment (Section 3.1.2) and a doughnut beam nanostructuring (Section 4.1). The Perla-B laser was used in the LIPSS scanning experiments on Si (Section 4.4) and on a Mo thin film [111]. The Perla-C laser was used in the mid-IR interaction experiment (Section 5). The DG laser was used for polystyrene ablation (Section 3.1.5). The Pharos (2) laser was used in a burst-mode ablation experiment (Section 1.2.1, [34]).

### 2.1.2 Gaussian beam

Knowledge of the energy distribution inside of the laser beam is a keystone in laser processing of materials. This knowledge, together with clear definition of the beam parameters, are necessary for successful and reproducible application of laser sources. A laser beam with Gaussian spatial intensity distribution is typically used, as it is naturally created as the lowest order transverse mode of a stable laser resonator. It is a convenient spatial distribution, as it is preserved during propagation and focusing, and can be focused to a diffraction-limited spot. Being a fundamental part of the laser physics, detailed derivations of its properties can be found in numerous literature, for example in [112]. In this subsection, only a summary of important characteristics for practical laser-material processing is presented.

Gaussian beams have a transverse profile of the electric field described by a Gaussian function at every position along the propagation, with a parabolic phase profile. For a monochromatic, radially symmetric beam (applying transverse coordinate $r^2 = x^2 + y^2$), propagating in the $z$ direction and with a wavelength $\lambda$, the complex electric field amplitude is

$$E(r,z) = E_0 \frac{\omega_0}{\omega(z)} \exp\left(-\frac{r^2}{\omega^2(z)}\right) \exp\left(i\left[kz + \frac{kr^2}{2R(z)} - \arctan\frac{z}{z_0}\right]\right), \tag{7}$$

| | Pharos (Light Conversion) | Astrela (Coherent) | Perla-B (Hilase) | Perla-C100 (Hilase) | DG (Dausinger +Giesen) | Pharos (2) (Light Conversion) |
|---|---|---|---|---|---|---|
| Wavelength [nm] | 1030 | 800 | 1030 | 1030 | 1030 | 1030 |
| Pulse duration [fs] | 240 - 10 000 | 35 | 1400 | 1000 | 1.4 ns | 220 |
| Repetition rate [kHz] | 200 (tunable) | 1 (tunable) | 1, 10 | 91 (tunable) | 1 | 200 (tunable) |
| Pulse energy [mJ] | 2 | 7 | 1.3, 22 | 1 | 100 | ~2 |
| Maximal power [W] | 6 | 7 | 13, 18 | 80, 100 | 100 | 10 |
| $M^2$ | 1.1 | 1.2 | 1.1 | 1.2 | 1.3 | 1.1 |
| Harmonics | 2H, 3H, 4H | 2H, 3H | 2H | 2H, 3H, 4H, 5H | N/A | N/A |
| OPA [µm] | N/A | ~1.3 - 16 | N/A | ~1.5 - 3.2 | N/A | N/A |
| Intra-burst repetition rate | as repetition rate | | | | | 5 GHz |
| Burst pulse number | adjustable | | | | | 1-25 (adjustable) |

Table 1: Parameters of the laser systems used in the experimental part of this work. Other parameter configurations are possible in particular for the HiLASE beamlines (in gray). Typically, maximal pulse energy and repetition rate can not be achieved at the same time.

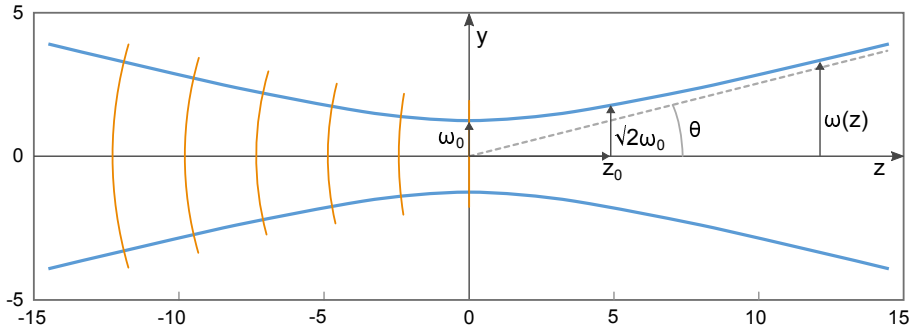


Figure 10: Cross section of a Gaussian beam focused at $z = 0$. Gaussian beam radius $\omega(z)$ (blue) and wavefront curvature (orange) as a function of the propagated distance $z$. Beam waist $\omega_0$, half divergence angle $\theta$ and a Rayleigh range $z_0$ are marked.

with the peak amplitude $|E_0|$, wavenumber $k = 2\pi/\lambda$, beam waist radius $\omega_0$, wavefront curvature radius $R(z)$ and the Rayleigh length $z_0$

$$z_0 = \frac{\pi\omega_0^2}{\lambda}. \tag{8}$$

Such electric field distribution satisfies a solution of the paraxial Helmholtz equation. The optical intensity has also a Gaussian radial distribution, given by

$$I(r,z) = |E(r,z)|^2 = I_0 \left(\frac{\omega_0}{\omega(z)}\right)^2 \exp\left(-\frac{2r^2}{\omega^2(z)}\right). \tag{9}$$

In every cross section, intensity reaches the maximum on the $z$ axis and decreases to $1/e^2 \approx 13.5\,\%$ of its maximal value at the radial distance $r = \omega(z)$ (Fig. 10). The quantity $\omega(z)$ is one of the definitions of the beam radius, with a corresponding beam diameter $2\omega(z)$ often called a spot size. Its dependency on the $z$ coordinate is given by

$$\omega(z) = \omega_0\sqrt{1 + \left(\frac{z}{z_0}\right)^2}. \tag{10}$$

A circular on-axis aperture with a radius $\omega(z)$ will transmit $86.5\,\%$ of the total beam power. This fraction increases to $98.9\,\%$ and $99.97\,\%$ for aperture radii of 1.5 and 2 times $\omega(z)$, respectively. The beam diameter reaches a minimum of $\omega_0$ at $z = 0$ (beam waist, focal plane), a value $\sqrt{2}\omega_0$ at $z = z_0$ and converges to an asymptotic behavior in the far field

$$\omega(z) \approx \frac{\omega_0}{z_0} z = \theta_0 z, \tag{11}$$

where a paraxial approximation $\tan(\theta) \approx \theta$ is used. Rewriting this equation, we find the beam divergence angle $\theta$ (and a full divergence angle $2\theta$, Fig. 10)

$$\theta = \frac{\lambda}{\pi\omega_0}. \tag{12}$$

For a given wavelength, this means the larger the far field divergence, the smaller is the beam waist. Finally, the parabolic wavefront curvature $R$ that evolves in $z$ according to

$$R(z) = z\left(1 + \left(\frac{z_0}{z}\right)^2\right). \tag{13}$$

The curvature is infinite, as for a plane wave, at the beam focus. It decreases to the minimum value of $R = 2z_0$ at $z = z_0$, and for $z \gg z_0$ approaches an approximately spherical wavefront $R(z) \approx z$. Phase curvature plays a role for example in interactions involving excitation of plasmons and therefore influences formation of LIPSS [113]. The beam size is commonly adjusted via focusing optical elements. Considering a beam of a diameter $D$ being focused by a circular lens with a focal distance $f$, the resulting focal spot size can be approximated by

$$2\omega_0 = \frac{4\lambda}{\pi}\frac{f}{D}M^2 \tag{14}$$

together with the depth of focus, defined here as an extension of one Rayleigh length on both sides of the beam waist position

$$\mathrm{DOF} \equiv 2z_0 = \frac{\pi\omega_0^2}{\lambda M^2} = \frac{8\lambda}{\pi}\left(\frac{f}{D}\right)^2. \tag{15}$$

All the aforementioned relations apply only within a frame of the paraxial approximation, i.e. while $2\theta < 30°$ [112]. For tightly focused beams, a more complex calculations based on the full Helmoltz equation are required.

Real laser beams show some deviation from the ideal Gaussian behavior. The $M^2$ beam quality factor, used to compare focusing performance of a real laser beam with that of a diffraction-limited Gaussian beam, is defined as a ratio of the beam parameter products of a real beam to an ideal one:

$$\mathrm{M}^2 = \frac{\theta\omega_0}{\lambda/\pi} = \frac{\text{real beam}}{\text{ideal beam}} \geq 1 \tag{16}$$

A truly Gaussian beam with $M^2 = 1$ will result in the smallest focal spot size. Commercial ultra-fast laser systems usually fall into a region of $M^2 = 1.1$ – 1.3.

Gaussian beams can be also astigmatic/elliptical and have different radii and divergence values for two perpendicular transverse directions. Equations similar to those above can be used for describing the independent evolution of the beam radii in both directions.

### 2.1.3 Gaussian beam spot size and damage threshold

Laser-matter interaction studies require precise quantification of laser intensity and fluence (i.e. energy per unit area) on the target. Their accuracy depends on a measurement of the laser energy and on a measurement of the laser beam spot size.

Characterizing the spot size, however, might not be simple. It depends on a definition of the beam diameter $D$, absolute beam diameter to be measured and possession of appropriate equipment. Four common diameter definitions exist: the full width half-maximum, $D_{\mathrm{FWHM}}$, where the diameter of the beam intensity distribution is measured at half of its maximum; the $1/e$ definition $D_{1/e}$, but more common is the $1/e^2$ definition, $D_{1/e^2} = 2w_0$, which was already discussed in the previous section and is used within this work. The fourth, more general definition, denoted D4$\sigma$, is based on the second moments of the intensity distribution function. For an ideal Gaussian beam the calculated width is identical to the $1/\mathrm{e}^2$ criteria. Mentioned definitions are compared in the Tab. 2.

| Beam width definition | Relative width |
|---|---|
| $D_{\mathrm{FWHM}}$ | $\sqrt{\ln(2)/2} \approx 0.589$ |
| $D_{1/\mathrm{e}}$ | $1/\sqrt{2} \approx 0.707$ |
| $D_{1/\mathrm{e}^2}$ | 1 |

Table 2: Comparison of the beam width definitions for an ideal Gaussian beam, relative to the $1/e^2$ definition.

All the aforementioned definitions can be simply applied to a beam image captured by a beam imaging device (a beam profiler). A problem arises for focused beams, when the beam size approaches the size of the profiler pixels and when the characterization should be done on an actual sample surface at a given focal position. In this case, a different approach must be chosen.

#### 2.1.3.1 $D^2$ vs $\ln(E)$

A widely used solution for spot size characterization, for pulsed lasers with a Gaussian output beam, is by measuring diameters of the laser-modified surface spots at variable pulse energy (and fluence) [114]. Broad range of materials, which exhibit a well observable and sharp threshold modification process, can be used for this purpose. A well polished surface is also favorable. The first such proposed material, a single-crystal silicon wafer undergoing a well-defined phase transformation, is still being utilized for this purpose.

The Gaussian beam intensity (Eq. 9) can be rewritten using laser fluence $F$, defined as the deposited energy per area in J/cm$^2$, in the form

$$F(r,z) = F_0(z) \exp\left[-2\left(\frac{r}{\omega(z)}\right)^2\right], \tag{17}$$

with the on-axis peak fluence $F_0$. Figure 11 demonstrates such fluence distribution around the beam waist. Integrating this equation over the whole beam cross section gives a connection between the peak fluence $F_0(z)$ and the measured pulse energy $E_{\mathrm{pulse}}$

$$\frac{2E_{\mathrm{pulse}}}{\pi\omega^2(z)} = F_0(z). \tag{18}$$

Let us assume the spot size measurement (in the $1/\mathrm{e}^2$ definition) is held on a material with a modification threshold fluence $F_{\mathrm{th}}$ and at a focal position ($\omega(z) = \omega_0, F_0(z) = F_0$). A single irradiation pulse creates a circular modified area with a radius $r$, which can be expressed from Eq. 17 as

$$r^2 = \frac{1}{2}\omega_0^2 \left(\ln F_0 - \ln F_{\mathrm{th}}\right) = \frac{1}{2}\omega_0^2 \left(\ln E_{\mathrm{pulse}} - \ln E_{\mathrm{th}}\right), \tag{19}$$

with $E_{\mathrm{th}}$ being the lowest pulse energy causing an observable surface modification. Finally, substituting for the $F_0$, a generally known form of the $D^2$ vs $\ln(E)$ relation is obtained:

$$D^2 = 2\omega_0^2 \left(\ln\left(\frac{2E_{\mathrm{pulse}}}{\pi\omega_0^2}\right) - \ln F_{\mathrm{th}}\right). \tag{20}$$

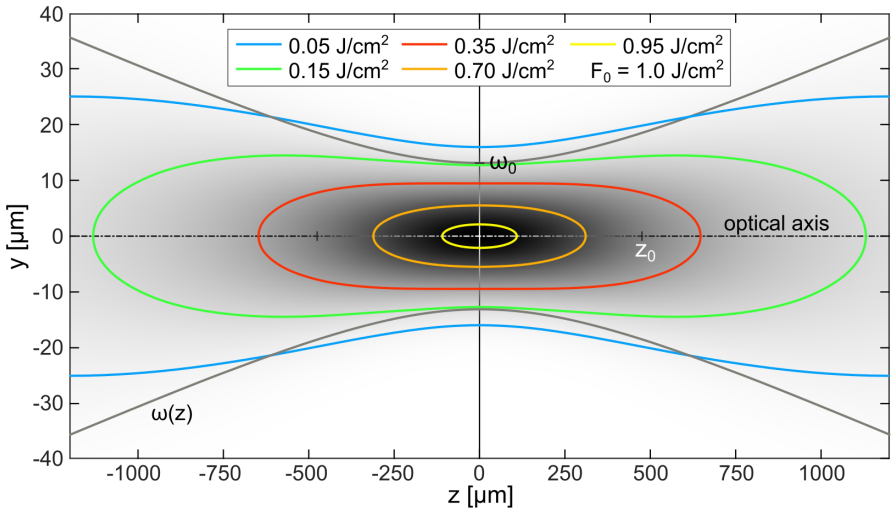


Figure 11: Laser fluence distribution in proximity of the Gaussian beam waist for the laser parameters of $\lambda = 1030$ nm, $\omega_0 = 13.1\,\mu$m, $z_0 = 477\,\mu$m, $E_{\text{pulse}} = 2.7\,\mu$J, $1/e^2$ input beam diameter 5.5 mm, focal length 100 mm, $M^2$=1.1. Peak fluence in the focal plane is $F_0 = 1.0$ J/cm$^2$.

In the case of an astigmatic beam (i.e. $\omega_{0x} \neq \omega_{0y}$), a substitution $\omega_0^2 = \omega_{0x}\omega_{0y}$ is made. In general, every beam is slightly irregular. Measuring a modified area $A_{\text{mod}}$ and defining the modified diameter as $D^2 \equiv 4A_{\text{mod}}/\pi$ yields a more robust method.

The Eq. 20 is used directly or in a linear form $y = Ax + B$ after the following substitutions:

$$\begin{aligned} y &= D^2 & A &= 2\omega_0^2 \\ x &= \ln\,(E_{\text{pulse}}) & B &= -2\omega_0^2 \ln(E_{\text{th}}) \end{aligned} \tag{21}$$

The actual spot size measurement is based on repeated single-pulse irradiation of pristine material by pulses of different energy close to the $F_{\text{th}}$. The resulting dataset of $(D_i^2, \ln(E_{\text{pulse,i}}))$ is then fitted by a linear regression, as demonstrated in Fig. 12, to obtain the $A$ and $B$ parameters. Finally, from these the $F_{\text{th}}$ and $\omega_0$ are retrieved by Eq. 21.

For completeness of the measurement, measurement error is estimated. The error values $\Delta A$ and $\Delta B$, from the linear regression, are used to derive the errors as

$$\begin{aligned} \omega_0 &= \sqrt{\frac{A}{2}} \\ \Delta\omega_0 &= \left|\frac{\partial \omega_0}{\partial A}\right| \Delta A = \frac{1}{2}\frac{1}{\sqrt{2A}}\Delta A \end{aligned} \tag{22}$$

$$\begin{aligned} F_{\text{th}} &= \frac{2E_{th}}{\pi\omega_0^2} = \frac{4}{\pi}\frac{e^{-B/A}}{A} \\ \Delta F_{\text{th}} &= \sqrt{\left(\frac{\partial F_{\text{th}}}{\partial A}\right)^2 (\Delta A)^2 + \left(\frac{\partial F_{\text{th}}}{\partial B}\right)^2 (\Delta B)^2} \\ &= \frac{4}{\pi}\sqrt{\left[\frac{e^{-B/A}}{A}\left(\frac{B}{A} - 1\right)\right]^2 (\Delta A)^2 + \left(\frac{e^{-B/A}}{A^2}\right)^2 (\Delta B)^2} \end{aligned} \tag{23}$$

The estimated error of the $F_{\mathrm{th}}$ should be actually non-symmetric, due to linear regression of the data with an $x$-axis being a logarithm of the pulse energy, however the usual non-symmetricity of a few percent can be neglected.

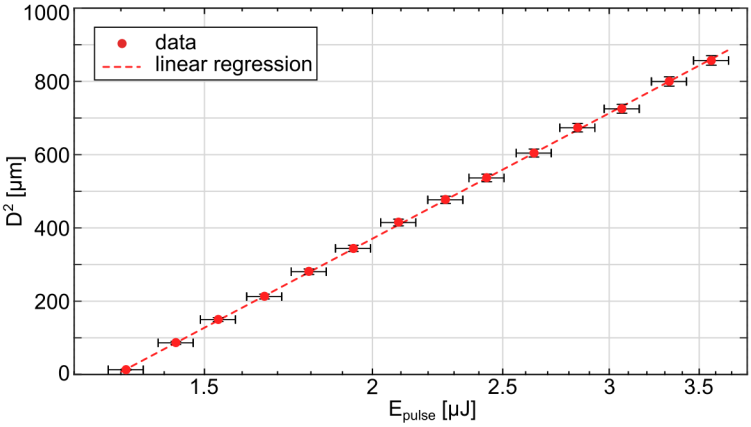


Figure 12: A measurement of the Gaussian beam spot size and damage threshold fluence on a single crystal silicon with a fit given by Eq. 20 ($\omega_0 = 20.52 \pm 0.04\,\mu$m, $F_{\mathrm{th}} = 0.195 \pm 0.05$ J/cm$^2$). Errorbars assume a $\pm 3$ % detector tolerance and $\pm 6$ pixel spot diameter readout error.

#### 2.1.3.2 Other phenomena and limitations

***Self focusing***

An intense electromagnetic field of ultra-short laser pulses can easily trigger strong nonlinear material response. For example, a Kerr nonlinearity causes dependence of the refractive index of the propagation medium $n$ on an electromagnetic field intensity $I(r,t)$ as $n = n_0 + n_2 I(r,t)$. Initial refractive index $n_0$ is usually increased by a nonlinear Kerr index $n_2$. As the intensity of a Gaussian beam is the highest on the axis, the non-linearly increased refractive index will be the highest on the axis as well. This lensing effect leads to the beam self-focusing and filamentation. Despite the fact that this effect is dependent on the field intensity, initial power of the beam $P_{\mathrm{in}}$ is more significant parameter. If the initial power exceed a *critical power* [115]

$$P_{\mathrm{cr}} = 0.146\lambda^2/(n_0 n_2), \tag{24}$$

self-focusing overcomes diffraction and the beam collapses. This occurs, for example, in air at $P_{\mathrm{cr}} \approx 3.2$ GW at 800 nm [116] or at 4.3 MW (1064 nm) and 1.98 MW (800 nm) in fused silica [117, 118]. Even though monchromatic light is assumed here, this equation is often used also for self-focusing estimation of ultra-short laser pulses, where dispersion effects, decreasing the peak pulse amplitude, must be considered. Experimentally, self-focusing is manifested in the beam diameter variation and in a change of the effective focal distance of lenses. The propagation distance $f_c$ of an initially collimated beam before its collapse by self-focusing is expressed semi-empirically as [116, 119]

$$f_c = \frac{0.367 z_0}{\sqrt{\left[(P_{in}/P_{cr})^{1/2} - 0.852\right]^2 - 0.0219}}. \tag{25}$$

Such focusing will also reduce focal distance of a lens with focal distance $f$ to an effective focal distance $f_{\text{eff}}$ given by a lens equation

$$\frac{1}{f_{eff}} = \frac{1}{f_c} + \frac{1}{f}. \tag{26}$$

***Limits of the $D^2$ vs ln($E$) method***

Returning back to the $D^2$ vs ln($E$) technique. In summary, it is commonly used in the Community and has the advantage of accurately measuring the spot size (and the material damage threshold) of the used focused beam on an actual sample surface. However it is good to keep in mind the possible limitations:

- It assumes a certain fluence dose is reached. However, the instantaneous power plays a significant role [120]. It is known that the damage threshold is strongly dependent on a pulse duration. It also depends on a temporal shape of the pulse.
- Changes in the surface reflectivity are not considered [62, 121].
- Energy diffusion/redistribution and heat affected zones are not considered.
- It is dependent on the damage definition. Damage is usually defined as a first permanent observable modification of the material (absorption, reflection, topography). However, by precise measurement of a refractive index change in Si [122], a damage threshold value 5× smaller than usually reported was obtained. Ellipsometric measurements of Si surface amorphization also give a significantly smaller value [123].
- The method starts to deviate from the relation given by Eq. 20 for larger fluences of approx. 10× the damage threshold, where, due to onset of other damage processes or non-Gaussian profile at the beam perimeter, the slope of the fitting line changes.
- Not all damage processes, even though exhibiting a sharp modification threshold, such as ablation of a thin surface layers [124], can be used for this method.

Finally, it is important to mention that the damage threshold of a single material is not a constant, but depends on additional variables, such as:

- laser wavelength [125];
- pulse duration – strong dependency of the damage threshold on the pulse duration $\tau$ is observed from metals [121] to dielectrics [126–128] and polymers [129]. For $\tau > 20$ ps the damage is dependent as $\sim \tau^{1/2}$, corresponding to lattice thermal conduction, heat deposition and conventional melting. Sub-picosecond pulses deviate from this trend. Here, the damage is caused mainly by ablation dominated by multiphoton and collisional ionization [127];
- polarization type (linear / circular);
- pulse spatial profile and homogeneity (beam shaping, $M^2$, hot-spots);
- surface quality, polishing quality and polishing material [117, 130];
- doping / impurities / defects [131];

- material phase (crystalline / polycrystalline / amorphous) and density;
- crystal lattice orientation (Section 3.1.2);
- number of pulses (incubation effects) [29] and repetition rate;
- ambient environment, humidity, pressure of ambient gas [39];
- temperature [132];
- if volume or surface damage is measured (surface damage threshold of fused silica is reported to be 2-5× smaller due to polishing cracks and residues; good polishing decreases the difference [117]);
- surface coating – a natural oxide layer or dielectric coating can increase surface quality, modify surface reflectivity [124]. These affect both, the measured damage threshold and the beam diameter;
- choice of a particular damage threshold process, if several coexist.

We had studied experimentally the effect of the surface coating and a choice of the damage threshold process on damage threshold and spot size measurement on silicon surface coated with a native and an artificial (300 nm) layer of $SiO_2$. In the published paper [133] we show, that the measured spot size exhibits an increasing trend with increasing threshold fluences associated with different damage threshold processes. Use of the lowest damage threshold process provides results closest to the theoretical values of the laser spot size for both surface coatings. Another result is that the sample with the native oxide layer exhibits generally smaller damage thresholds for all studied damage processes (e.g. amorphization, melting). This is despite the fact of 4 % smaller static reflectivity of the sample with 300 nm oxide layer. In the case of this sample, the measured spot size increased by 32 % (in contrast to 3 % for the sample with the native oxide) when different damage threshold fluences were examined. One of the possible explanations could be a confinement of deposited pulse energy within the Si-$SiO_2$ interface, that spreads laterally and seemingly increases the modified area.

### 2.1.4 Beam shaping

#### Beam shaping in general

The Gaussian beam profile, though dominant in laser material processing, is one of many possible laser beam spatial distributions. Conversion between such distributions, beam shaping, has an increasing trend in the scientific and industrial applications. The resulting large variety of shaping approaches and beam shapes makes it difficult to provide a full overview of the whole topic. It can be found in dedicated literature, e.g. [134]. Therefore, the following text will focus only on the beam shaping methods used within the experimental part.

While the Gaussian beam is the commonly encountered transverse intensity distribution with several beneficial properties in generation, propagation and focusing, it is not necessarily the ideal shape for laser applications. As illustrated in Fig. 13, high on-axis intensity can cause excessive ablation and material damage. Diffused energy together with the low energy outer portion of the beam often cause adverse thermal effects, usually termed as heat affected zone (HAZ). To overcome such problems, other beam shapes

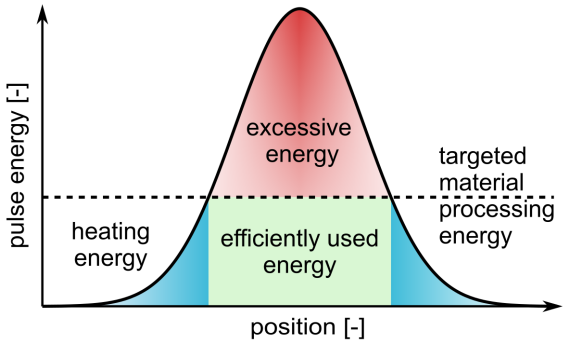


Figure 13: An illustration of Gaussian pulse energy utilization in laser-material processing.

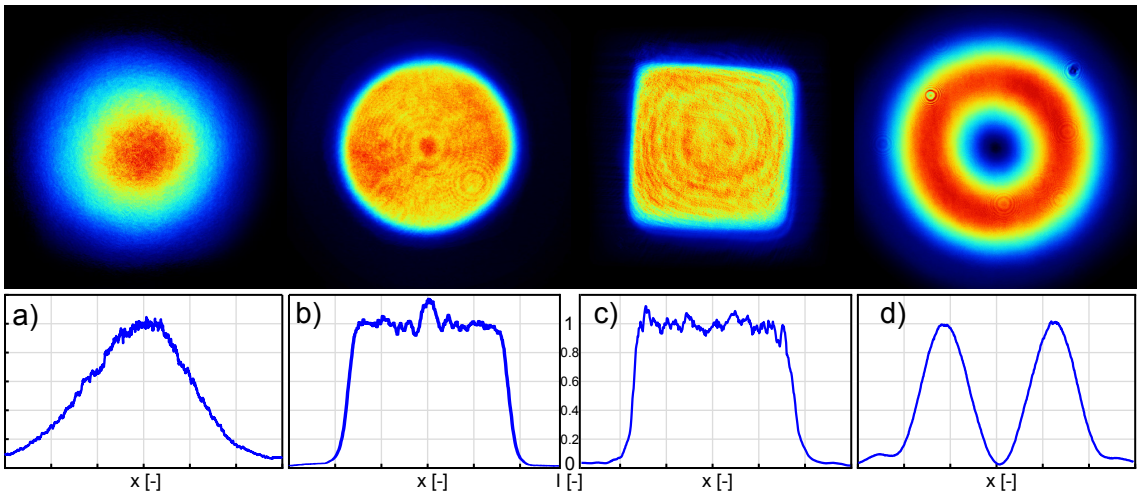


Figure 14: Common laser beam profiles obtained experimentally and imaged with a beam profiler (Cinogy CMOS-1.001 Nano): a) Gaussian beam, b) circular flat-top beam, c) square flat-top beam and d) Laguerre-Gaussian (doughnut) beam. Size and intensity are normalized.

should be used. There are endless variations of the intensity distribution, however, mostly a few basic non-Gaussian beam-shapes are actually used. For example flat-top (top-hat) beams (Fig. 14b-c) with constant intensity over the profile, advantageous in homogeneous surface structuring and micromachining [135,136], Bessel beams with non-diffracting central part, or vector and vortex "doughnut" beams (Fig. 14d) with zero on-axis intensity. Some of them are compared to the Gaussian beam in the Fig. 14. Beamshaping elements used are specified in the first three rows of the Tab. 3.

Experimental laser beams used to be mostly considered as scalar optical fields with uniform polarization in the transverse plane. However, in the past two decades, so-called *vector beams*, beams where the light polarization in the beam transverse plane is space-variant [137], started to gain attention. In particular, cylindrical beams with an on-axis singularity, leading to a zero on-axis intensity. This singularity can be either vectorial (e.g. radial / azimuthal polarization) or also related to the optical phase, creating co-called *vector vortex beams*.

The above mentioned spatial beam distributions and shaping techniques represent the frequently used ones. However, more unique and application specific beam shaping

| Beam shape | Method | Element |
|---|---|---|
| square | energy redistribution (mapping) | free-form optic (GTH-5-250-4, Eksma) |
| circular | spatially variable transmission filter | spatially variable L/2 + polarizer (RPC-1030-06-661, Workshop of Photonics) |
| doughnut | spatially variable polarization modulation | spatially variable L/2 (RPC-800-12-662, Workshop of Photonics) |
| square (in focus) | diffraction | free-form surface (FBS2-1030-5, Eksma) |

Table 3: Beam shaping methods used to obtain square, circular, doughnut and in-focus square beam from an input Gaussian beam.

techniques exist, along with techniques based on diffraction elements and Spatial Light Modulators (SLM) capable of shaping beams arbitrarily in real time. To some extent, it is also possible to combine the beam-shaping methods (spatially variable waveplate + axicon [138]) or to have different intensity distributions (flat-top – Gaussian – doughnut) at different working distances [139].

### Beam shapers employed in this work

In this work, four particular beam-shaping elements were used experimentally to generate a square flat-top, a circular flat-top and a radially and azimuthally polarized doughnut beam. These beam shapes are summarized in the Tab. 3, together with the employed beam shaping method and a reference of the actual optical element. The following subsections discuss them in detail.

### Square flat-top

Flat-top beams aim at high homogeneity of modification and avoiding of damage to the adjacent material. Furthermore, the homogeneous energy distribution allows to reduce the pulse-to-pulse overlap and thereby to increase processing speed.

The first tested element was a beam-shaping lens (GTH-5-250-4), a free-form optics shaped to redistribute (map) the input Gaussian power distribution into a square flat-top one. As the energy is redistributed in a non-homogeneous way, the spot size of the input Gaussian beam must match the size for which the beam-shaper was manufactured. An integrated lens results in a $4\times4$ mm$^2$ square profile to be generated at a distance of 25 cm after the shaper for a collimated beam ($5.0 \pm 0.15$ mm, $1/e^2$) on the input. Figure 15 shows the evolution of the spatial distribution of the initially Gaussian beam after the shaper as a function of distance.

Variation of the input beam divergence affects size and position of the shaped beam. Unfortunately, this construction of the beam shaper results in two problems for microprocessing. The position of the shaped beam is actually before the focus of a focusing lens and consequently its size is much larger than a focal spot of a Gaussian beam focused by the same optic. Although, it is possible to demagnify the profile by additional optics, it complicates the setup.

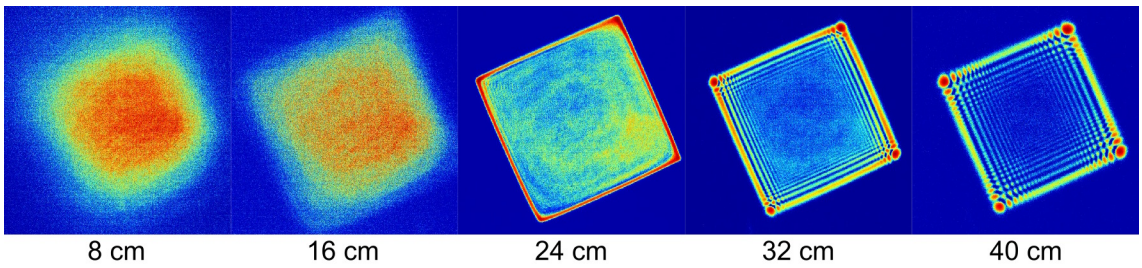


Figure 15: Evolution of the beam profile after the beam shaping element. The input Gaussian beam is redistributed (mapped) to a flat-top profile by a beam shaping lens. Corresponding distances from the element are indicated, no additional optics were used. Size of the square at 24 cm is ∼4×4 mm$^2$ (@ 1030 nm, imaged with a beam profiler Cinogy CMOS-1.001 Nano).

### Circular flat-top

The second used beam shaping approach is utilizing a space-variant transmission filter. More precisely, a spatially variable waveplate (s-waveplate) followed by a polarizer. The s-waveplate (RPC-1030-06-661, Workshop of photonics) is inscribed inside a bulk of fused silica glass by femtosecond laser pulses [108]. During the fabrication, orientation of birefringent laser-induced self-assembled periodic nanostructures is controlled in order to produce the necessary radial distribution of polarization. Following linear polarizer affects the resulting transmission. The same construction is also used for other types of converters. All such converters have relatively high damage threshold (2.2 J/cm$^2$ @1030 nm, 212 fs) and are suitable for high-power laser systems [140]. A drawback is lower efficiency of 50–70 %, which is a large difference compared to the previous energy redistributing type claiming an efficiency up to 95 %. Both input and output beams are linearly polarized.

### Doughnut beam

Another beam-shaping option is conversion of a linearly polarized Gaussian beam into a radial or azimuthal polarization vector beams. The beam-shaping element could be again an s-waveplate manufactured by volumetric inscription of birefringent nanogratings [108, 141] as mentioned above or a liquid crystal polymer film, where orientation of the fast axis is a function of the azimuthal coordinate.

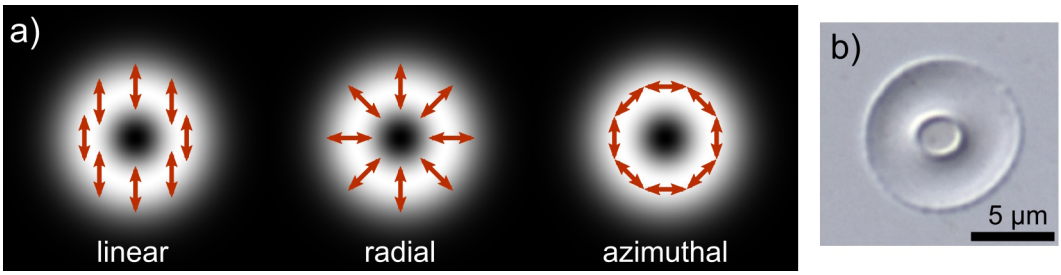


Figure 16: a) The amplitude (white color) and the direction of the polarization states of a hollow core doughnut beam. b) Optical microscopy image of a laser ablation spot on silicon by a focused (10x, 0.12 NA objective) radially polarized beam.

For the first-order s-waveplate used, direction of the input linear polarization selects between radial (horizontal input) and azimuthal (vertical input) output polarization.

Nonetheless, generation of both radially and azimuthally polarized beam automatically leads to creation of polarization singularity on the beam axis and zero on-axis intensity. Such hollow-core (Laguerre–Gaussian) beam is often called a *doughnut* beam.

The doughnut beam can be also created by the previously mentioned method of spatially variable transmission filter. In this case, the output polarization will be linear. A comparison of three polarization states of a doughnut beam is presented in Fig. 16a.

When a collimated linearly-polarized doughnut beam is focused by a lens, the focal spatial distribution, being a Fourier transform of the input beam, is no longer a doughnut beam. On the contrary, for radial and azimuthal polarization, due to the on-axis polarization singularity, the hollow core will be retained. This is demonstrated in Fig. 16b, showing a focused doughnut beam from Fig. 14d. The central part is left unmodified. However, it should be noted that under tight focusing conditions (NA $>\sim 0.4$), radially polarized beam will have a significant on-axis intensity due to an on-axis component of the polarization [142].

**Square flat-top (FBS)**

Another beam shaper used implements a so called Fundamental Beam-mode Shaping (FBS) [135]. A litographically produced FBS-type diffractive optical element represents a phase plate with a continuous and smooth phase relief. It transforms an input Gaussian beam to a $\mathrm{sinc}(x)\times\mathrm{sinc}(y)$ type beam (Fig. 17a), which, once focused, produces a flat-top profile (Fig. 17c). A layout of the beam-shaping setup is illustrated in Fig. 17b. The distance between the FBS and a focusing lens is not critical. Unlike the first square flat-top element, by this approach the smallest achievable flat-top size is $\sim 1.5\times$ of the diffraction limited Gaussian spot under the same focusing conditions. Fig. 17d demonstrates this by comparing a focused Gaussian beam with a focused shaped beam. The FBS shaper can be combined with any objective or an f-theta lens. The element, is also manufactured for a specific beam size. A benefit is that the input beam does not need to be collimated. Therefore, it can be located between two lenses inside a beam expander, where the input beam size can be easily adjusted; as well as it can be placed after a focusing lens.

### 2.1.5 Scanning devices, synchronization

Laser material processing is typically conducted on a larger areas than a single laser spot. Therefore it is necessary to scan the laser beam across the material. There are several options how to do so, for example by piezo scanners, micro electro-mechanical system scanners, electro-optic or acousto-optic deflectors, but mostly two methods, i.e. scanning by a galvanometer/polygon scanner or by linear stages, are used. The latter two were used also within the experimental part here. The following sections will introduce basic parameters characterizing the laser scans and main properties of these two scanner types, including some aspects of their synchronization.

**Laser-scanning patterns and parameters**

In general, the scanners allow for arbitrary paths to be scanned, but we will focus on regularly distributed laser pulses over the sample surface, and more precisely on their distribution into rectangular or hexagonal grid (see Fig. 18). Assuming a rectangular

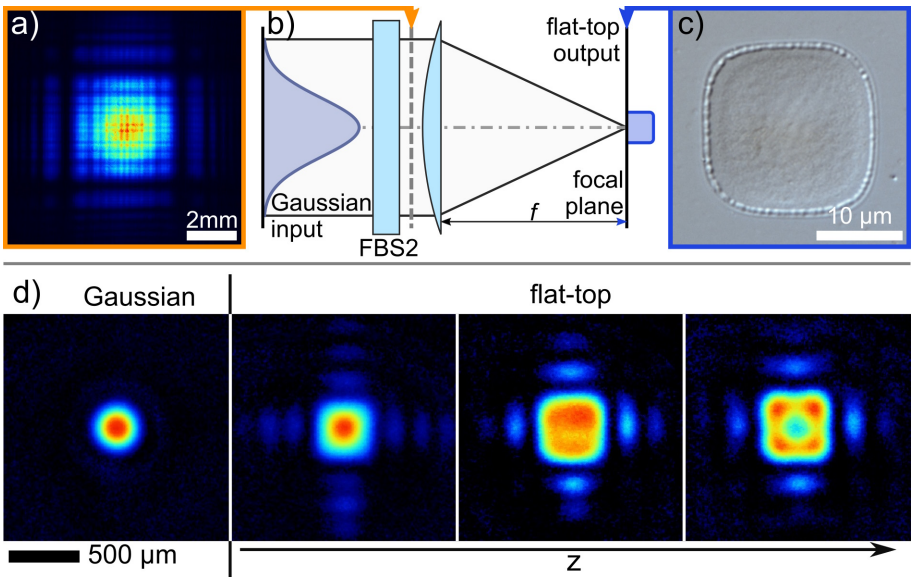


Figure 17: a) A beam profile of the shaped beam after the FBS element. b) Usage of a fundamental beam-mode shaping element (FBS). Adapted from [135]. c) Surface ablation spot by the shaped beam on a silicon surface. d) Comparison of a focused Gaussian beam with a focused flat-top beam. The flat-top beam is imaged at three positions after the focusing lens ($f = 1$ m).

geometry pattern and a Gaussian beam with a beam diameter $2\omega_0$, by scanning successive lines along $x$, then in-line ($\Psi_x$) and inter-line ($\Psi_y$) scanning overlaps can be defined as

$$\Psi_x \equiv \left(1 - \frac{d_x}{2\omega_0}\right) \times 100\,[\%] = \left(1 - \frac{v}{2\omega_0 f_{\text{rep}}}\right) \times 100\,[\%] \tag{27}$$

and

$$\Psi_y \equiv \left(1 - \frac{d_y}{2\omega_0}\right) \times 100\,[\%], \tag{28}$$

where $v$ denotes the $x$–velocity of the scanning, $f_{\text{rep}}$ is a laser repetition frequency and $d_{\text{x,y}}$ is a pulse spacing defined in Fig. 18.

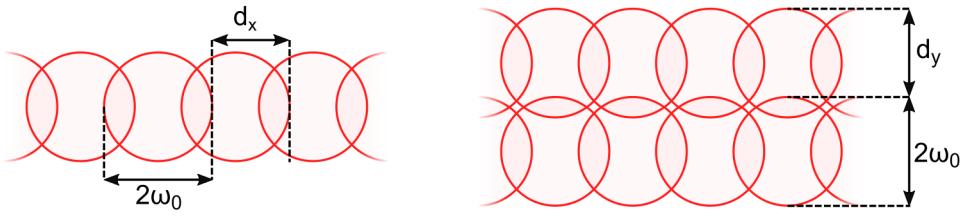


Figure 18: In-line and inter-line overlap of Gaussian pulses scanned in a rectangular grid.

### Scanning devices

*Galvanometer scanner* (galvo) is a laser scanning device based on a pair of laser-steering mirrors. Figure 19a shows a typical beampath with a galvanometer scanner. Figure 19b schematically illustrates a galvanometer scanning unit internally. Input laser

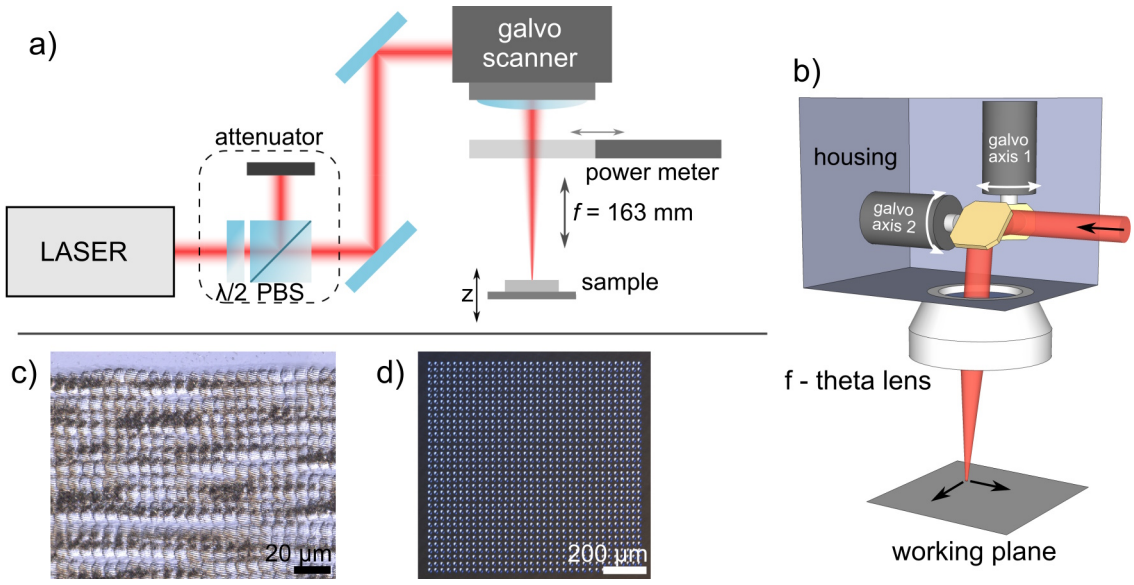


Figure 19: a) A simplified schematic of the galvo scanner beampath. b) Schematic drawing of a galvo scanner unit. c) Densely scanned area with an average in-line spacing of 7 $\mu$m. Lack of laser positioning precision causes beam oscillations and disrupts homogeneity of the scanning. d) Large area, low-overlap laser-scanned area with equidistantly spaced pulses.

beam is reflected by a pair of mirrors, that are mounted on rotating galvanometric motors. Axes of these motors are perpendicular with default positions causing two 90° beam reflections. After that, the beam is focused by a special objective termed f-theta lens, which translates the angularly steered beam into an $x$-$y$ position on a flat working plane. Its main advantage is speed of the scanning (typically several meters per second) on a relatively large area ($\sim 10 \times 10\,\mathrm{cm}^2$). A drawback is that the beam shape on the working plane gets increasingly distorted with an increasing beam deflection angle, unless a more expensive telecentric lens is used.

In our experiments mostly a galvanometer unit SCANcube III (Scanlab) with a RTC5 PCI board was used. The PCI board allowed for synchronization with a laser for repetition rates of 50 kHz and above. To control the scanner, a native Scanlab's laserDESK software was used. Main parameters of the scanner are summarized in the Tab. 4.

Unfortunately, the scanner may exhibit oscillations, probably around the last significant bit of its 16 bit encoded position. This is demonstrated in Fig. 19c, during scanning of successive horizontal lines at 50 kHz laser pulses over $SiO_2$ surface. Clearly visible oscillations at ∼2.4 kHz are disabling controlled energy deposition and failing the experiment. A shorter focal length lens can increase the positioning accuracy, but that contradicts the benefit of the high scanning speed. On the other hand, positioning precision across larger scanning field is acceptable (Fig. 19d).

### Scanning with linear $x$-$y$ stages

In our case, after the unfavorable results from the galvo scanner, we proceeded with the other extensively used laser scanning (or precisely sample positioning) method, i.e. by a linear stage scanning. The Fig. 20 shows an image and a sketch of the in-situ setup that I developed during this work, where two DDS100/M (Thorlabs) stages with KBD101

| | SCANcube III 14 (galvo) Scanlab | DDS100/M (linear stage) Thorlabs | 8MTL120XT (x-y planar stage) Standa |
|---|---|---|---|
| Focal length | 163 mm | any | 0 - 150 mm |
| Scan area | 10x10 $cm^2$ (for 1064 nm, f = 163 mm) | 10x10 $cm^2$ | 12x12 $cm^2$ |
| Wavengths | 1030 + 515 nm | any | 1030 + 515 nm |
| Max. speed | 2 m/s | 0.5 m/s | 1 m/s |
| Positioning resolution | ~1.6 µm (see text) | 500 nm | ≥ 25 nm |
| Bidirectional repeatability | < 2 µrad (RMS) | ± 1.5 µm | ± 0.1 µm |
| Absolute accuracy | ~ 2 µm | ± 6.5 µm | ± 0.5 µm |
| Minimum step | ~1 µm | ~ 5 µm | < 150 nm |
| Motor type | galvanometric | brushless direct drive linear | |
| Max. load | - | 0.9 kg | 30 kg |
| Synchronization to laser | yes (for $f_{rep} \geq 50$ khz) | no | partial (see text) |

Table 4: Parameters of the main three scanning systems used (SCANcube III 14 galvo scanner, DDS100/M (Thorlabs) linear stage and 8MTL120XT (Standa) $x$-$y$ planar stage).

(Thorlabs) controllers were used in an $x$-$y$ configuration.

In this setup, the dichroic mirror, which is actually a standard ultra-fast IR mirror with a polished back side, reflects the beam towards the focusing lens and the sample. An optional $\lambda/2$ waveplate is used to rotate the beam polarization, to adjust an angle between scan direction and polarization, as the stages can scan only in one direction (upper stage). Vertical focusing onto the sample is done by two linear stages, manual and a PC controlled one, but a quick coarse adjustment by moving the whole lens tube within its holder is also possible. The sample is mounted on a tilt-adjustable magnetic mount made out of a lightweight kinematic mirror holder, not to overload the lower stage. The imaging part consists of a green 1 W LED, which illuminates the sample through the focusing lens, which also serves as an objective for the camera.

Main parameters of the stages used are also summarized in the Tab. 4. The stages can be controlled in two ways, manually by an APT (Thorlabs) software, or to perform $x$-$y$ scanning by user-defined scripts (Matlab) which is the approach adopted here.

Through the experimental investigation it was found, the minimum step size is actually significantly smaller around 1 $\mu$m, but reaching the position takes a few seconds. Therefore, in terms of positioning precision, two such stages in an $x$-$y$ configuration will outperform the galvo when scanning closely spaced straight lines.

At the end of the PhD study, a second $x$-$y$ linear stage scanning system was obtained,

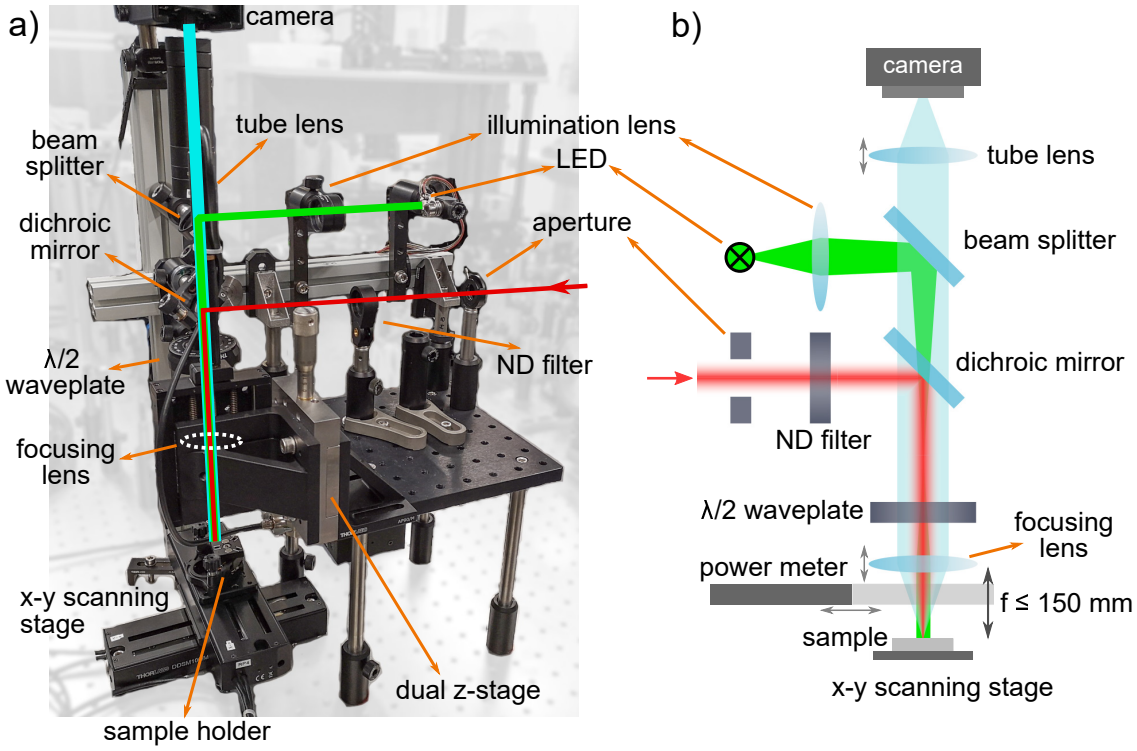


Figure 20: a) An optical setup for laser microprocessing with an in-situ visualization developed during the PhD. b) A schematic sketch of a).

Figure 21: Commercial in-situ micromachining setup.

as a part of a commercial $x$-$y$-$z$ micro-processing station (Direct Machining Control, LT) (Fig. 21). The 8MTL120XT (Standa) planar $x$-$y$ linear stage is driven by an 8UMC-16-3 motion controller and a DMC software interface. Main parameters of the stage are again summarized in the Tab. 4. This system is superior to the two previously mentioned in terms of positioning precision / accuracy, available software and an ability to directly control the laser functionality.

**Synchronization**

During the experiments it was found that good positioning parameters of the scanning systems on their own are only a part of the success for regular laser-surface processing and the possibility to synchronize a scanner with laser pulses plays often a crucial role. By synchronization we understand here a capability of the scanning system to deliver the laser pulses in particular positions along the motion trajectory. Specifically, to distribute the pulses equidistantly along a scanning line, where the first pulse will be at a predefined distance from the start of the line. This enables us to uniformly distribute laser energy over a surface in a regular grid of laser spots. Such synchronization is mainly a question of the hardware support. The galvo scanner controller has such support, but only for laser repetition rates of 50 kHz and above. The controller of the 8MTL120XT $x$-$y$ stage supports synchronization at any frequency but without a possibility to align the very beginning of the scan to a laser pulse. Finally, the controller of the DDS100/M stage has no default support. However, two general purpose input/output (GPIO) connectors can be used to trigger the laser, when a certain motion position is reached. Resulting pseudosynchronization (Fig. 22a) is discussed in detail in the Appendix E. Unfortunately, the laser pulses stay synchronized only in a proximity of the synchronization position (right side of the image) and the regular pattern gets misaligned with increasing distance due to non-repeatable scanning speed. Therefore, such (pseudo)synchronization is limited in space by the motion path repeatability.

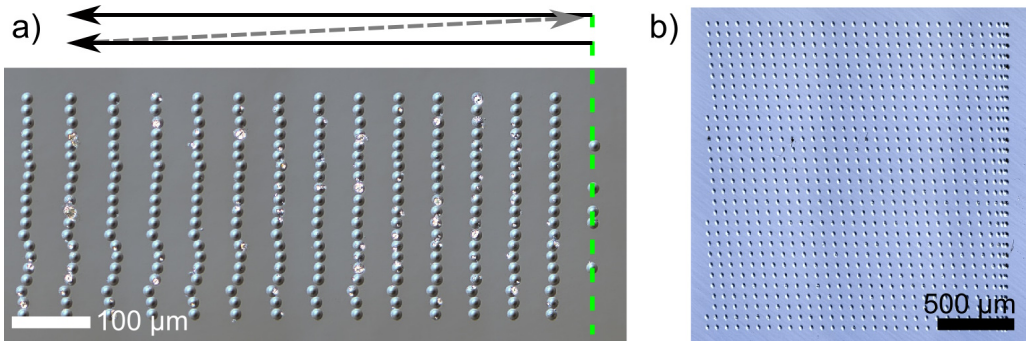


Figure 22: Pseudosynchronization: a) OM image of horizontal line scanning synchronized on the rightmost column (green dashed line). b) Spontaneous alignment of laser pulses with no laser-scanner synchronization arises from high motion repeatability of the galvo scanner.

A specific situation may arise for highly repeatable scanning systems (e.g. a galvo scanner) while filling a rectangular area by regular lines *without* synchronization with the laser. When each scan line takes exactly the same amount of time to be scanned an aligned pattern is produced (Fig. 22b). Moreover, in a particular case when time necessary to scan

a single line is exactly a whole-number multiple of interpulse delay ($1/f_{\mathrm{rep}}$) a rectangular scan pattern is obtained. By gently tuning the scanning parameters, this method can be used to "synchronize" the galvo scanner below the supported 50 kHz repetition rate.

## 2.2 Sample materials

Several target materials were used in the experiments. Table 5 lists most of these and summarizes in which experiments were the samples used. Parameters of the two most used materials, fused silica and silicon, are provided afterwards.

| **Material** | **Experiment** | **Note** |
|---|---|---|
| **fused silica** | LIPSS scanning | $F_{th} = 4.1$ J/cm$^2$ (1030 nm, 260 fs) |
| (bulk, thin layer) | thin layer DT / ablation | |
| | burst DT / ablation | |
| | N-on-1 DT | |
| | volumetric modif. (ns) | |
| ULE glass | LIPSS | $F_{th} = 3.6$ J/cm$^2$ (1030 nm, 260 fs) |
| | N-on-1 DT | |
| **silicon** | LIPSS | $F_{th} = 0.175$ J/cm$^2$ (800 nm, 37 fs) |
| | modification in mid-IR | $F_{th} = 0.194$ J/cm$^2$ (1030 nm, 260 fs) |
| | burst DT / ablation | $F_{th} = 0.285$ J/cm$^2$ (1030 nm, 1900 fs) |
| | N-on-1 DT | |
| | polariz. orientation DT | |
| germanium | modification in mid-IR | |
| Kapton (polyimide) | DT / ablation | $F_{th} = 0.66$ J/cm$^2$ (1030 nm, 250 fs) |
| | N-on-1 DT | $F_{th} = 2.35$ J/cm$^2$ (1030 nm, 7 ps) |
| polystyrene | DT / ablation | $F_{th} = 1.98$ J/cm$^2$ (1030 nm, 250 fs) |
| | N-on-1 DT | $F_{th} = 0.85$ J/cm$^2$ (515 nm, 250 fs) |
| PMMA (thin film) | DT / ablation | $F_{th} = 2.5$ J/cm$^2$ (1030 nm, 260 fs) |
| diamond (thin film) | DT / modification | $F_{th} = 1.4$ J/cm$^2$ (1030 nm, 260 fs) |
| titanium | LIPSS | |
| molybdenum (thin film) | LIPSS | $F_{th} = 1$ J/cm$^2$ (1030 nm, 1400 fs) |
| copper | burst DT / ablation | |

Table 5: A list of the materials used in the experiments.

### Fused silica and ULE glass

LIPSS scanning was attempted on fused silica and on ultra low thermal expansion (ULE) glass to investigate effect of thermal expansion on LIPSS formation. A damage threshold of the ULE glass was measured to be smaller than the one of the FS, but considering a lower annealing point of the ULE and a fact it is a doped material, such result can be expected. Table 6 summarizes parameters of both materials.

Silicon dioxide is an important, widely used material, which exist in crystalline and amorphous form. Several terms are used to describe $SiO_2$ based on its state and manufacturing process, which are often causing confusion. For example, terms fused quartz and

| | Corning® Fused silica | Corning® ULE glass |
|---|---|---|
| Density [g/cm$^3$] | 2.20 | 2.21 |
| Annealing point [°C] | 1180 | 1000 |
| Specific heat [J/(g.K)] | 0.77 | 0.76 |
| Thermal conductivity [W/(m.K)] | 1.38 | 1.31 |
| Thermal diffusivity [cm$^2$/s] | 7.5 $10^{-3}$ | 7.9 $10^{-3}$ |
| Mean coeff. of thermal expansion [1/K] | ~ $10^{-6}$ | ~ $10^{-9}$ |
| Refractive index (@589 nm) | 1.48 | 1.45 |
| Damage threshold [J/cm$^2$] (1030 nm, 260 fs) | 4.1 ± 0.4 | 3.6 ± 0.3 |

Table 6: Comparison of material properties of the fused silica and Ultra-Low Expansion (ULE) glass. Data source: Corning material data sheets.

| | |
|---|---|
| Silica | A general term for silicon dioxide. |
| Quartz | Crystalline form of silica. A typical form of the silica in nature. |
| Fused quartz<br>Quartz glass | Is made by fusing (electrically or by a flame) natural quartz powder. |
| Fused silica<br>Fused silica glass<br>(Flame) Synthetic fused silica | An amorphous material, that is produced synthetically from pure chemicals (typically tetrachlorosilane). Due to increased purity, it is has better optical properties (transmission) than the fused quartz [143]. |
| Fumed silica<br>Pyrogenic silica | Flame produced silica nanoparticle powder of low density. |

Table 7: A list of the $SiO_2$ material nomenclature.

fused silica are often interchanged. However, use of these is not unified and significant differences exist in its interpretation among individual manufacturers/sellers. In particular for the fused quartz, it can be found as both amorphous and crystalline material. Therefore, Tab. 7 presents a survey on the $SiO_2$ nomenclature, to understand, what material is actually used.

| | crystalline | amorphous |
|---|---|---|
| Density [g/cm$^3$] | 2.32 | 2.28 |
| Melting temperature [°C] | 1417 | 1147 |
| $E_g$ [eV] | 1.12 (indirect) | 1.53 (direct) |
| Thermal conductivity [W/(m.K)] | 150 | 1.8 |
| Thermal diffusivity [cm$^2$/s] | 0.85 | 0.0097 |
| Specific heat [J/(g.K)] | 0.71 | 0.8 |
| Bulk reflectivity [%] | 31.3 | 32.1 |
| Damage threshold [J/cm$^2$] | (100), B doped, 10 Ω/cm | |
| (800 nm, 37 fs) | 0.175 ± 0.002 | |
| (1030 nm, 260 fs) | 0.194 ± 0.001 | |
| (1030 nm, 1900 fs) | 0.285 ± 0.003 | |
| (1030 nm, 6000 fs) | 0.46 ± 0.02 | |

Table 8: Equilibrium optical [144] and thermophysical [145] properties of silicon. Optical properties are interpolated to the 1030 nm from available wavelengths.

### Silicon

Silicon was the main experimental material due to its superior surface finish, availability, and availability of theoretical models. Table 8 summarizes thermodynamical and optical properties of both forms, crystalline and amorphous. In addition, Fig. 23 illustrates typical marking of the silicon wafers and associated crystalline orientation of the (100) p-type wafer, used in a majority of the later experiments.

### Sample preparation

Monocrystalline silicon samples were cut from a 125 mm diameter wafer by first scribing the wafer by a diamond-tipped pen and than cleaving it into $\sim 25 \times 25$ mm$^2$ pieces. Glass samples already had similar dimensions from the manufacturer. In the next step, samples were cleaned by wiping them with a folded optical tissue soaked in a 1:1 mixture of acetone and isopropyl alkohol. For a more throughout cleaning, the sample was inserted in a glass beaker, submerged in a deionized water with a kitchen detergent and sonicated in an ultrasound cleaner for 5 minutes. Than it was rinsed by a tap water and deionized water. Second round of ultrasonic cleaning was in pure acetone for another 5 minutes. Finaly, acetone was left to drip out of the sample and the sample was cleaned for 15 minutes in a plasma cleaner with the air as the cleaning gas.

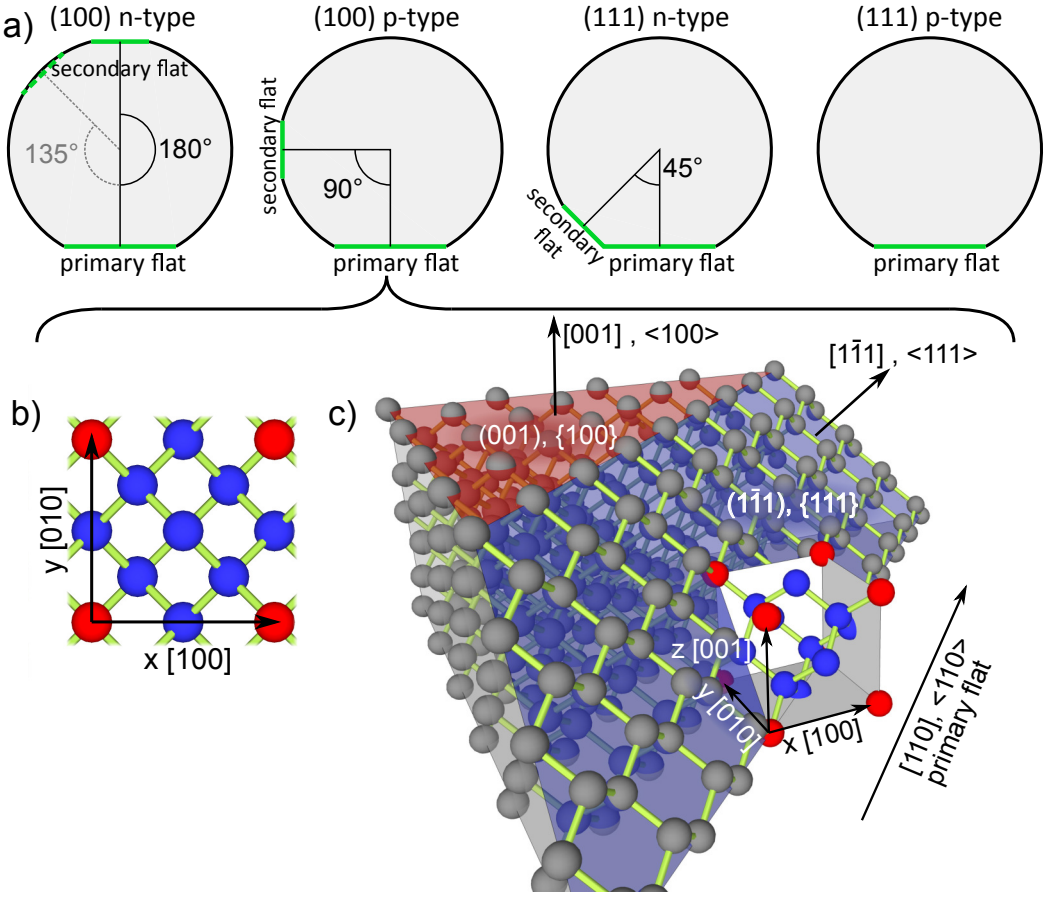


Figure 23: a) Typical marking of the Si wafer types by primary and secondary flats. Two types of the marking for the (100) n-type wafer can be found to be in use. b) The crystal structure of the (100) p-type Si in the view along the <100> direction. c) A 3D view of the primary flat wafer edge. Crystal planes and a unit cell are illustrated.

## 2.3 Characterization devices

During the experimental work, laser-modified materials were characterized by several different methods, including optical microscopy (OM), confocal laser-scanning microscopy (CLSM), scanning electron microscopy (SEM), atomic force microscopy (AFM) and $\mu$-Raman spectroscopy. These methods, by nature, provide different information about the studied sample. For better understanding of the presented results a brief overview of these methods follows for the microscopes used: Olympus BX43 (OM), Olympus OLS5000 (CLSM), Tescan Mira 3 (SEM), Horiba SmartSPM-1000 (AFM) and XploRa Plus ($\mu$-Raman). Along with these, several other microscopes including OM Olympus BX51, CLSM Olympus LEXT4000, SEMs JEOL JSM 6490LV and FEI Phenom and optical profiling microscope Zeta Instruments Zeta-20 were used while on secondment to other institutions.

The most important parameter in the microscopy is lateral, and if applicable also vertical, resolution. The best achievable resolutions for the used microscopes are summarized in the Tab. 9.

| | lateral resolution | vertical resolution |
|---|---|---|
| Optical microscope (Olympus BX43) | $\sim$ 270 nm (100x, 0.95 NA) | – |
| Confocal laser scanning microscope (Olympus OLS5000) | 120 nm (100x, 0.95 NA) | $\sim$2 nm (100x, 0.95 NA) |
| Scanning electron microscopy (Tescan Mira 3) | 1.2 nm (30 keV) | – |
| Atomic force microscopy (Horiba SmartSPM-1000) | $<$ 0.1 nm | $<$ 0.1 nm |

Table 9: An overview of the declared and estimated ($\sim$) resolutions of the used microscopes.

### 2.3.1 Optical microscopy

Optical microscopy was the most frequent investigation method due to its versatility, ease and speed of measurement. The clinical upright microscope with a top illumination for reflection observation allowed us, along the basic bright-field mode, also dark-field mode, differential interference contrast (DIC) and polarized microscopy. All of the mentioned modes provide slightly different complementary sample information. This is demonstrated in Fig. 24, on an example of the LSFL structures on silicon with a spatial period of 1 $\mu$m. Figure 24a shows a simple reflected bright-field image. It may lack contrast for topographically pronounced, but otherwise homogeneous regions.

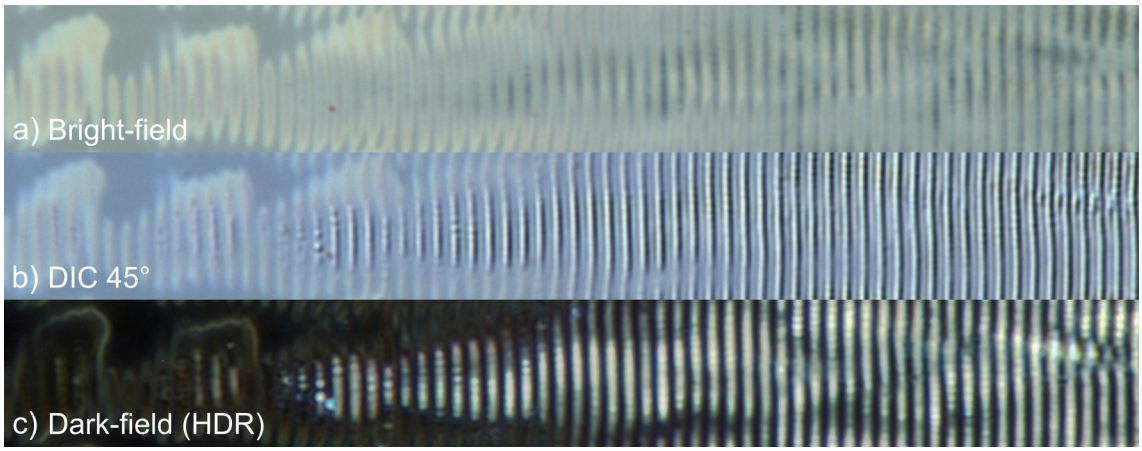


Figure 24: Comparison of selected optical microscopy observation modes visualising LSFL structures on silicon with a 1 $\mu$m spatial period. (HDR) denotes a multi-exposure *high dynamic range* image.

This is not the case in the DIC mode (Fig. 24b), which is designed to reveal small topographical variations. The DIC is a beam-shearing interference system. As illustrated in Fig. 25a, polarized illumination is split (sheared along a shear axis) by a miniscule amount by a birefringent compound Nomarski prism, which later also recombines the ordinary and extraordinary waves. Topographical variations of the sample surface introduce optical path modulation into the two waves, each probing a slightly different position on the sample. After recombination, interference and filtering by an analyzer, phase differ-

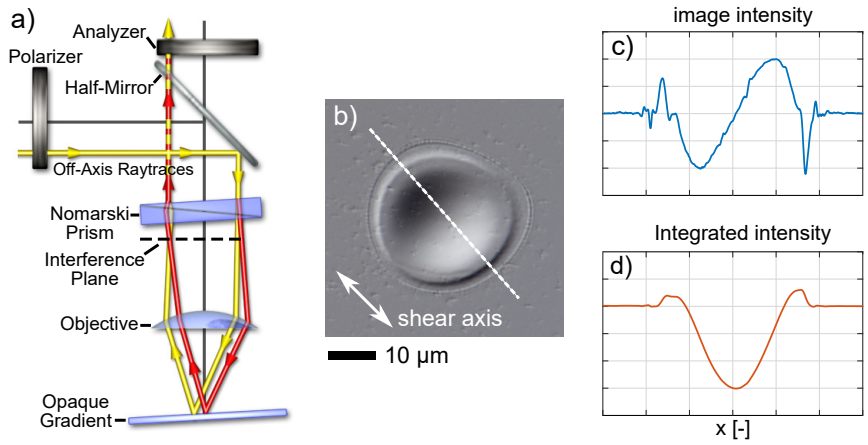


Figure 25: a) The optical pathway in reflected light DIC imaging. Reproduced from Nikon [146]. b) A DIC image of a laser crater on Si with c) a corresponding image intensity profile and d) an integrated image intensity profile along the white dashed line.

ences are converted into an amplitude modulation. When set correctly, the amplitude modulation can be both positive and negative, depending on the direction of the surface gradient. Steeper the gradient, the higher contrast is achieved. Resulting shadow-cast like image (Fig. 25b) can be therefore interpreted almost as a true three dimensional representation of the surface illuminated from a highly oblique light source. In addition, the DIC image closely corresponds to the mathematical first derivative of the optical path variation. Integrating a DIC image along a line profile (Fig. 25c from Fig. 25b), an approximate profile of the surface is retrieved (Fig. 25d). In the DIC mode, topographical gradients are visualized only along the shearing axis. By rotating the sample, surface features perpendicular to the shearing axis are emphasized.

The last examined mode is the dark-field observation (Fig. 24c). A special illumination adapter on the objective is used for a sample illumination by a hollow cone of light. The angle of this cone is large enough so that the directly reflected light from the sample is not captured by the objective. Therefore, only the scattered light is visible through the microscope. This allows to discern surfaces with different scattering parameters or with

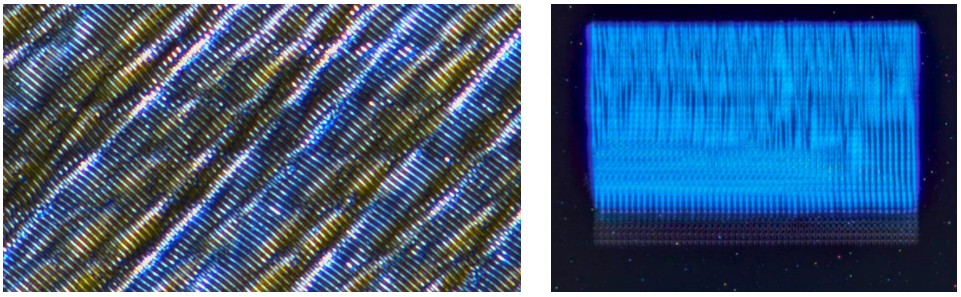

Figure 26: Optical coloration effects in OM of 1 $\mu$m periodic structures on Si. Left: DIC image of structures with two similar orientations visualized in blue and yellow ($88 \times 44\,\mu m^2$, saturation enhanced). Right: dark-field image of periodic structures visible as a blue diffraction color ($5\times$, 0.15 NA, scanned area $450 \times 250\,\mu m^2$).

topographical variations deflecting the directly reflected light towards the objective.

In addition, it is worth noting two effects observed in OM on periodic structures ($\Lambda \approx 1\,\mu$m), which are helpful in evaluation of the surface modification. Figure 26 left shows an effect in the DIC, where the orientation of the structures with respect to the shear axis also leads to coloration of the image, helping to distinguish tiny changes in the ripples orientation. This effect was observed to be stronger for lower magnifications. The other effect is exemplified in Fig. 26 right. Strong diffraction of the blue wavelengths can be observed from 1 $\mu$m periodic structures in the dark field illumination, giving information on the structure presence in a wide-field, low magnification observation (5×, 0.15 NA).

### 2.3.2 Confocal laser scanning microscopy

Confocal laser scanning microscope is a reflective type of microscope, where the sample is illuminated through a dedicated microscope objective by a focused low power laser beam at 405 nm. This beam is $x$-$y$ raster scanned over a single $z$-plane by a galvo-MEMS scanner several times per second. Reflected light is collected by the same objective, passed through a pinhole filter (a confocal system) and detected by a single channel detector (e.g. a photodiode). Several such $x$-$y$ scans are performed in successive $z$-planes in a range slightly larger than all the sample surface depth variations. After that, for each $x$-$y$ position (pixel) a fit of the image intensity as a function of the $z$-position is calculated. Amplitudes of the fitted intensity peaks yield an *intensity image*, while $z$-positions of this peaks correspond to sample surface height. Along with the confocal imaging system, the microscope typically includes a classical white-light microscopy part providing in addition a color image that is, thanks to knowledge of the height map, all in focus. However, due to a confocal-specific objective, the color image may be of lower quality than that from a dedicated optical microscope.

Properties of the confocal microscope make it a useful tool in quick and precise measurement of lateral and depth sample features, enabling for example a measurement of an ablated volume. Further, no sample preparation is needed and sample is not damaged during the measurement.

### 2.3.3 Scanning electron microscopy

A scanning electron microscope (SEM) forms an image by raster scanning an electron beam across the specimen surface. The electron beam, in the case of Mira 3, is emitted from a Schottky field emission gun. It is then accelerated by an electric potential up to 30 keV and shaped by apertures and electromagnetic coils. Another set of coils focuses and deflects the beam to accomplish the beam raster scanning. Interaction of the e-beam with the specimen causes several effects to take place, namely elastic and inelastic scattering and emission of electromagnetic radiation. During elastic scattering, electrons are deflected, without significant loss of energy. These *Back-scattered electrons* (BSE) are detected by a circular detector positioned above the sample. Since the scattering coefficient is strongly dependent on an atomic number, the BSE image provides an elemental contrast. The BSE may undergo a diffraction on the sample's crystal lattice, forming an electron backscatter diffraction pattern, which is used to analyze crystal orientations in

poly-crystalline samples. Inelastic scattering leads to creation of secondary electrons, electrons ejected from their atoms by interaction with the primary e-beam. Those *secondary electrons* (SE) close to the sample surface may be released to the microscope vacuum chamber and attracted by a positively biased grid in front of a (Everhart–Thornley) detector. This detector generates a secondary electron signal, which is the most common SEM imaging mode. During the inelastic scattering, a hole can be generated in some of the inner electronic shells after ejection of an electron. This empty electronic state may be filled by a higher energy electron, while radiating an electromagnetic wave. This includes characteristic X-rays, that are used for microscopic elemental analysis in the Energy-dispersive X-ray spectroscopy (EDS), which is demonstrated on molybdenum nanostructures on glass in Fig. 27.

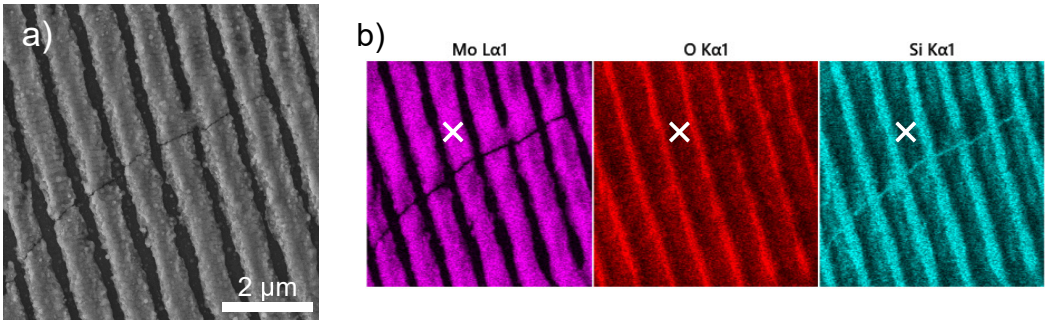


Figure 27: Energy dispersive X-ray spectroscopy (EDS, Oxford) used for elemental localization in molybdenum nano-wires on glass. a) An SEM SE image, b) corresponding elemental maps with a single position indicated by a cross.

In comparison with the previous microscopy techniques, SEM is more cumbersome in terms of additional sample preparation (cleaning, mounting, conductive layer deposition), a need for high vacuum, possible contamination of the specimen by residual gasses in the microscope chamber and damage by the electron beam. Further, high quality real-time image is not available since the acquisition of a noise-free image takes considerable time. Non-conductive or non-homogeneously conductive samples will accumulate charge during image acquisition, causing e-beam drift and image distortion. Also the microscope parameters may need to be corrected after every e-beam current or energy change. However, these drawbacks are largely compensated by two orders of magnitude better resolution than for the OM, an easily variable field of view up to a few centimeters and a large focal depth. Under specific conditions (large pressure, and/or low voltage), non-conductive uncoated samples can be imaged as well.

Resolution of the SEM is not a fixed value, but depends on the e-beam size and the interaction volume, the volume where the primary e-beam scatters within the specimen. Its size depends on electron energy, elemental composition and mass density of a specimen. With increasing interaction volume contrast of the surface features fades away and the specimen surface gains a translucent appearance.

### 2.3.4 Atomic force microscopy

Atomic force microscopy (AFM) is a scanning probe microscopy technique capable of achieving sub-nanometer resolution. A sharp scanning tip (typically silicon or silicon nitride) with a tip radius of several nm is attached at the end of a flexible cantilever. In a close proximity of the sample surface, variety of forces start to interact with the tip, e.g. attractive Van der Waals force due to charge-induced polarization or near-contact repulsive force of electron orbitals due to exchange interaction. These cause deflection of the cantilever and deflection of a laser beam, which is reflected on its back side. The laser beam is registered by a position sensitive (quadrant) detector. Precise *x*-*y*-*z* positioning and scanning is accomplished by piezo scanners, allowing a $\sim 100 \times 100 \times 15\,\mu\mathrm{m}^3$ scan range, while classical stepper motor *x*-*y*-*z* stages are used for rough sample positioning.

The scanning tip requires a specific attention as its properties dictate the interaction with the sample and type of information being collected. A resulting image is a convolution of the tip shape with the real surface map, therefore for an artifact free measurement a sharp (small tip radius) and high aspect ratio tip is desirable.

Depending on the application, AFM can be operated in numerous imaging regimes, that can be generally divided into contact and non-contact modes. In the *contact mode*, as the name says, the tip is swiped along the surface typically with a constant applied force (cantilever is bent), or less often at a constant height of the scanner. In this regime an atomic resolution can be obtained, however the sample surface can be substantially damaged. In contrast, in the *non-contact mode* the tip is oscillated above the surface at or near cantilever resonant frequency. Oscillating tip interacts with long range forces from the surface (e.g. Van der Waals, electrostatic), that are affecting its resonant frequency and oscillation amplitude. Surface topography is sensed by adjusting the average tip height in order to maintain constant oscillation amplitude or frequency in a closed feedback loop while raster-scanning the sample. The distance of the tip prevents both the sample and the tip from damage at the cost of lower resolution. In practice, a hybrid *tapping mode* is the most frequently used AFM regime. The cantilever is again oscillated, however, it also comes into contact with the sample. This prevents the tip from sticking to the surface as in the contact mode, while allowing for brief close contacts for higher resolution than in non-contact mode. Sample damage is reduced compared to the contact mode. In tapping mode, phase lag between the cantilever driving element and cantilever oscillation can be recorded as well, simultaneously with the topography information. The resulting *phase* signal contains information about energy dissipated by the cantilever in each oscillation cycle. Amount of the dissipated energy is dependent on material elasticity and adhesion properties. The phase image therefore also provides a material contrast.

AFM, in a comparison to the previous microscopy methods has the highest spatial resolution. The sample does not need special preparation neither vacuum is needed and the measurement is three-dimensional. On the other hand the maximum scan volume is strongly limited to (in our case) $\sim 100 \times 100 \times 15\,\mu\mathrm{m}^3$, acquisition of an image takes from several minutes to over an hour and real time view is available only through low resolution optical navigation. Also the piezoelectric scanners are prone to nonlinearity, hysteresis and thermal drift. Therefore, the obtained data require additional post-processing, making the measurements less suitable for accurate absolute distance/height measurements.

In the measurements reported in this work mainly conical silicon Nu Nano Scout 150 RAI AFM tips were used with typical parameters of 5 nm tip radius, 7 $\mu$m tip height, 25° cone angle and 150 kHz resonance frequency.

### 2.3.5 $\mu$-Raman spectroscopy

The method of Raman spectroscopy was developed to sense vibrational modes of molecules, however may work as well with sensing of optical phonons in solid state physics, where it is applied in determination of sample material constituents and crystallinity. The Raman spectroscopy is based on inelastic scattering from optical phonons. It is simillar to the Brillouin scattering, where the photon interact with an acoustic phonon instead. In both cases there are two possible interaction scenarios: Stokes scattering, when a phonon is emitted and the incident photon loses energy (red shift) and an anti-Stokes scattering corresponding to an opposite process. The anti-Stokes scattering requires phonons to be present in the material before the interaction, while Stokes scattering does not. By analysing a spectrum of the scattered light, phonon frequencies (near the Brillouin zone center) can be deduced. Positions and strengths of the spectral peaks are used to determine the material types and their structural state. Raman spectroscopy is complimentary with the infrared spectroscopy, which provides similar information, however, as a rule of mutual exclusion states, the optical phonon modes in centrosymmetric crystals are either Raman or IR active.

Raman scattering is a weak process with small scattering rates. Also the frequency shift is small. Therefore, Raman spectrometers use IR-VIS-UV lasers as a high intensity monochromatic light source along with high sensitivity cooled semiconductor detectors and a notch filter to suppress the elastically scattered light.

The $\mu$-Raman spectrometer (Horiba Scientific, XploRa Plus, microscope BX41, software LabSpec6), i.e. a spectrometer where a microscope objective is used to both focus the excitation laser and collect the scattered light, was used in the experimental part to analyze silicon surface modification. Fig. 28a) shows Raman spectra of crystalline (c-Si) and amorphous (a-Si) silicon, and of fused silica (a-$SiO_2$). A characteristic peak at 520.5 $cm^{-1}$ can be seen in the silicon spectra. The amorphous silicon can be distinguished by presence of a broad band peak around 473 $cm^{-1}$ [147]. When the silicon surface is irradiated by high intensity laser pulses in air, a few nanometer oxide surface layer may form. Unfortunately, it is not possible to distinguish such layer with the available spectrometer, due to: a) the signal from the $SiO_2$ is by two orders of magnitude less intense than the signal from the Si; b) the penetration depth of the excitation laser light (532 nm) is $\sim 3\,\mu$m and most of the signal comes from the underlying Si. To reduce the penetration depth, deep-UV excitation may be used.

In spectroscopy, a unit of reciprocal length is frequently found, that may be unfamiliar to experts in other topics of physics. To help with this inconvenience, basic conversion equations follow. A laser wavelength $\lambda$ [nm] in the reciprocal units is expressed as:

$$\lambda_{\mathrm{rec}} = \frac{10^7}{\lambda}[\mathrm{cm}^{-1}]. \tag{29}$$

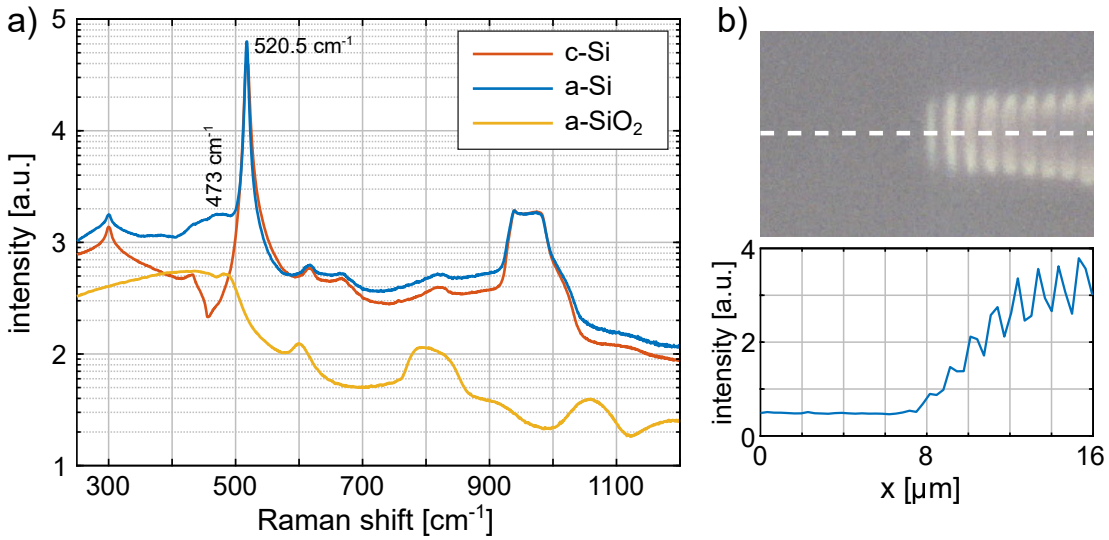


Figure 28: a) Raman spectra of crystalline silicon (c-Si), a layer of amorphous silicon (a-Si) on c-Si, and of fused silica (a-$SiO_2$, amplified), measured with 532 nm excitation. b) Amorphous Si LIPSS on monocrystalline Si surface (Section 3.3.2). Corresponding Raman signal along the white dashed line at the band around 473 $cm^{-1}$ clearly indicates periodic amorphization.

To convert a unit of the Raman shift $\Delta\omega$ [$cm^{-1}$] to [nm]

$$\Delta\lambda = \frac{10^7 \Delta\omega}{\lambda_{\text{rec}}^2}[\text{nm}] \tag{30}$$

for an excitation laser wavelength $\lambda_{\text{rec}}$ [$cm^{-1}$]. And a general expression for the photon energy is

$$\varepsilon = \frac{c_0 h}{e_0 \lambda 10^{-9}} = \frac{1240}{\lambda}[\text{eV}]\,, \tag{31}$$

where $c_0$ denotes a speed of the light in vacuum, $h$ Planck constant and $e_0$ an elementary charge.

# 3 Results and discussion: LIPSS – scanning with a Gaussian beam

During the course of doctoral studies, several types of experiments were conducted on the topic of LIPSS formation and material surface modification [65, 90, 111, 148], damage threshold measurements [129, 133] and volumetric modification by using various methods and laser parameters. The major part of the experimental results is related to the study of formation of the LIPSS structures on large areas of silicon and fused silica surface in a view of reaching high regularity of the structures. These are followed by attempts on laser modifications by shaped beams and damage threshold measurement of silicon in the mid-IR region.

This section is focused on material surface structuring by a spatially Gaussian laser beam. First, prerequisites for controlled surface modification are discussed. The second part of the section reports on experimental results obtained from large-area periodic surface structuring of silicon and fused silica.

## 3.1 Laser-induced material damage threshold

Successful realization of surface structuring by LIPSS depends on knowledge of several parameters, some of which are inherent to the material properties, while some are inherent to the LIPSS in general. Prior to starting attempts to produce a structured surface, at least material laser damage threshold, for given laser parameters, should be known. Along with this, we should ideally also know how the material modification behaves at a variable pulse number. These two aspects allow us to estimate the laser power and pulse overlaps for the scanning. Further, we may need to account for the sample orientation (due to polarization dependence of the damage threshold) and orientation of the laser scanning direction with respect to the laser polarization (due to structural feedback from the LIPSS). The following discuss the above mentioned prerequisites in more detail.

### 3.1.1 Si and $SiO_2$ $N$-on-1 damage threshold

The laser-induced material damage threshold is a major parameter that determines the range of laser power / pulse energy / fluence, where the LIPSS structuring can be successfully conducted. The second most important parameter for large area structuring is determination of the pulse spacing. It can be roughly estimated by observing $N$-on-1 pulse damages. Figure 29 demonstrates such damages on silicon for 1030 nm, $\omega_0 = 23$ $\mu$m, 270 fs, $f_{\mathrm{rep}} \sim 2$ Hz. By increasing the fluence and number of pulses $N$, LIPSS will be eventually produced. This typically happens in the parametric space at the border between slight modification and ablation. As surface corrugation by LIPSS creates a positive feedback in laser energy coupling into the material, this transition is rather sharp. In this figure we can also see the damage threshold dependence on the number of pulses from the size of the damage spots, especially in the bottom row, as was described in the Section 1.2.1.

Additionally, Fig. 30 shows an evaluation of the $N$-on-1 irradiation of silicon (Fig. 29) and $SiO_2$. It clearly shows a decrease of the measured damage threshold as a function of

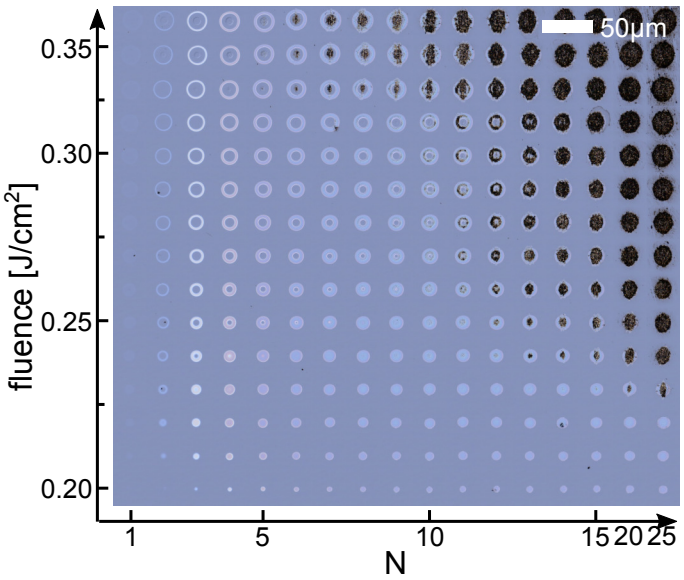


Figure 29: Collage of OM-DIC images showing a typical $N$-on-1 pulse damage threshold experiment on silicon.

the increasing number of pulses. Respective accumulation factors are $s_{\mathrm{Si}} = 0.94$ and $s_{\mathrm{SiO_2}} = 0.76$. For silicon, the value is close to what is reported in literature ($s = 0.87$ [149]). In the case of $SiO_2$, accumulation dependency by eq. 6 does not fit very well. Either the incubation effects are more complex than a simple exponential decay [18, 150, 151], or the observed deviations are caused by a specific interaction of the laser with glass, where the damage crater has a tendency to deepen and create rugged edges with chipping material, rather than smoothly extending in its width. Anyway, the 54 % decrease of the threshold fluence for $N = 20$ is comparable within the experimental error (at this pulse number) with a reported 70 % decrease for similar parameters (100 fs, 800 nm) [18].

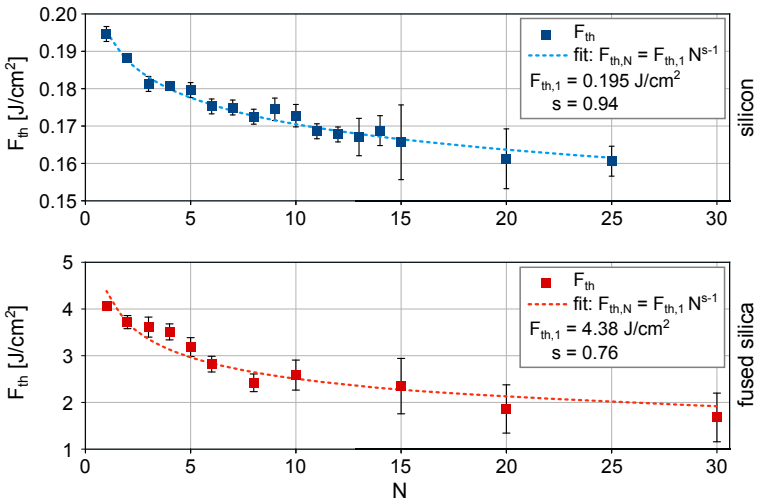


Figure 30: An accumulation effect in the damage threshold of silicon and fused silica when irradiated by $N$ pulses.

In the $N$-on-1 irradiation (Fig. 29) laser spots are forming ring structures for most of the irradiations with fluences larger than $\sim 0.25$ J/cm$^2$. These are understood [50] as a result of silicon melting followed by recrystallization in the central part of the irradiation, while due to low melt depth and high cooling rate in the surrounding area, the melt solidifies here in an amorphous pale annulus. Figure 31 shows this feature in detail for irradiation of silicon by $N = 10$ pulses. For curiosity reason, pulse number dependency of the fluence threshold for occurrence of the central hole is evaluated by the $D^2$ vs $\ln(E)$ method (Section 2.1.3.1), where $D$ denotes a diameter of the internal hole. Empirical fit functions (modified incubation relation - blue and a parabola - red) are proposed in the graph.

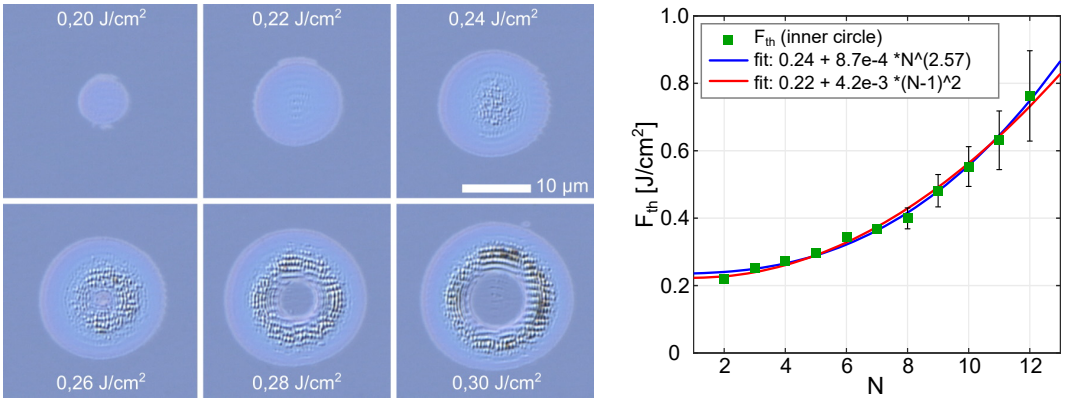


Figure 31: Evolution of the 10-pulse damage spots on Si for increasing fluence. The graph shows laser fluence at the inner border of the annulus.

### 3.1.2 Polarization dependence of the damage threshold

In case the irradiated material is crystalline, whether metallic [152] or with a bandgap [153–156], its damage threshold (DT) can be dependent on the crystal orientation and orientation of the incident laser polarization. For bandgap materials, this is due to modulation of the ionization rate along different crystal orientations, which is attributed to anisotropy of the effective electron mass in a mixed regime between multiphoton and tunneling ionization [154, 156].

Although this effect is known, it is often disregarded and it is interesting to investigate its magnitude in the actual material (silicon, (100) oriented, p-doped), that was used for the LIPSS scanning experiments. For this, simple, but precisely aligned laser setups were built, where $\sim 2 \times 2$ cm$^2$ silicon samples were placed on a $x$-$y$-rotation stage with carefully removed tilts. The laser beam was incident perpendicularly onto the sample in a top-down vertical direction.

In total, three series of measurements were conducted, each for a different pulse duration of 37, 270 and 1900 fs. Focusing conditions were adjusted so that the $\omega_0$ was kept constant. The damage evolution for $\tau = 37$ fs is visually demonstrated in Fig. 32. DIC images of the damage threshold measurement series are shown, where each row corresponds to a different orientation of the laser polarization with respect to the crystal axes. A clear 90° period is visible in the sample modification variations.

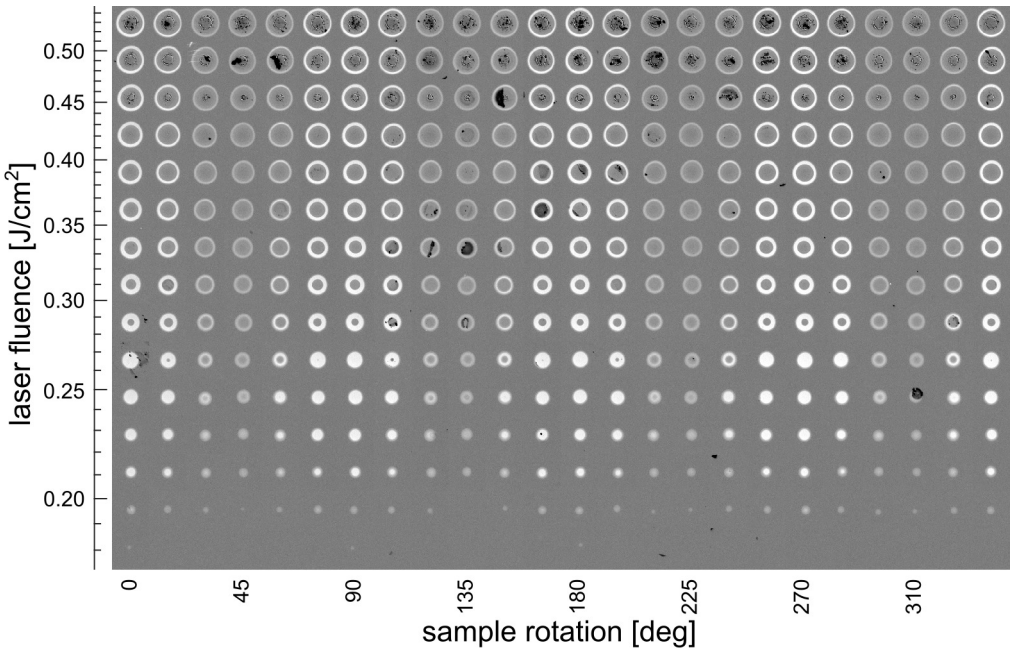


Figure 32: A mosaic of optical microscopy images of raw damage data for $\lambda = 800$ nm, $\tau = 37$ fs. Contrast is globally enhanced. At 0° orientation, polarization is parallel with $\langle 110 \rangle$. The sample was rotated under a fixed linear polarization.

During the experiment, laser power was set and measured manually before each partial irradiation consisting of 24 single pulses of the same energy. The rotation stage was rotated by 15° after every pulse, creating a circle of 24 points. At the 0° angle, polarization is aligned with $\langle 110 \rangle$ crystal direction. Then the rotation stage was offset sideways to allow for another irradiation series at an increased power. Every experiment consisted of 20 such steps, four of which were alignment marks.

Surface damage threshold was evaluated for every angle and every pulse duration by the $D^2$ vs $\ln(E)$ method. A significant amount of data and very low contrast between pristine and amorphized silicon in the OM images were causing large measurement errors in manual area evaluation. Therefore, I developed a semi-automated algorithm in Matlab (see Appendix F), which significantly improved the precision of the results and repeatability of the image analysis.

The obtained dependency of the DT on the sample orientation is demonstrated in

| **pulse duration** [fs] | **37** | **270** | **1900** |
|---|---|---|---|
| wavelength [nm] | 800 | 1030 | 1030 |
| $\omega_0$ [$\mu$m] | 20.0 | 20.5 | 20.1 |
| $F_{\mathrm{th,average}}$ [J/cm$^2$] | 0.184 | 0.201 | 0.292 |
| $\Delta F_{\mathrm{th,p-p}}$ [J/cm$^2$] | 0.017 | 0.015 | 0.015 |
| $\Delta F_{\mathrm{th,p-p}}$ [%] | 9.3 % | 7.2 % | 5.0 % |

Table 10: Experimental parameters and results obtained for damage threshold dependency of the (100) Si on orientation of incident linearly-polarized laser pulses.

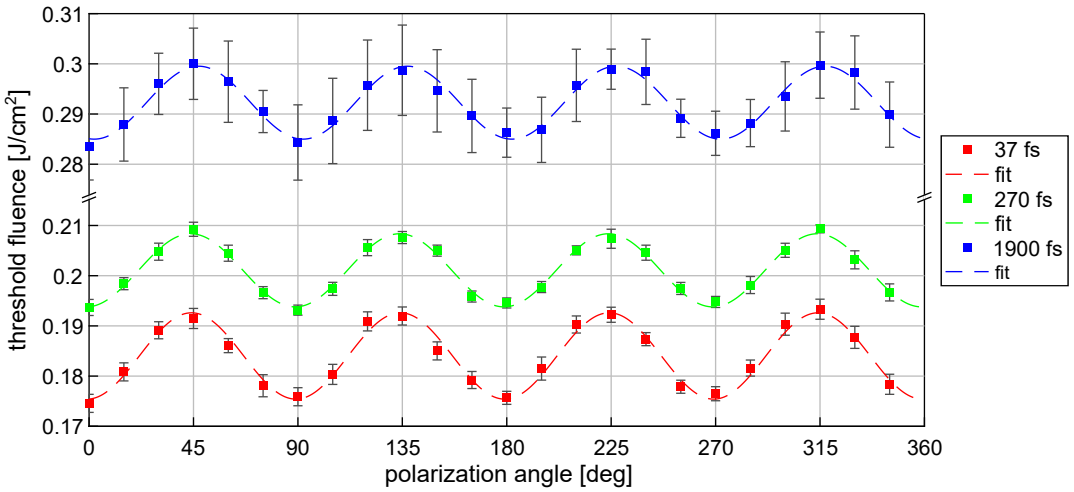


Figure 33: Influence of the laser linear polarization orientation in the (100) Si crystal plane on the surface damage threshold. Data for three series of irradiation (see text) are reported. The dashed lines stand for a least-squares cosine function fits. At 0° orientation, polarization is parallel with ⟨110⟩. Note the gap in the $y$-axis.

Fig. 33 for all three pulse duration. The above mentioned 90° modulation period is clearly visible. All the data can be fitted by cosine functions within the measurement error. Extracted fit values together with experimental parameters are summarized in the Tab. 10. Phase offsets of the fit functions are -1°, 2° and -1° for the 37, 270 and 1900 fs respectively. The variations in the offset corresponds well to the precision in the sample alignment method, by observing scattering of a focused laser on cleaved ⟨110⟩ edges and aligning them to the $x$-$y$ stage axes. Larger errors of the picosecond DT measurement arise from a very low contrast between the modified and pristine surface in the microscope image data (see Appendix F - Fig. 81). However, thanks to a relatively large number of evaluation points in the procedure, the DT values are actually still precise.

The orientation dependency can be explained by multiphoton ionization, which is dependent on the crystal orientation. This was verified also by numerical simulations based on time dependent density functional theory made by Dr. T.J.-Y. Derrien. When the polarization is in a plane of the Si bonds, the ionization rate is higher and, therefore, a smaller damage threshold is observed. Along with multiphoton ionization, impact ionization is also present. Since the impact ionization is related mainly to the kinetic energy of the heated electrons in the conduction band, it plays an important role in the damage onset for longer pulses. It is also less dependent on the polarization of the laser. As a consequence, the effect of the polarization orientation in the DT becomes less pronounced for longer laser pulses.

The observed DT variations mean that orientation of the silicon sample with respect to the polarization plays a non-negligible role in laser processing. In particular, for our mostly used irradiation regime, using 1030 nm and 270 fs pulse duration, one can get a DT change of up to 7.2 % when the sample is not oriented properly.

These results are being prepared for a publication.

### 3.1.3 Two-pulse bi-color irradiation

Traditionally, monochromatic laser beams are used for material processing. However, for specific conditions, several studies reported on advantages of dual-wavelength two-pulse irradiation against the single pulse or monochromatic double-pulse irradiation. In particular, the advantage is enhancement of the laser ablation yield and smoothness of processed fused silica [157], silicon [158] and steel [159], improvement of microfabrication of optical structures in fused silica and GaN [160], additional control over LIPSS orientation and period [161, 162], and more. The interaction mechanism itself is believed to be based on enhanced photoionization by shorter wavelengths while longer wavelengths are absorbed more efficiently by the inverse bremsstrahlung process. Therefore, a combination of the two wavelengths (shorter first, longer second) in a correct ratio may result in a more efficient energy absorption. On the other hand, combinations of laser and material parameters exist, where it was shown that dual-wavelength irradiation is energetically disadvantageous against simpler single-wavelength processing [163].

We investigated this effect experimentally on silicon, for our irradiation condition. The (100) Si sample was irradiated in a normal incidence by fundamental and second harmonic pulses of the Pharos laser in a pump-pump collinear configuration for pulse duration of ∼250 fs. Focusing was done by a parabolic mirror to have the same focal distance for both wavelengths. Spot size of both beams on the sample was 59 $\mu$m. In this configuration, the effect of the pulse delay (-400 .. +400 ps) and pulse energy ratio (0 .. 1) on a damage threshold and volumetric ablation efficiency was investigated.

Figure 34 shows the dependency of the surface damage and ablation area size on the delay between the two pulses. Here, both pulses have equal energy and total peak fluence for the zero time delay is 0.67 J/cm$^2$ (2.3× the ablation threshold for 515 nm). The areas are normalized to the modification size observable for a single 515 nm pulse with the same total energy. Modification size is larger for a single 515 nm pulse as the observed damage threshold for 515 nm (0.13 J/cm$^2$) is smaller than the one for 1030 nm (0.23 J/cm$^2$). A strongly asymmetric behavior is observed. Both damage and ablation sizes are larger for negative pulse delays where the 515 nm pulse is leading. Size of the damage area for 0 ps delay is ∼15 % larger than for a 515 nm pulse alone. Increased damaged area for 0 ps delay is observed also for other pulse energy ratios where 515 nm is at least 20 % and peaks around 45 %. Enhanced dual-wavelength modification, in comparison to monochromatic irradiation, is observed only in a range -1 ps to 0 ps delay, which matches with results reported on fused silica [163]. Within the ablation sizes, a second peak exists around -100 ps. Reasons for this peak are not understood.

Similarly, for fluence of 0.44 J/cm$^2$ (1.5× the ablation threshold), dependency of the ablated volume on temporal delay shows a peak at 0 ps at ∼ 7× the amount ablated just with 515 nm, but this time stays above 3× enhancement up to -300 ps. This behavior completely changes for larger fluences of more than 5× the ablation threshold, where no such enhancement of ablated volume is observed. A significant increase of the ablated volume of silicon by dual-wavelength irradiation is possible, but is limited to low fluences just above the ablation threshold.

These results are in an agreement with a theoretical concept in which the first short wavelength pulse generates free electrons by photoionization, which allow for efficient

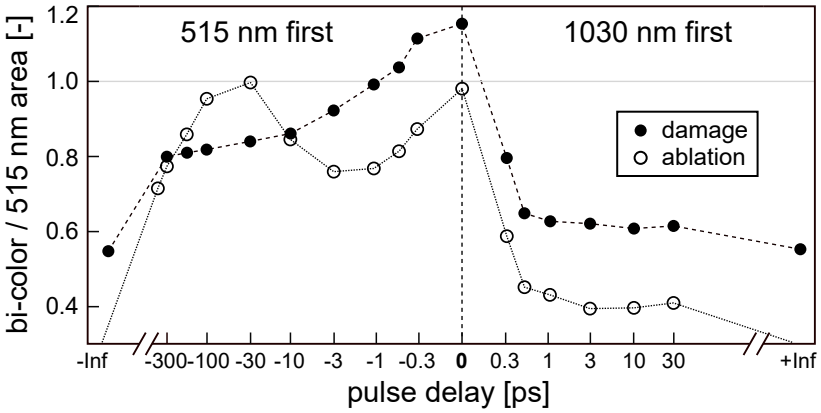


Figure 34: Size of damaged and ablated surface area in a double-pulse dual-wavelength irradiation with 1030 and 515 nm pulses of equal energy 4.55 $\mu$J. Areas are normalized to a modification area by a single 515 nm pulse of double energy. Lines are guides for an eye.

absorption of the second longer-wavelength pulse. In an opposite scenario when the NIR pulse interacts first, laser interaction is weak and lower electron density is generated. Subsequent 515 nm pulse increases excitation by photoionization, but its absorption by solid plasma is not efficient and overall absorbed energy is lower. This theory can be applied to both semiconductors and dielectrics.

Additionally, the damage threshold of the dual-wavelength irradiation, for equal pulse energies, was determined to be $\sim$0.1 J/cm$^2$. That means a decrease of the damage threshold even below the one for 515 nm pulses alone.

These results are being prepared for a publication.

### 3.1.4 Si-SiO$_2$ interface LIPSS

Several applications involve processing of materials with a protective or masking surface layer. Even a silicon wafer, when stored under ambient conditions, will develop a few nm thick native oxide layer on its surface. Such a thin layer does not affect interaction between the silicon and laser, which is not the case for thick artificially grown oxide layers. Several hundreds of nm thick layer will alter the initial spot size and damage threshold estimation, causing processing with incorrect parameters. In the publication [133], we investigated such an effect on a silicon wafer with a native and artificial ($\sim$300 nm) oxide layer, upon irradiation by 1030 nm, 260 fs, $\omega_0$ = 13.2 $\mu$m laser pulses. It was observed that the artificial oxide layer increases both the damage threshold (from 0.226 to 0.267 J/cm$^2$, $\Delta$18 %) and the spot size measured (from 13.17 to 13.65 $\mu$m, $\Delta$4 %). Therefore, it is suggested not to use materials with transparent coating for spot size evaluation by the $D^2$ vs ln($E$) method. We note that the reported damage threshold fluence of the silicon with the native oxide layer in the manuscript does not match the lower fluences around 0.2 J/cm$^2$ reported here earlier, e.g. in Fig. 33. As the silicon wafers used here and in the manuscript were different, we believe the main reason for the discrepancy is due to a different doping concentration.

Further, we demonstrate that for a certain range of laser fluence the SiO$_2$ layer stays continuous, while the underlying silicon is already being modified/ablated. Figure 35

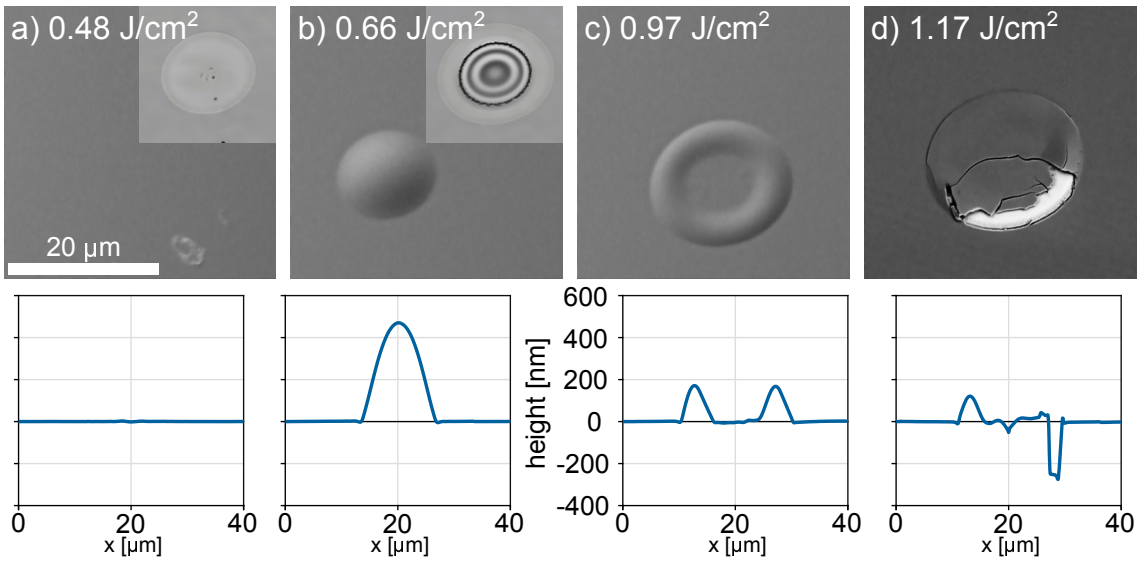


Figure 35: SEM micrographs of silicon with an artificial $SiO_2$ layer and corresponding AFM surface topographical profiles ($\omega_0 = 13.2\,\mu$m, $\lambda = 1030$ nm, $\tau = 260$ fs and increasing fluence). CLSM image insets show silicon damage under the oxide layer. Modified from [133].

demonstrates this for four fluences on SEM and CLSM images together with AFM surface profiles. This type of modification was further used in our publication [90], where on a similar silicon sample with an artificial oxide layer, we fabricated LIPSS on the silicon under the $SiO_2$ covering layer. Two particular structure types were produced: a) shallow highly-regular LIPSS transferring the $\sim$ 5–10 nm surface relief modulation to the oxide layer (1030 nm, 300 fs, 200 kHz, 0.221 J/cm$^2$, $\Psi_{x,y} = 75$ %) and b) smooth bumps erected above the initial oxide surface to the height of several dozens of nanometers positioned in the centers of the irradiation spots (1064 nm, 10 ps, 100 kHz, 1.68 J/cm$^2$, $\Psi_{x,y} = 51$ %). After irradiation, both structures were covered by a single layer CVD grown graphene, which mimicked the surface topography. A periodic modulation of the graphene charge doping with a period of the LIPSS was observed for the latter pattern. This is most probably due to the fact that the p–doped silicon was deposited periodically on the bottom of the oxide film. Such modulation affects chemical properties, which was used to periodically modulate the functionalization density of the graphene monolayer. Periodic functionalization was verified by $\mu$-Raman surface mapping of the D and G band intensities. These findings allow to design anisotropic, periodically modified surfaces for advanced applications in (opto)electronics, smart coatings or cell biology experiments.

### 3.1.5 Modification of polymers

Discussion on the damage thresholds will be closed by measurements on polymers, where laser interaction with Kapton polyimide, polystyrene and PMMA was investigated. Laser interaction with polymers is rather complex and includes chemical reactions, thermal, photophysical and mechanical processes. Depending on the specific irradiation conditions, one of the processes may dominate. Typically, various polymers were processed by UV wavelengths, where linear absorption takes place. Nowadays, ultra-fast NIR laser

systems with frequency upconversion into UV can be used for this purpose. However, technologically simpler direct irradiation with NIR wavelengths is also capable of high quality polymer processing.

Results on the laser ablation of Kapton were summarized in a publication [129]. Here, we provide a direct comparison between irradiation by femtosecond (fs) and picosecond (ps) pulses in terms of damage threshold (0.66 vs 2.3 J/cm$^2$ respectively) and surface quality of the ablation craters. A large difference in the damage thresholds and damage morphology indicate different ablation mechanisms in the two regimes. Accurate, smooth and practically rimless ablation craters with little redeposited material were observed for fs pulses. Craters produced by ps pulses show ∼500 nm high rims and some redeposited material inside and outside of the craters. In the fs regime, elongation of the craters in a direction of laser polarization was clearly visible. This effect was attributed to an interaction of the laser pulse with solid-state plasma generated by a leading edge of the pulse [164]. Such elongation was not observed in the ps regime, which indicates that this effect is dependent on intensity rather than on fluence or that other mechanisms in the ps regime heal this effect.

The second investigated polymer was a general purpose polystyrene (Eppendorf) commonly used for fabrication of lab-ware like Petri dishes, test tubes, etc.

Surface of the 1 mm thick polystyrene sample was treated by UV (258 nm), VIS (515 nm) and NIR (1030 nm) pulses in femtosecond (250 fs) and picosecond (6 ps) range. In order to maintain similar beam spot size on the surface, three different lenses with focal lengths of 150, 300 and 600 mm were used. Table 11 summarizes results on the ablation threshold fluence. This value is strongly dependent on both wavelength as well as pulse duration. The lowest threshold was measured for 258 nm. At this wavelength, the sample strongly absorbs light and linear absorption (LA) is the dominating process. The other two wavelengths are below the energy bandgap and, therefore, only nonlinear processes (MPI - multiphoton ionization, TI - tunneling ionization) are present. In order to determine which nonlinear process is present, the Keldysh parameter $\gamma$ was estimated.

The Keldysh parameter writes as

$$\gamma = \frac{\omega}{e}\left(\frac{m_e^* c_0 n \varepsilon_0 E_g}{I}\right)^{1/2}, \tag{32}$$

where $\omega$ stands for angular frequency, $m_e^{*2}$ effective electron mass, $c_0$ the speed of light, $e$ the elementary charge, $\varepsilon_0$ the vacuum permittivity, $n$ refractive index, $E_g$ an energy bandgap of the material and $I = F/\tau\,[\mathrm{W/m^2}]$ is the peak intensity of the laser radiation. Based on the Keldysh theory, the $\gamma$ parameter reaches values $\gamma \ll 1$ in the case of dominant tunneling ionization and values $\gamma \gg 1$ for multiphoton absorption. The input parameters $E_g = 4.02$ eV, $n_{1030}$=1.562, $n_{515}$=1.588 and $n_{258}$=1.779 were derived by spectroscopic ellipsometry by other team members.

Further, topography of the ablation spots was investigated. Figure 36 demonstrates different topographies of the ablation craters for combinations of wavelengths and pulse duration, in all cases for twice the ablation threshold fluence. Ablation craters are well-defined, except for 1030 nm ps irradiation, where irregular material extrusions appear. The well defined craters exhibit rims of resolidified material, which height is increasing with increasing pulse energy. Crater elongation along the polarization direction of the

| **Wavelength** [nm] | $\tau$ [fs] | $\mathbf{F}_{\mathrm{th,a}}$ [J/cm$^2$] | **Keldysh parameter** $\gamma$ | **Process** |
|---|---|---|---|---|
| 1030 | 250 | 1.95 | 1.61 | MPI/TI |
| 515 | 250 | 0.85 | 4.92 | MPI |
| 258 | 250 | 0.28 | 18.1 | LA |
| 1030 | 6000 | 7.73 | 3.99 | MPI |
| 515 | 6000 | 2.14 | 15.3 | MPI |

Table 11: Summary of the polystyrene ablation thresholds and processes involved in the ablation.

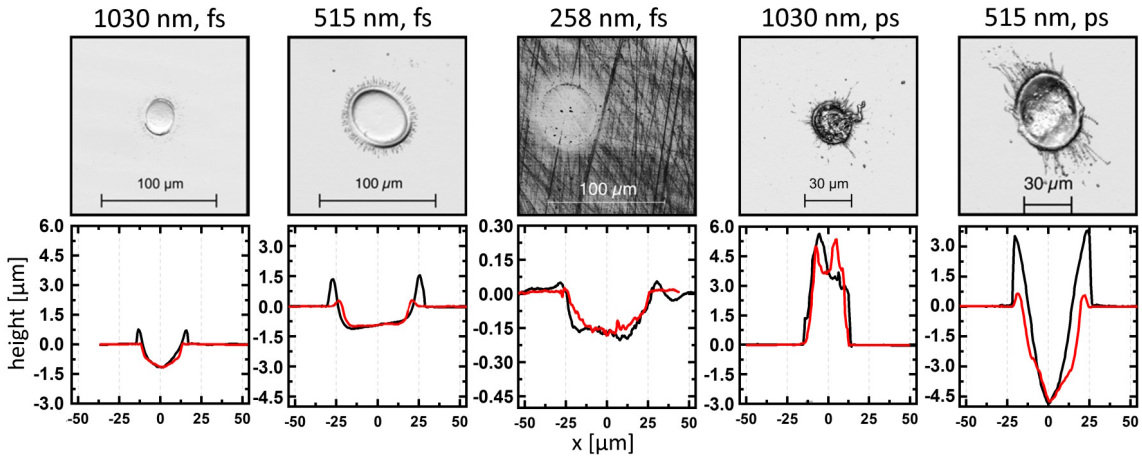


Figure 36: CLSM polystyrene ablation craters for various wavelengths and two pulse duration created at two times the ablation threshold fluence (individual for every wavelength – pulse duration pair). Topographical profiles measured along polarization (black) and perpendicular to it (red) are shown.

linearly polarized laser pulses, as well as asymmetry of the crater rims are present, similarly as in the case of the above discussed Kapton irradiation. It can be concluded that ps irradiation of polystyrene, in particular in NIR wavelengths, does not provide practical results for controlled processing. Either uncontrollable subsurface boiling and material extrusion or jets of resolidified materials are present. The highest control of the ablation results from the UV irradiation, where smooth craters with negligible rims and redeposited material were obtained. However, fs ablation with 1030 and 515 nm generated also well defined craters. Only the asymmetric crater rims are present and it is application dependent if this poses a problem or not. The data obtained on the DT of polystyrene are being prepared for a publication.

## 3.2 Polarization orientation vs scanning direction

Additionally to the orientation of the laser polarization with respect to the sample crystal axes, orientation of the linear polarization with respect to the laser scanning direction is another parameter of the large-area LIPSS scanning. This dependency originates from the spatially anisotropic scattering of the incident pulse on already existing surface structures. Figure 37 demonstrates such an effect on LIPSS scanning of silicon with 1030 nm, 270 fs, $F_{\mathrm{pk}} = 0.244$ J/cm$^2$ and $\Psi_x = \Psi_y = 85$ % overlaps, for square and hexagonal spatial pulse

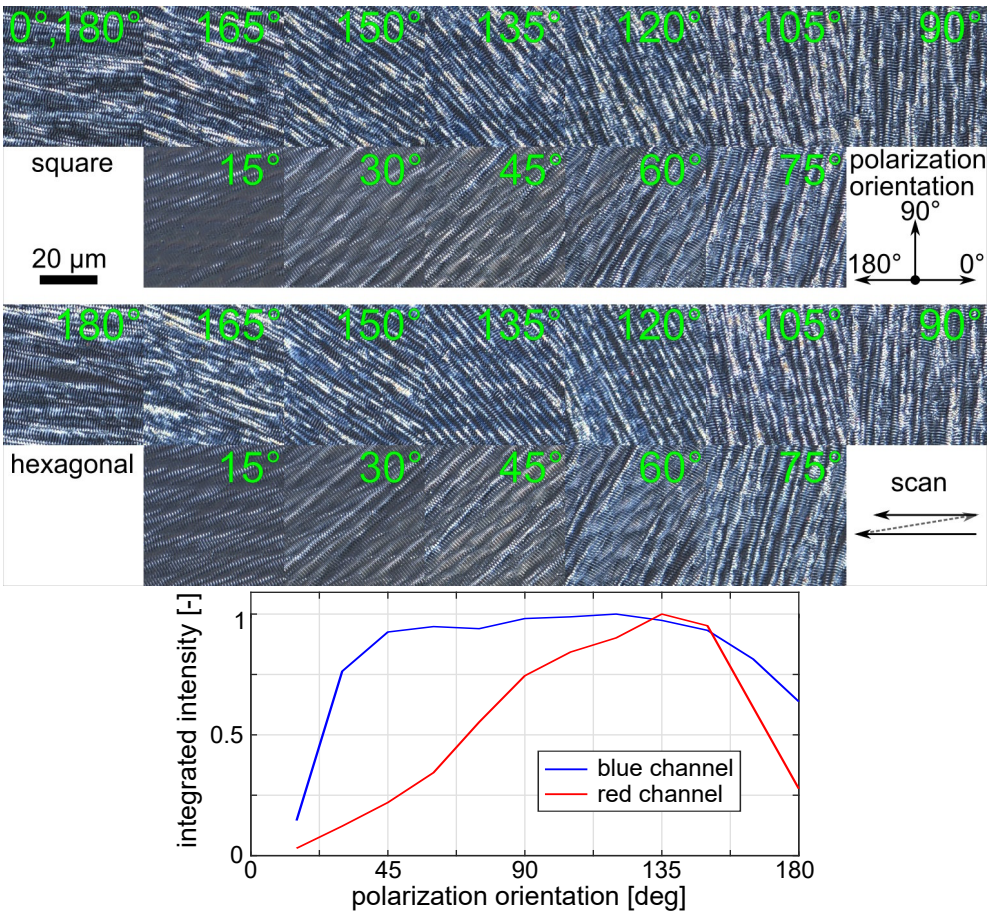


Figure 37: Dependency of the LIPSS scanning on silicon on the mutual orientation of the scanning direction and the laser polarization direction for square and hexagonal spatial pulse arrangement. Green numbers in the DIC optical micrographs indicate the polarization angle. The graph shows normalized integrated intensity of blue and red color channels from dark field optical micrographs corresponding to diffraction and scattering in the same experiment.

arrangement. Strong variation of the structure quality with respect to the polarization orientation is evident in the structures themselves (top, OM DIC) and in their efficiency to diffract and scatter light (bottom).

One can speculate that for the particular given scanning schema (of single direction scanning), the more pronounced LIPSS for 180° – 90° orientations are due to better forward (with respect to the scanning direction) scattering and, therefore, better forward coherent extension of the LIPSS. On the contrary, for 90° – 15° the existing LIPSS scatter backwards (in the direction towards the already processed area), and every new laser pulse irradiates an area with less adjacent periodic modification. This results in less energy coupling into the surface, resulting in less surface modification, resulting in even less energy coupling for the next pulse. I.e. the positive feedback of the modified surface is less effective.

Spatial pulse arrangement plays a role in homogeneity of the accumulated fluence dose on the sample and in theory could affect (see Section 3.4.1) resulting surface structures. However, for the irradiation conditions in Fig. 37 and relatively large overlaps in partic-

ular, only a little difference is observed that the hexagonal arrangement performs slightly better for $180° \pm 15°$.

Variation of the structure capability to diffract and scatter light is depicted in the graph in Fig. 37. Diffraction efficiency is derived from dark field microscopy images by integrating the blue color channel of the color image. Amount of scattering, which is spectrally broadband, is similarly derived from the red channel, to avoid overlap with the diffraction. In both cases the data are an average of both spatial arrangements. Due to the acquisition method, the blue channel data quickly reach saturation level and the corresponding curve flattens around 90°. On the other hand, the amount of scattering shows a clear peak around 135°, pointing to the most effective energy coupling and structure extension conditions. Therefore, 135° polarization orientation is the most beneficial for single direction scanning in terms of energy coupling efficiency. For bi-directional scanning, symmetric 90° orientation may perform better in formation of a more uniform pattern of the scan lines. In contrast to the findings, one of the most regular LIPSS on metal were demonstrated using 45° orientation [77].

It should be noted that, in our experiment, polarization dependence of the damage threshold was not considered and the data are not corrected for this effect. However, other similar tests (1030 nm, 1.4 ps, $F_{\mathrm{pk}} \sim 2.5 \times F_{\mathrm{th}}$) on the galvo scanner, where the polarization was fixed and the scan directions were rotated instead, provided the same conclusion of the LIPSS dependency on the polarization orientation. It also revealed a period of this dependency to be 90°, which is probably a result of a different fluence regime or rotation of the scan area boundaries. These data are not shown as the smaller positioning accuracy of the scanning system did not provide homogeneously scanned areas.

## 3.3 Silicon scanning

During the course of my experiments, surface scanning of silicon was revisited numerous times. Every time with different laser parameters (pulse duration, wavelength, $M^2$, repetition rate, polarization, beam shape) and scanning conditions (spot size, scanning speed, overlap, pulse arrangement, etc.). This resulted in a substantial dataset of ∼10700 processed images and ∼150 spreadsheets with outcomes. Such dataset is obviously impractical to be presented in whole. Even the toughest LIPSS enthusiast would be bored after seeing the $6437^{\mathrm{th}}$ image of the LSFL. Just on silicon. Therefore, typically expected results and trends are presented, followed by a discussion of specific features of the structures and observations.

Two prerequisite measurements, damage threshold and $N$-on-1 pulse irradiation were already described. If outcomes of these are known, it is typical to proceed with parametric space scanning. This process applies not only for silicon, but any material in general. Figure 38 shows a map of the structures resulting from a parametric scanning in the fluence – overlap ($\Psi_x = \Psi_y$) domain in a range of 0.18 – 1.02 J/cm$^2$ and 36.7 – 99 % with steps in the main part of 0.05 J/cm$^2$ and 3.3 %. As can be seen in the figure, variability of the structures increases, when the fluence approaches the damage threshold. Therefore, sampling steps in the fluence are reduced in this region to 1/2 and 1/4 of the initial one to fully capture the structure variability. Such detailed scans as shown are not typically used due to time requirements. However, it is not uncommon that in more sensitive points

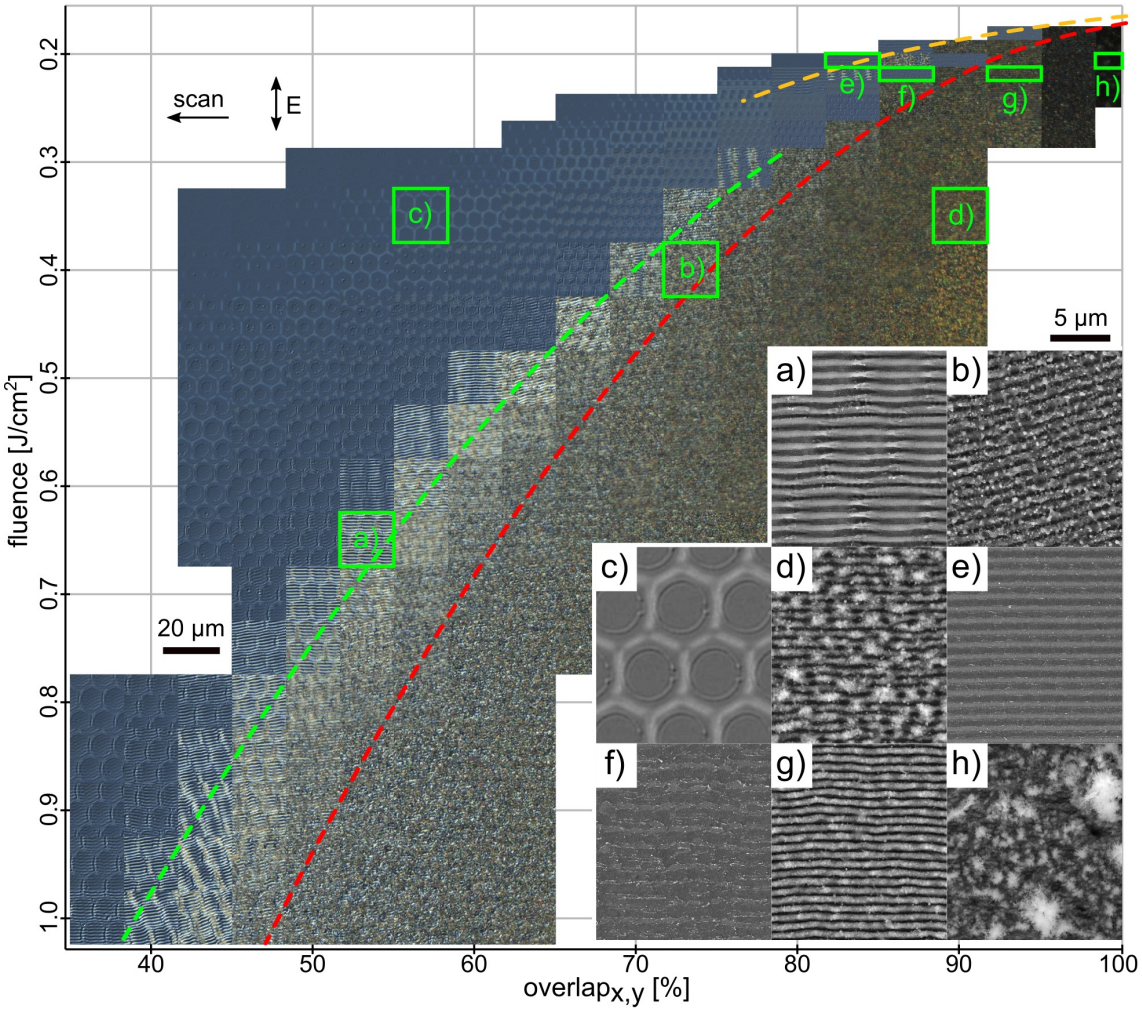


Figure 38: An OM-DIC map of the LIPSS scanning in a fluence – overlap ($\Psi_x = \Psi_y$) parametric space. Insets show magnified SEM (except c) OM-DIC) images of the corresponding green-highlighted regions. Dashed red, green and yellow lines are parabolic fits to onset of ablation, center of smooth LIPSS and highly-regular amorphization LIPSS respectively. Laser parameters: $\lambda = 1030$ nm, $\tau = 270$ fs, $\omega_0 = 6.3$ $\mu$m, $f_{\mathrm{rep}} = 2$ kHz, vertical polarization.

of the parametric space, parameter variation of even a 1 % can have a well observable impact on the result. As sampling the whole parametric space with such precision is just not practically feasible, an iterative approach with a decreasing step size, while focusing into a particular parametric region, can be used instead.

The main part of the Fig. 38 is made by tiling of the OM-DIC micrographs corresponding to the given parameters. Three main regions can be distinguished: the blue one, where only gentle surface modulation and superficial amorphization takes place; the gray-brown region corresponding to strongly ablated surface and the intermediate region in between, where shallow smooth LIPSS are present. From an empirical investigation one can see that regions of the LIPSS with similar properties are located on parabolas.

This is illustrated in the figure by three fitting functions

$$\Psi_{\mathrm{x,y}} = 105 - \beta\sqrt{0.4 * \left(F/\left[\mathrm{J/cm^2}\right] - 0.174\right)}, \tag{33}$$

where the function for $\beta = 104$ defines a border line between ablative and smooth LIPSS (red); for $\beta = 120$ marks a center of the smooth LIPSS region (green) and for $\beta = 165$ estimates center of the amorphization LIPSS region (yellow). Though, at least for the first two, classification of the structures into these groups is to some extent subjective. Together with rough spacing of the last one, this is probably a reason why these fitting trend lines imaginary intersect at $\Psi_{\mathrm{x,y}} = 105$ % (i.e. above 100 %) and $F = 0.174$ J/cm$^2$ (i.e. above $F_{\mathrm{th}} = 0.162$ J/cm$^2$ for N = 25 as shown in Fig. 30).

To better demonstrate the fabricated structures, detailed SEM micrographs of eight particular parametric points are included in the insets. Figure 38a shows topographically pronounced semi-ablative smooth LSFL. This kind of structures is found at the border between regions of ablative modification and modification without LSFL. However, for too small fluence it is hard to produce them homogeneously and for too high fluence formation of a circular rim around the spot can disturb its periodicity. Closer to the no-modification zone, it is common that the LSFL period fluctuates within the irradiation spot, being larger in the center and the shortest between two adjacent spots (perpendicular to polarization, here between the two scanning lines). Pronounced depth and relatively debris-free surface (reducing scattering) make this type of LSFL ideal for diffraction applications.

Towards the ablation zone (Fig. 38b), regularity and depth of the LSFL is usually increased. Unfortunately, this is for the price of substantially reduced smoothness of the structures as now they contain a plenty of redeposited material in form of nanoparticles and jets of material. Also in this regime, bubbles tend to form inside the LSFL periods, creating large amounts of localized LSFL period width changes. As a result, these structures strongly scatter light. Mentioned undesirable effects get worse with increasing fluence.

Figure 38c, exceptionally an OM-DIC image, illustrates periodic amorphization structures with a period of the irradiation spots spacing. No LSFL structures are observed in this region.

Deep in the ablative region, structures resembling substantial material melting are found (Fig. 38d). The underlying LSFL are still present with similar uniformity to that in Fig. 38b. Periods are smoother, but chunks of redeposited material interconnecting adjacent periods appear.

Now we focus on the parametric region close to the single-pulse damage threshold, where the parametric dependency of the resulting structures is substantial. Figure 38e shows highly regular and uniform amorphization structures observed for the smallest overlaps ($\sim$ 83 %). Period of these structures is typically close to the irradiation wavelength.

For slightly higher overlap, a region of modified surface without LSFL is located (Fig. 38f). The observed amorphization periodicity of 1.25 $\mu$m matches exactly the pulse line spacing. Therefore, these structures should be of similar nature as the structures in Fig. 38c. This interesting feature of the notch in the parametric space, of a no-LSFL region into a LSFL region, is more pronounced with decreasing spot size. For example,

scanning the same parametric region as in Fig. 38f, with the same parametric steps and $\omega_0 = 11.12$ $\mu$m, already does not show this feature. Interestingly, discontinuous quasi-periodic structures with a period of 0.27 $\mu$m, oriented perpendicular to the polarization are distributed uniformly over the whole surface.

Figure 38g shows again ablative LSFL. Their quality is close to that of the Fig. 38d, but without the interconnecting material chunks. Regularity of these structures is decent, some amount of nanoparticle decoration is still present.

Finally, surface irradiated with the largest overlap of 99 % in Fig. 38h shows no periodicity at all. Instead, fairly random multiscale structures are present. All of the OM-DIC images in the parametric map were captured with the same exposure settings. The last described structures are the least reflective. Similar multiscale rough surface is often generated artificially to decrease reflectivity in applications such as light sensors.

An important parameter of the LIPSS is their orientation. For metals and semiconductors, LSFS are observed to be predominantly perpendicular to linear polarization. However, as can be seen in Fig. 38b this perpendicularity is not strict. In fact, in most of the scans in Fig. 38, some tilting of the structures was observed. The structures can be tilted as a whole, or can be split into domains of different orientation. LSFL periods tend to be continuous at the borders of such domains in the ablative regime. For the employed scanning configuration of right to left scanning with vertical polarization, the tilt is typically in an anti-clockwise direction (Fig. 38b). This finding corresponds well with the anisotropic LSFL extension efficiency described in the previous section. Inclination of the LSFL to tilt towards the scanning direction was verified by scanning the same scans in opposite direction. Indeed, orientation of the structure tilt was flipped.

Structure orientation was examined across the whole parametric region in Fig. 38, but no evident general trend was found. Structures with scanning overlap $\Psi_{x,y} \geq 80$ % seem to have smaller tilts of $\sim 2°$. For lower overlaps one quarter of scans exhibit tilts of 10–16°. Abrupt variation by 10° at neighboring parameters was present. For highly uniform smooth structures their tilts seem to exhibit a peculiar behavior of being either close to zero (horizontal) or defined by an angle of one LSFL period per pulse spacing. This effect is demonstrated in detail in the Section 4.4.

Lastly, we should investigate behavior of the LSFL period. Figure 39 shows a clear decreasing trend of the period with increasing pulse overlap from 1.03 $\mu$m at ∼40 % down to 0.59 $\mu$m at 96.7 % overlap. In the literature, usually static $N$-on-1 irradiations were reported. To compare static and scanning irradiation, a connection between pulse number and overlap can be made by defining an effective pulse number $N_{\text{eff}}$ as

$$N_{\text{eff}} \equiv \frac{1}{(1 - \Psi_{\text{x}}/100)\,(1 - \Psi_{\text{y}}/100)}. \tag{34}$$

With this definition, the decreasing trend of the observed spatial period is in agreement with that of a static $N$-on-1 irradiation, where a period decreasing trend down to 70 % of the irradiation wavelength (although for 800 nm) was reported [51]. These reported values are shown in green in Fig. 39 for comparison. The LSFL period depends also on the fluence, with decreasing period for increasing fluence. However, this effect accounts only for several percent variation and is, therefore, included in the error bars.

In the end, it should be noted that appearance of the regular and largely uniform

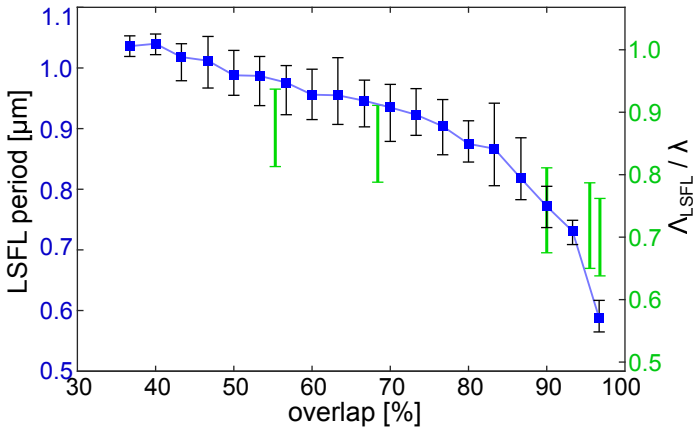


Figure 39: Dependency of the Si LSFL period on a pulse overlap. Green: comparison with a period change in an $N$-on-1 irradiation (800 nm) from Ref. [51].

periodic structures across the whole parametric space, as presented in Fig. 39, is strongly dependent on various other parameters. It took numerous experimental iterations to obtain a set of correct parameters to perform and present this scan.

***Other LIPSS remarks***

Low fluence, high overlap regime is also characteristic by a strong threshold behavior of structures fabricated within. This means, the scanned surface shows none to little modification, until suddenly a surface defect triggers creation of the periodic structures.

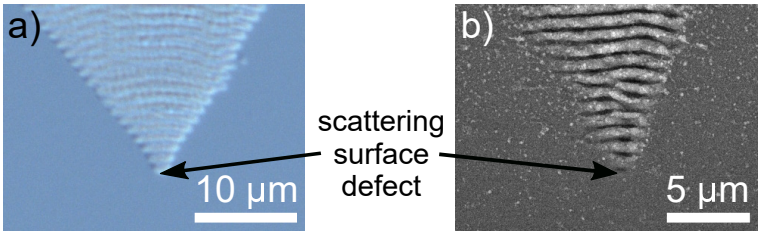


Figure 40: Threshold effect initiation of the a) amorphization (OM-DIC) and b) ablative LIPSS (SEM) in a homogeneously scanned area. Vertical polarization, horizontal scanning.

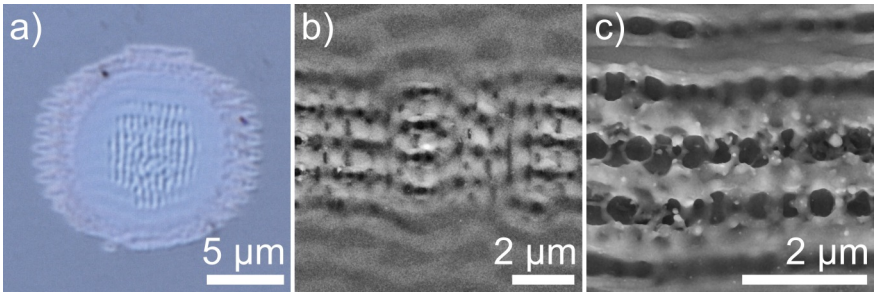


Figure 41: Coexistence of two LIPSS orientations in silicon in a) static irradiation, near-damage-threshold fluence and high pulse number ($\omega_0 = 22.6$ $\mu$m, $F_{\mathrm{pk}} = 0.22$ J/cm$^2$, $N = 25$) and in single line scanning for b) lower and c) higher fluence. Vertical polarization, 270 fs.

These then serve as scattering center during subsequent scanning passes and through a positive feedback further extends the surface modification. This effect applies for both amorphized and ablative structures as demonstrated in Fig. 40. In practice, when a large surface is being scanned, such triggering events occur randomly within the scanned area. Generated LSFL are extending along the scanning and eventually merge together. Then periods of the two merging structures either align perfectly or create a merging defect that may "propagate" for a significant distance. The exact scenario again depend on specific experimental parameters.

Another effect well observable in the near damage threshold regime is formation of $\lambda/2$ LSFL-II structures parallel to the laser polarization. Figure 41a shows an example of such structures in an $N$-on-1 irradiation where the typical horizontal LSFL are overlapped by vertical periodicity with half the period. Similar high spatial frequency structures can be sometimes found also after surface scanning, when these are localized inside of the grooves between individual LSFL periods for either lower or higher fluence (Fig. 41b, c respectively).

To achieve microscopically uniform structuring across the whole scanned area, a fragile balance between pulse fluence and overlaps must be maintained. More precisely, a balance between feedback from nearby already existing periods needed for coherent LIPSS extension and amount of available energy needed to imprint the local field into the material surface.

Spatial overlapping of the Gaussian pulses inherently produces microscopically non-homogeneous spatial distribution of energy and, therefore, it is problematic, if not impossible, to retain this balance in all points on the surface, especially for low overlaps. Figure 42a, similarly to the Fig. 38a, demonstrates this inhomogeneity effect by a variation of the LIPSS morphology at the periphery of the laser pulses scanned in a hexagonal pattern. In the central horizontal scanning line, two light-colored columns of narrowed LIPSS periods are clearly visible between the pulses. Additionally, two LSFL periods between the scan lines exhibit shorter and narrower periods with significant bending and roughness. Moreover, Fig. 42b and c demonstrate significant period narrowing in a single vertical line scanning by picosecond pulses. Formation of bubbles in the LSFL periods is evidently a dominant source of the single period roughness.

All of these are unwanted effects. Luckily, from the experimental investigation we

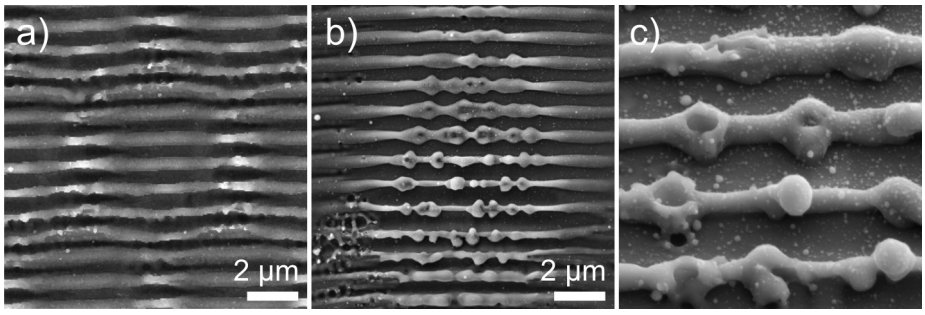


Figure 42: Modulation of the LSFL period and aspect ratio a) at the periphery of every pulse in 2D scanning with femtosecond pulses and b) picosecond pulses in a single vertical line scanning with larger $\omega_0$. c) A magnified side view of b). Vertical polarization, horizontal scanning.

found, there are several ways to (partially) suppress them. Shorter laser pulses may help to avoid excessive material melting and bubble formation. Smaller spot size seems to be beneficial with overall uniformity. Finally, fine tuning of the processing parameters around the current parametric set and along the parabolic region specified in Fig. 38 helps to smooth the period irregularities at the spot periphery.

However, some sets of processing parameters were predominantly problematic. For example, scanning with laser pulses in the picosecond range. Figure 43 shows a map of a parametric scan in the fluence – overlap space for 6 ps laser pulses. We can see, that for fluences up to ~0.8 J/cm$^2$ there is a sharp transition from surface ablation to mild modification, even though sampling of the parametric space is relatively dense with steps of 0.036 and 0.024 J/cm$^2$, and 2.5 %. An inset parametric matrix with steps of 0.014 J/cm$^2$ and 1 % shows a region of the onset of more gradual transition from ablation to mild modification regime. Taking a closer look at the adjacent pulses in the second inset, structure changes can be seen within the scan. While there are gaps

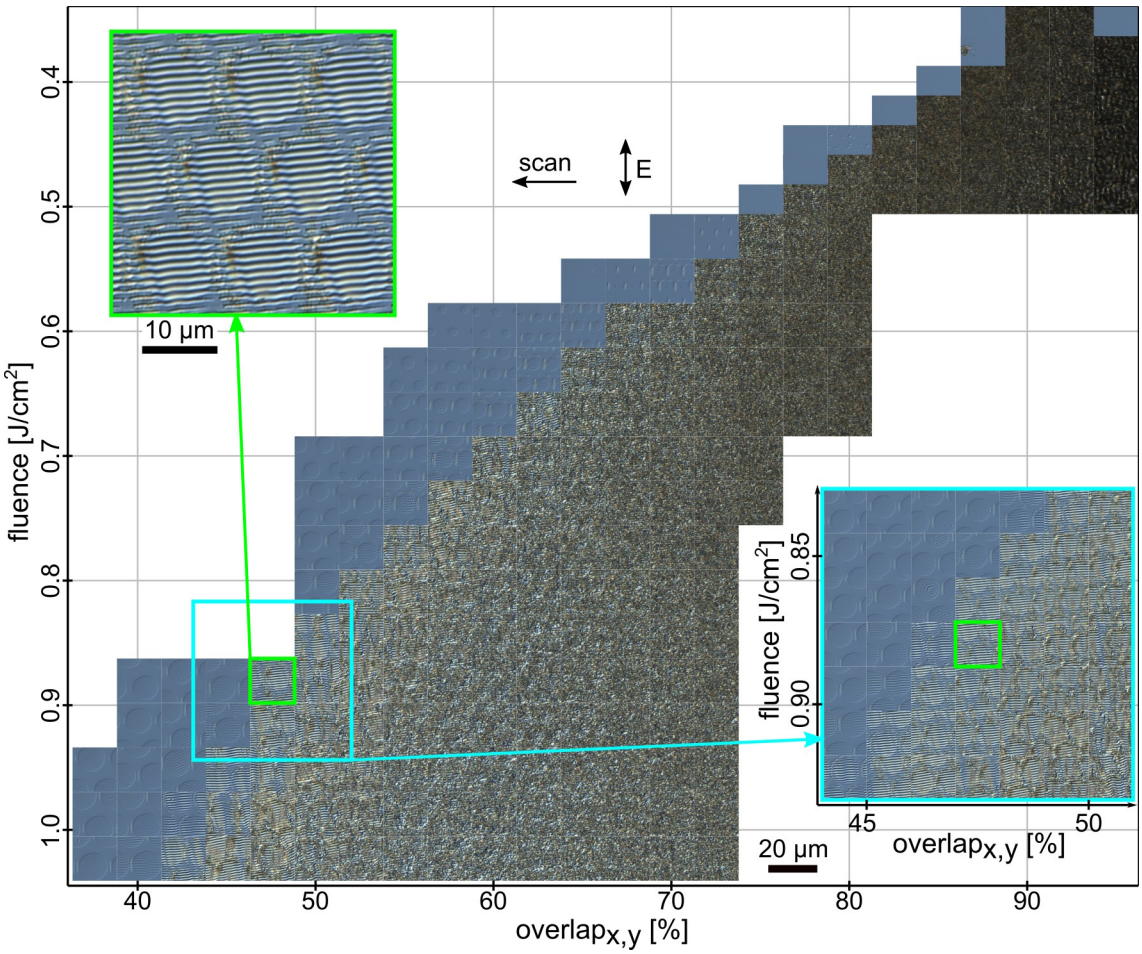


Figure 43: An OM-DIC map of the LIPSS scanning in a fluence – overlap ($\Psi_x = \Psi_y$) parametric space for laser parameters: $\lambda$ = 1030 nm, $\tau$ = 6 ps, $\omega_0$ = 10.9 $\mu$m, $f_{\mathrm{rep}}$ = 2 kHz, vertical polarization. Insets include a parametric scan with fine resolution and a magnified view of the LSFL for $\Psi_{\mathrm{x,y}}$ = 47.5 %, $F_{\mathrm{pk}}$ = 0.88 J/cm$^2$.

with missing modification between adjacent pulses at one position, excessive ablation can be found nearby. The problem is, for picosecond pulses these two extremes often coexist, what prevents uniform surface structuring with LSFL. Moreover, this inset shows line discontinuities / period phase mismatching in the direction from top-left to bottom-center. Typically, these discontinuities develop into lines of no topografical modification propagating through the whole scanned surface (see Appendix C, Fig. 75d). This, not yet fully understood effect, was a significant problem in the most of the LSFL surface scanning experiments with picosecond pulses.

Comparing the parametric scans for picosecond (Fig. 43) and femtosecond (Fig. 38) pulses, we first notice a larger damage threshold in the ps regime. Single-pulse threshold 0.47 J/cm$^2$ is more than twice higher and onset of ablation for 95 % overlaps is approx. 80 % higher. This corresponds well with the shift of the onset of gradual transition between ablation and mild modification to higher fluences. In the *ps* regime the highly variable resulting structures are not present, but this may be affected also by slightly different spot size. The *ps* scan was not performed for larger fluences due to the above discussed (Fig. 42) adverse effects start to be manifested in this range.

In conclusion, it is more problematic to achieve uniformly scanned areas with ps pulses than with shorter pulses. On the other hand, it seems that with ps pulses it is easier to write smooth ablative LSFL at lower overlaps, even in cases where the damages of the successive pulses do not fully overlap. However, in this case the uniformity of the structures may be low.

### 3.3.1 Large-area regular structures

In the previous section, general assumptions on the LIPSS scanning parameters were discussed. Here, particular examples of the best LIPSS achieved by Gaussian beam scanning of silicon are presented. Figure 44 shows such areas covered by ablative (left), smooth ablative (right) and amorphized LSFL (bottom).

These representative structures were obtained in different experiments. The corresponding processing parameters are summarized in the Tab. 12. In all three cases, linear scanning stages and perpendicular beam incidence were used.

To proof that the LSFL in the bottom image of the Fig. 44 are indeed of amorphous origin, $\mu$-Raman spectroscopy of these structures is shown in Fig. 45. The Raman spectra were evaluated along the green line in the OM image for a spectral band at 457 cm$^{-1}$. Clear signal intensity modulation is visible. However, it seems the amorphization is not spatially uniform as additional fluctuations with a period similar to the scanning line spacing can be seen in both the optical image and the Raman spectra. This can be caused by a limited positioning accuracy of the DDSM/100 stages. The other two structures were fabricated with the more precise scanning system.

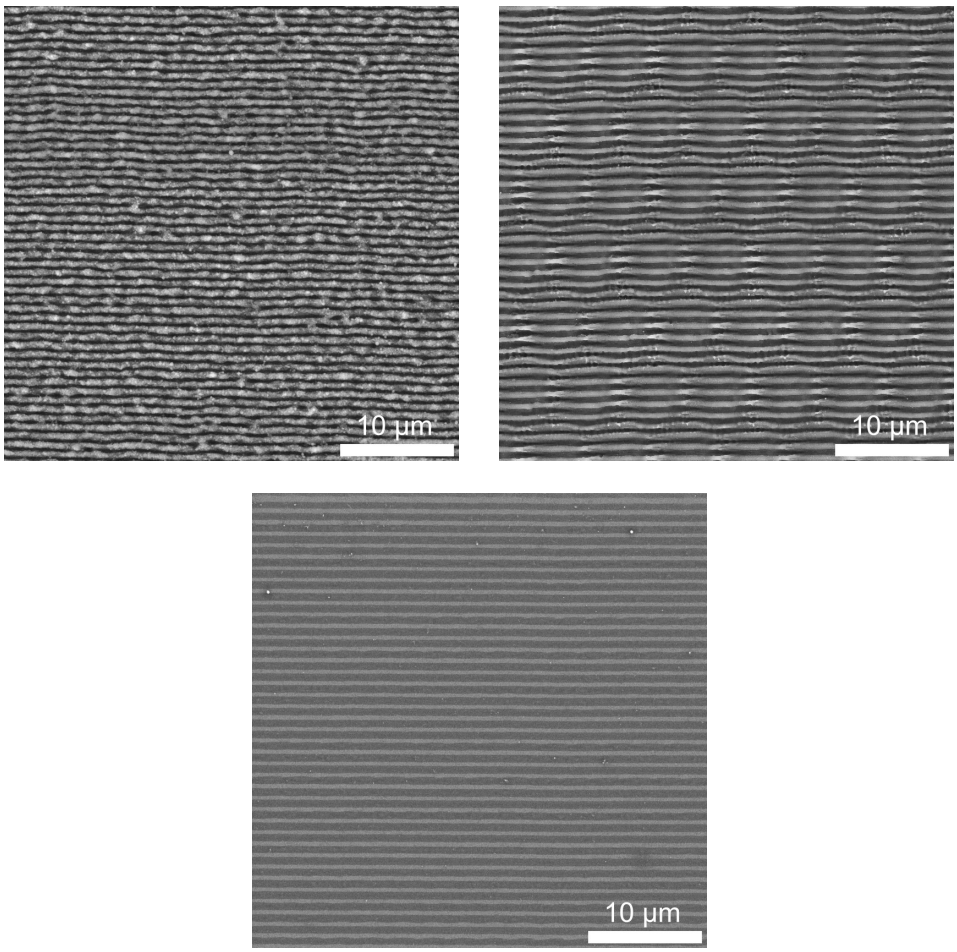


Figure 44: Demonstration of silicon structuring by LIPSS with Gaussian pulses. Top left: ablative LIPSS, top right: smooth ablative LIPSS, bottom: amorphized LIPSS. Vertical polarization and horizontal laser scanning. Other parameters are summarized in the Tab. 12.

| **LSFL type** | **ablative** | **smooth ablative** | **amorphized** |
|---|---|---|---|
| $\omega_0$ [$\mu$m] | 7.0 | 6.3 | 7.0 |
| $f_{\mathrm{rep}}$ [kHz] | 33.3 | 2 | 33.3 |
| pulse spacing [$\mu$m] | 1 | 5.9 | 2.2 |
| in-line overlap [%] | 93 | 53 | 84 |
| scan speed [mm/s] | 32.6 | 11.8 | 74.6 |
| line spacing [$\mu$m] | 2.8 | 5.9 | 2.8 |
| line overlap [%] | 80 | 53 | 80 |
| $F_{\mathrm{pk}}$ [J/cm$^2$] | 0.33 | 0.65 | 0.27 |
| pulse alignment | rectangular | hexagonal | rectangular |
| pulse duration [fs] | | 270 | |
| wavelength [nm] | | 1030 | |

Table 12: Processing parameters of the LSFL structures demonstrated in Fig. 44.

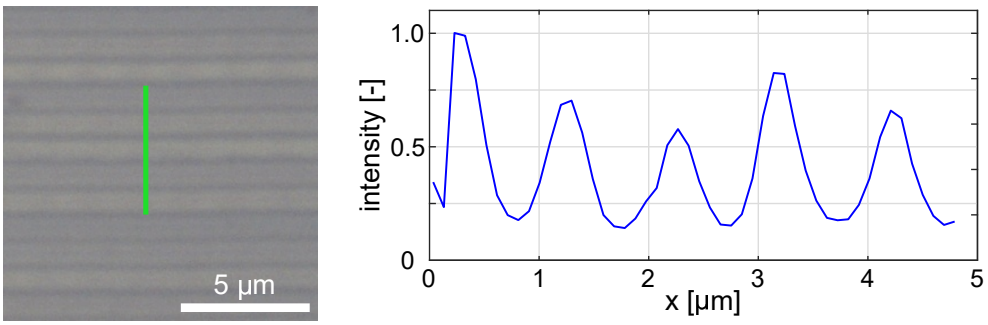


Figure 45: Amorphous LIPSS and proof of amorphization by $\mu$-Raman spectroscopy. The graph shows intensity of the Raman signal at 457 $cm^{-1}$ along the green line in the image. Excitation 532 nm, 100x objective.

### 3.3.2 LIPSS stripes

Through the LSFL scanning experiments focused on highly regular and uniform structuring, there was a persisting troublesome effect of the LSFL being produced transform into disordered, irregular stripe pattern, as shown in Fig. 46a. Here, adjacent LSFL stripes are mostly mutually misphased, creating separating inhomogeneous lines where no surface modification is apparent. In this case, under detailed observation it can be often found that the LSFL are actually continuous, having a stepped or sinusoidal profile. Only the amount of modification is strongly modulated and the continuity is not visible at first.

After detailed investigation, we found out that specific processing conditions exist, where such peculiar pattern of LIPSS stripes can be fabricated in a controlled way with high regularity and uniformity. This finding was reported in a publication [65]. The main results and additional results left out from the publication are presented below.

Figure 46b demonstrates such stripes of LIPSS created by *horizontal* beam scanning. It is stressed that the lines develop perpendicularly to the scanning direction. Another unique property of this pattern is a location of the Gaussian pulse centers, i.e. peaks

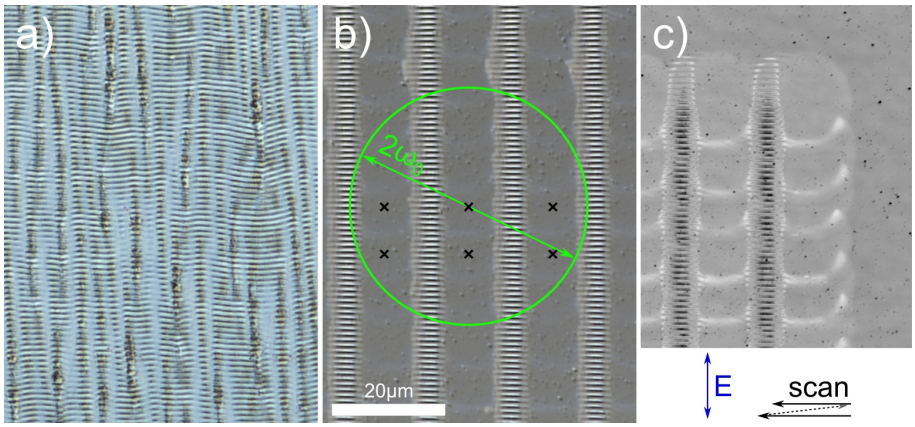


Figure 46: Stripes of the LIPSS on silicon: a) unordered stripes, b) regular stripes (OM-DIC) and c) CLSM image of b). Gaussian beam spot diameter (green), pulse centers (black crosses), polarization and scan direction are indicated. b) and c) modified from [65].

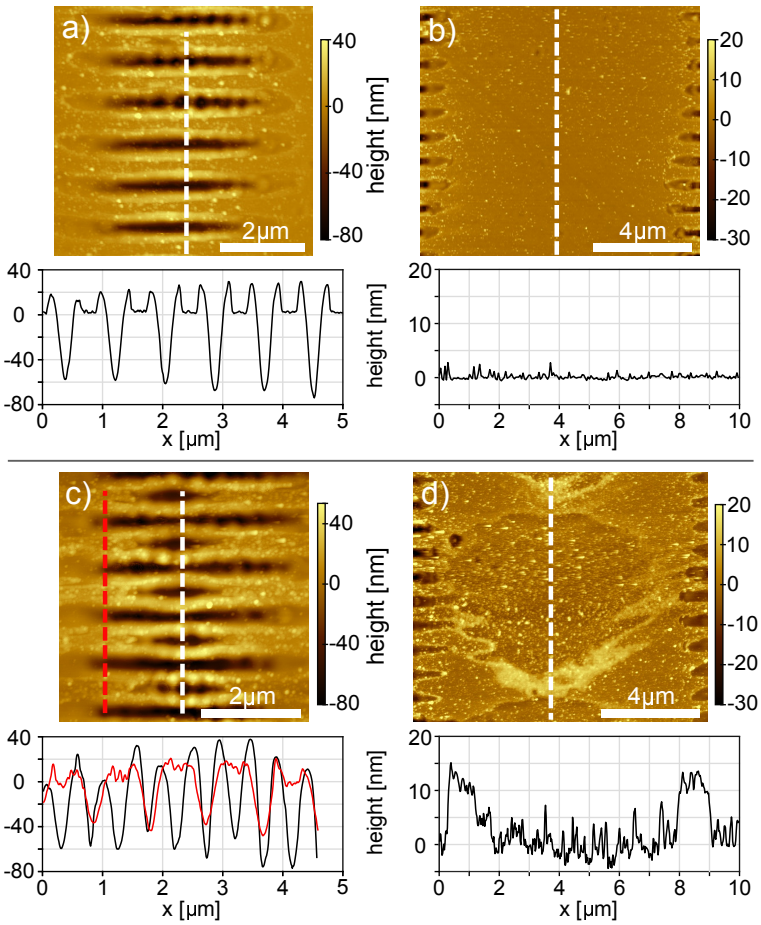


Figure 47: a), c) AFM images of the LIPSS stripes and b), d) stripe separating region for processing parameters: $\omega_0 = 21.2$ $\mu$m, linespacing 8 $\mu$m. a), b) $F_{\mathrm{pk}} = 0.268$ J/cm$^2$, $\Psi_{\mathrm{x}} = 67$ %. c), d) $F_{\mathrm{pk}} = 0.298$ J/cm$^2$, $\Psi_{\mathrm{x}} = 64$ %. a) and d) modified form [65].

of fluence (indicated by black crosses), which are *in between* the LIPSS stripes. This is clearly visible in Fig. 46c, a CLSM image of a corner of the scanned area. Further, the Gaussian beam diameter, indicated by a green circle, can be several times larger than the pattern spatial period. The approach for its fabrication is therefore completely different from a simple vertical scanning or direct laser interference patterning [165].

LSFL in the stripes are initiated as usual through amorphized LSFL and after several scan lines evolve into ablative LSFL. Figures 47a,b show a single stripe and an area separating two stripes for lower fluence and pulse overlaps. Some resolidified material ejected from the grooves can be seen as protruding rims at their edges. No apparent modification occurs between the stripes. For higher fluences and overlaps, period splitting [166,167](Fig. 47c) is often observed. Here, an additional groove is created in the initially plateau region between two subsequent ripples, thus doubling the LIPSS spatial frequency. Appearance of ablation craters between the LIPSS stripes is also typical for this regime (Fig. 47d).

The first attempt to explain this intriguing pattern was by accumulated incident fluence [95]. Obviously, if a surface is scanned by spaced Gaussian pulses, the received

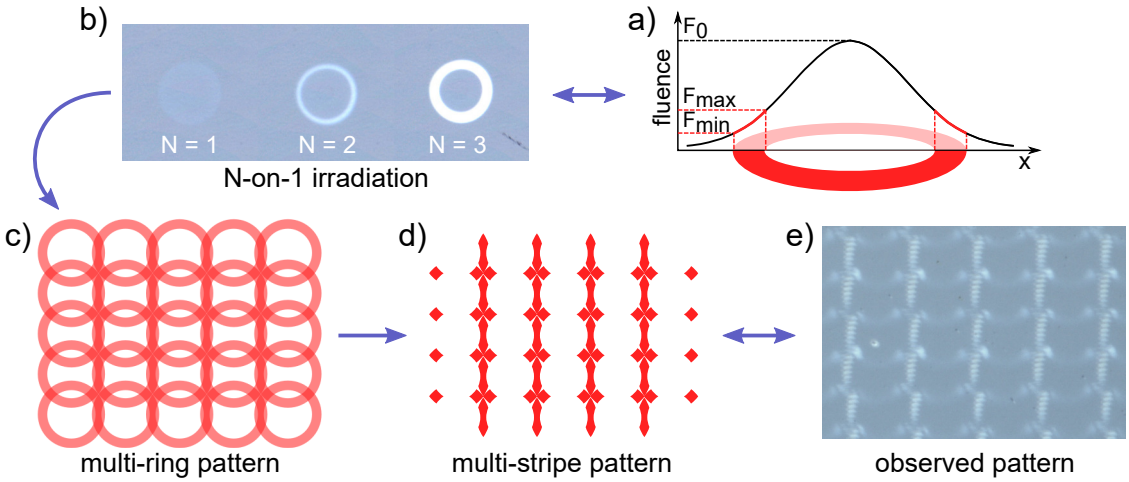


Figure 48: The LIPSS stripes creation process.

amount of the accumulated fluence must vary in every point. However, for our conditions this variation was found to be negligible, moreover with a slight excess of the accumulated fluence in between the stripes, compared to the locations over them. Therefore, another explanation of the LSFL stripes formation was proposed.

A process of the LIPSS stripes formation is illustrated in Fig. 48. It was previously shown for single pulse (Fig. 32) and $N$-on-1 pulse irradiation (Fig. 29), that an annular region of amorphized material can be created on mono-crystalline silicon. Such region is marked red in Fig. 48a). The underlying reason is (partial) melting of the material followed by fast quenching of the melt, as was already proposed in other works [168]. In the central part of the irradiated zone, the highest received fluence together with geometry of heat diffusion allows the cooling process of the melt to be slow enough for material recrystalization. Laser-induced crystallization of amorphous silicon was already

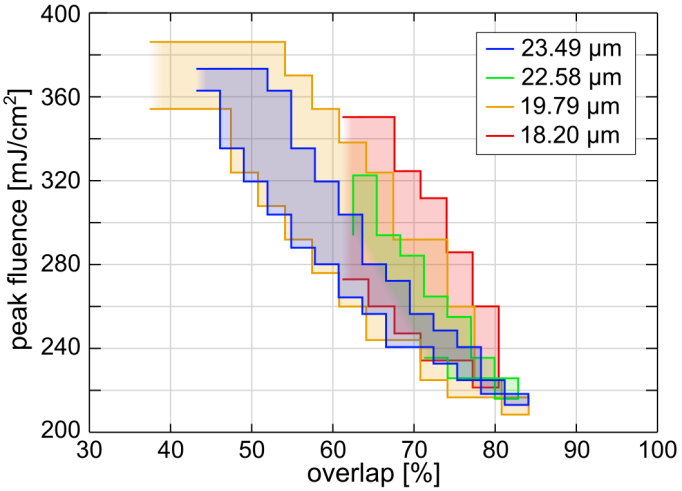


Figure 49: Localization of the LIPSS stripe structures in the parametric space of fluence and in-line overlap for different Gaussian beam waist radii $\omega_0$ (1030 nm, 270 fs, silicon).

demonstrated experimentally [169]. On the contrary, in the outermost melted region, a kinetically limited solidification results in an amorphized material state. Due to differences in optical and thermophysical properties of the crystalline and amorphous silicon (Tab. 8), amorphous silicon is more prone to further modification, in particular due to its lower melting temperature, melting enthalpy and thermal diffusivity compared to c-Si. This can be seen in the $N$-on-1 irradiation in Fig. 48b), where succeeding pulses significantly increase the amount of amorphization. Applying this amplification effect to beam scanning, a pattern of possible amorphization is constructed in Fig. 48c). However, significant amorphization will occur only in overlapped regions (Fig. 48d). And indeed, this is exactly the pattern observed for low fluence and overlap, where surface scattering feedback from adjacent LIPSS is negligible (Fig. 48e).

At higher fluence/overlap, where pronounced continuous amorphized stripes are produced, the crystalline – amorphous LIPSS will build up. Eventually, due to increasing degree of modulation and positive inter-pulse feedback, pronounced ablative LSFL are formed. Though, it should be noted that LIPSS are not observed in all scenarios of regular surface amorphization [170].

A geometric pattern of possible amorphization (Fig. 48c) will occur only for a specific combination of fluence and pulse overlap. Such range is experimentally mapped in Fig. 49. As the scanning experiment was repeated several times with a slightly different beam diameters, dependency of this range on the beam spot radius $\omega_0$ was also found. Soft edges of the regions indicate continuation beyond the experimentally investigated parametric range. It can be seen that the smaller the spot size, the larger the region of the LIPSS stripe occurrence. However, the smaller the spot size, the better the scanning accuracy must be to maintain constant overlaps. This is why it was possible to perform these scans with a relatively large spot size on relatively low accuracy linear stages (DDS100/M, Tab. 4). The positioning accuracy is also a reason why sufficiently large line spacing of 8 $\mu$m was a fixed parameter. There were attempts to vary also this parameter, but, at that time the only available motorized stages were inducing significant non-uniformity in the in-line spacing that led to non-repeatable results. Its effect was similar to varying the in-line overlap anyway.

It is worth noting, that as for any other LIPSS scanning, several initial scan lines may be necessary to fully build up the LSFL in the stripes.

## 3.4 Fused silica

### 3.4.1 Orientation of the LIPSS and knitting patterns

Fabrication of LIPSS on glass, and dielectrics in general, follows the same principles that were already described in the previous section for silicon. The main differences are usage of larger fluences due to larger band gap of the materials and existence of conditions to generate typically parallel [45,171] but also perpendicular [172,173] metal-like orientation of the LSFL with respect to the polarization.

This chapter presents first attempts to fabricate LSFL on fused silica (FS) and Ultra-Low (coefficient of thermal) Expansion glass (ULE). These experiments were partially performed during an internship in the Center for physical sciences and technology (FTMC) in Vilnius, and were the first experiments in the course of the PhD. ULE is a titania-silicate glass with three orders of magnitude lower coefficient of thermal expansion than FS (see Section 2.2 Tab. 6 for full comparison). As thermal expansion and contraction after irradiation may play a role in the LIPSS creation, ULE was chosen to be compared to the FS to verify if any difference in the LIPSS fabrication can be observed.

In the following experiments, initially a commercial micromachining setup (similar to the one introduced in the Section 2.1.5 Fig. 21) with linear scanning stages and a Pharos

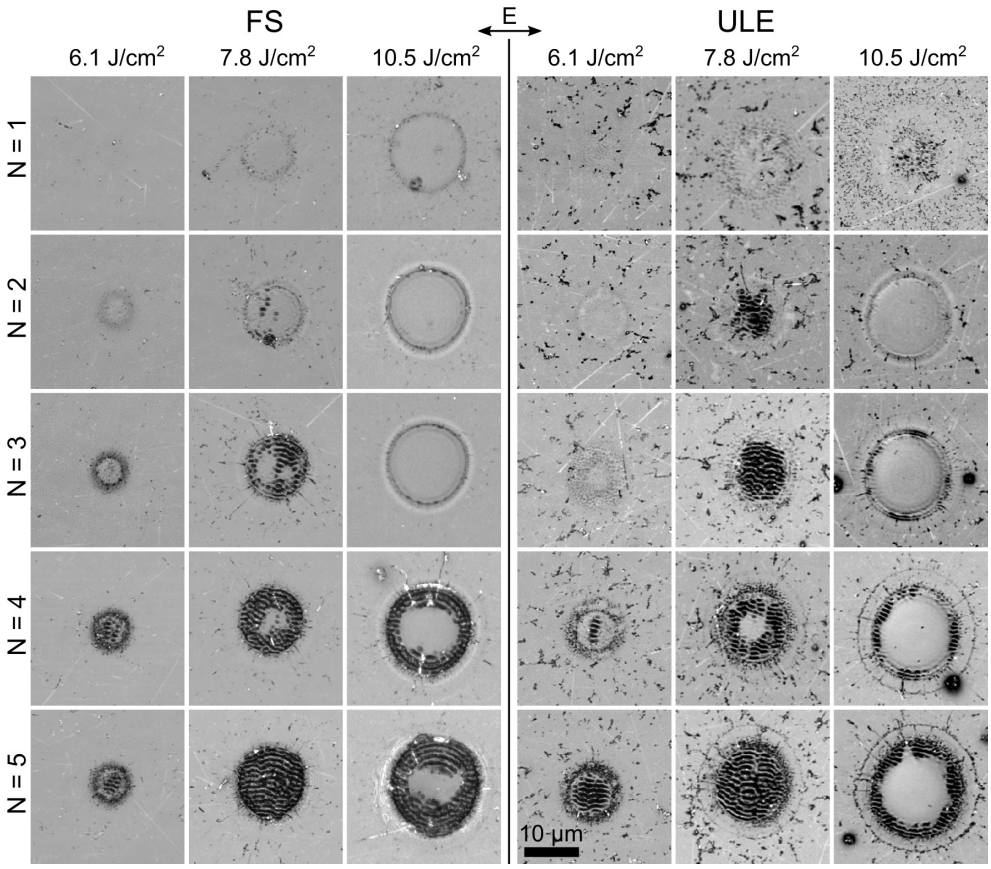


Figure 50: Formation of LIPSS in $N$-on-1 irradiation as a function of applied number of pulses and laser fluence on fused silica and ULE glass.

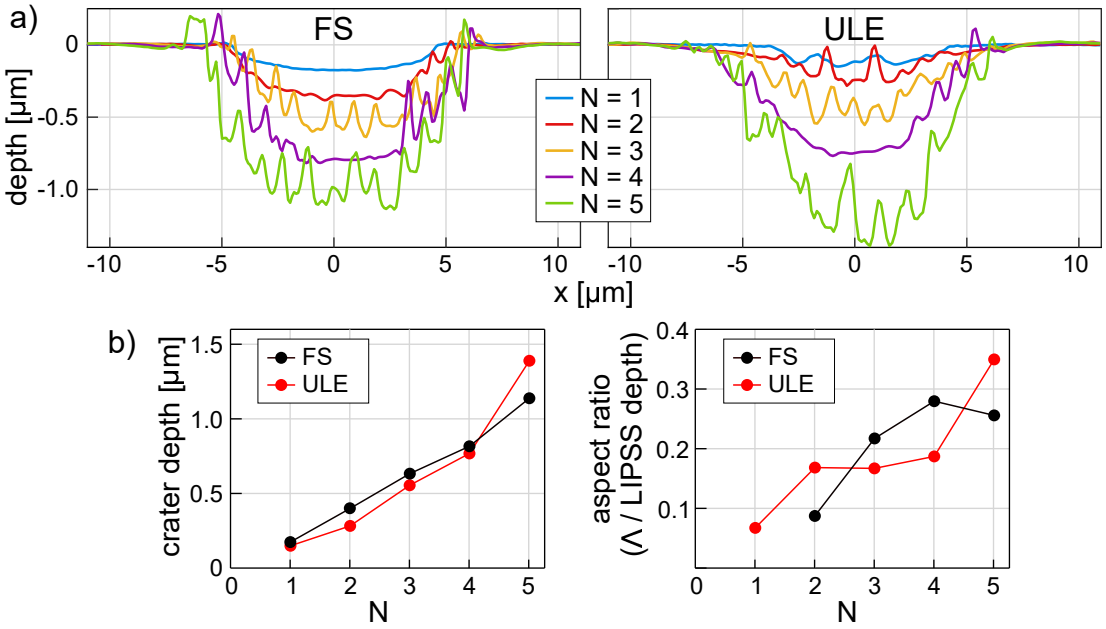


Figure 51: a) Crater profile evolution with increasing number of pulses in $N$-on-1 irradiation of FS and ULE glass for a peak fluence of 7.8 J/cm$^2$. b) Corresponding crater depth and LIPSS aspect ratio.

laser (1030 nm, 290 fs, $2\omega_0 \sim 24\,\mu$m) was used. Later it was reproduced on a galvo scanner and the Pharos laser in the HiLASE Centre.

The first step was an analysis of the $N$-on-1 irradiation spots. Figure 50 shows selected CLSM micrographs of the irradiation craters on both FS and ULE. Coarse mapping of the fluence and pulse number reveals that five pulses with a fluence of 7.8 J/cm$^2$ produce LSFL structures of acceptable quality. Below these values, in terms of both pulse number and fluence, the LIPSS either did not completely cover the spot surface, or were not present at all. On the other hand, for higher fluences, central part of the irradiated spot started to be already ablated and optically smooth.

Irradiation spots for the fluence of 7.8 J/cm$^2$ were further analyzed. Figure 51a shows CLSM line profiles of the ablation craters made on FS and ULE. The profiles clearly reveal a process of the LIPSS formation on samples surfaces. For both samples, a flat crater bottom can be observed for four pulses and LIPSS reappearing with the fifth pulse.

Figure 51b summarizes the crater depth evolution and LIPSS aspect ratio for both samples. Knowing roughly the laser fluence and pulse overlap where the LIPSS form in the $N$-on-1 configuration, the laser scanning experiment (to irradiate large area sample surface $\sim 1 \times 1$ mm$^2$) was performed, where the parametric space of the fluence and overlap was set around the previously discovered values.

Figure 52 shows some of the obtained LIPSS morphologies for FS and ULE glass in scanning conditions. Again, a rough parametric scan revealed a region of the LIPSS formation for fluence of 7.8 J/cm$^2$ and 75 % overlap on both glasses. In this case, even a small change of the parameters caused a dramatic change of the resulting surface morphology. For overlaps smaller than 75 %, individual spots can be distinguished, possibly with a few periods of the LIPSS forming at the edge regions of the pulse-modified surface for higher

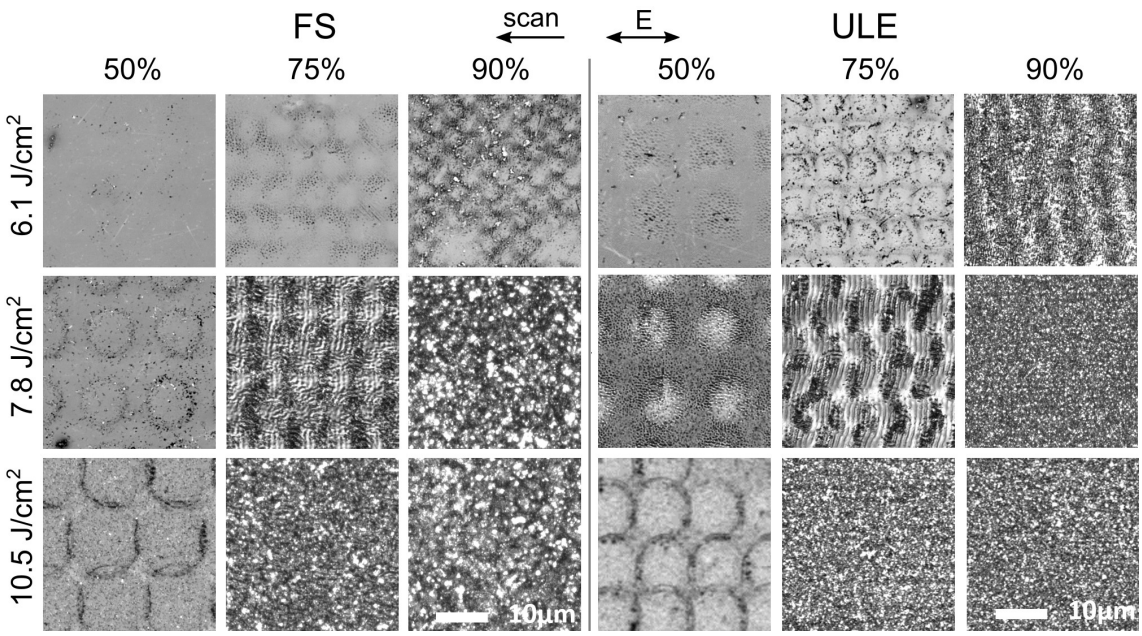


Figure 52: Formation of LIPSS under scanning irradiation as a function of pulse overlap and coarse change of laser fluence on FS and ULE glass.

fluences. Below 7.8 J/cm$^2$, little or no modification was observed. In contrary, for higher fluences and higher overlaps only a chaotically rough surface showing no periodicity was found.

It should be noted that, the orientation of the LIPSS changed direction from parallel with the polarization, as was observed in the static irradiation (Fig. 50), to perpendicular.

A closer look at the scanning results in the "optimal" region reveals an interesting quality difference between the two glasses. While the structures on the ULE glass surface consists of coarse LSFL oriented perpendicular to the polarization, structures on FS combines both parallel and perpendicular LSFL domains. This can be also seen from a Fourier analysis of the images in Fig. 53. Two vertically located, highly dispersed (due to small number of periods) regions can be seen. In both cases, the LIPSS periods are equal to the applied laser wavelength and the LIPSS wave vector deviates a few degrees from the laser polarization.

Afterwards, another iteration of scanning was conducted in HiLASE. It returned a slightly different value of the optimal fluence 6.1 J/cm$^2$, which was previously discarded. This time, mutual orientation of the scanning direction and laser polarization, which has an effect on uniformity of the generated structures, was investigated. Therefore, FS surface was scanned in both parallel and perpendicular orientation, but actually no significant change was observed (Fig. 53 - left).

It must be noted that these additional experiments were conducted on other scanning system (a galvo scanner) at different repetition rate, what may explains the change in the fluence leading to the highest structure regularity. Additionally, as can be seen in Fig. 53-left, pulse spacing uniformity is poor. Spacing of $\sim 7\,\mu$m is close to the positioning precision of the galvo scanner and minor fluctuations in a scanning position drive the

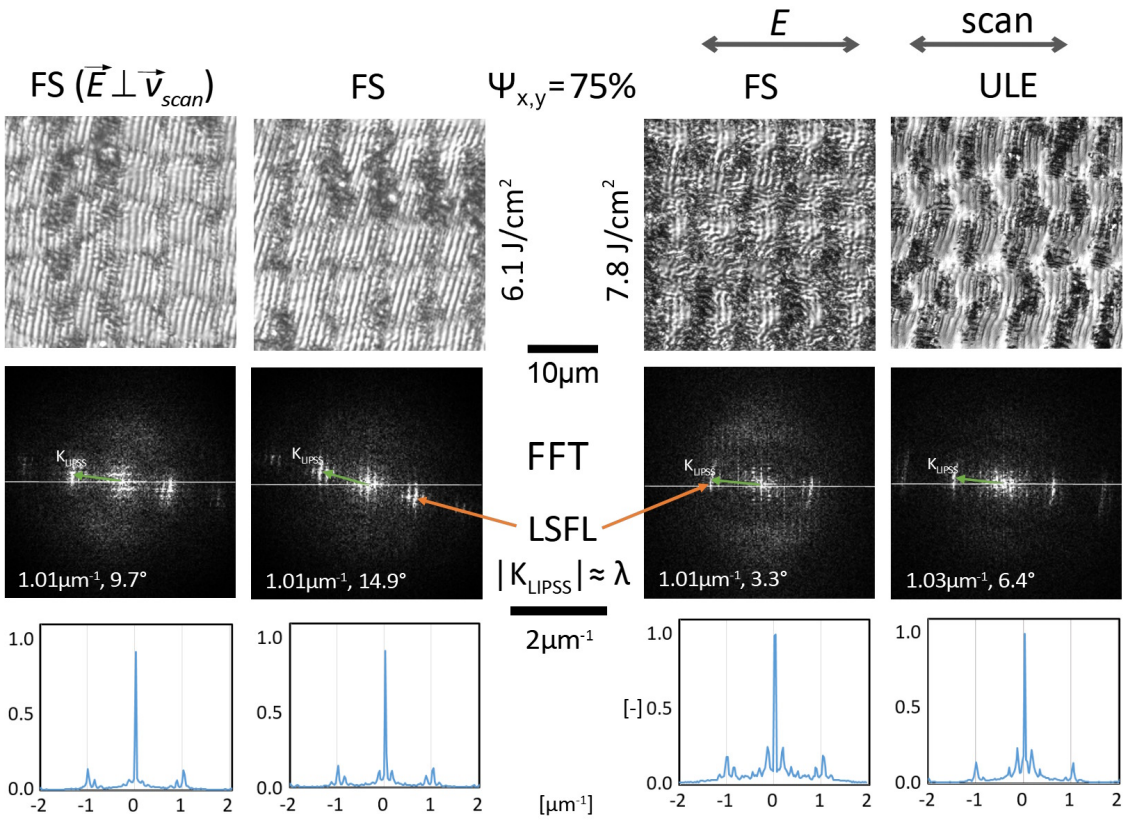


Figure 53: Spectral analysis of the LIPSS after laser scanning. CLSM images (upper row) were analyzed by a Fourier transform (FFT, middle row). Size of the LIPSS wave vector and its angle with respect to the polarization is indicated. Bottom row contains line plots from the corresponding spectra in the direction of the LIPSS wave vector. The first and second column depicts FS scanned perpendicularly and parallel to polarization at 6.1 J/cm$^2$. The other columns depict FS and ULE glass structuring with non-optimized fluence 7.8 J/cm$^2$.

LIPSS formation process off its optimal conditions.

This is illustrated in Fig. 54, where individual scanning lines are randomly displaced in vertically direction by less than $\pm 1.3$ $\mu$m. Such variation is strong enough to affect the LIPSS formation process from formation of no structures up to a strong surface ablation.

Coexistence of the perpendicular and parallel LSFL on FS, as shown in Fig. 52 and 53, may be explained by variations in the incident fluence. Based on calculations of the efficacy factor [42,45,55] (i.e. a scalar function predicting a possibility of non-homogeneous energy deposition to the surface with a particular periodicity and direction), there is a change in the preferred direction of energy deposition with a varying density of the photo-excited electrons (Fig. 55a,b). As can be seen in the graph in Fig. 55b, fluences occurring in the experiment are sufficient to generate electron densities necessary for this orientation change [174]. Taking into account Gaussian shape of the beam, a central (high fluence) part can generate enough free electrons necessary for the orientation change to occur, while the outer beam region will remain in the low fluence regime (Fig. 55c). This can lead to a periodically alternating LIPSS orientation (Fig. 55d). However, regularity of such LSFL is low, as the pattern is periodically interrupted and reestablished. Additionally,

diffraction on an edge of previous pulses is another effect, which can cause similar localized change of the LSFL orientation. This will be demonstrated in detail in the Section 4.3.

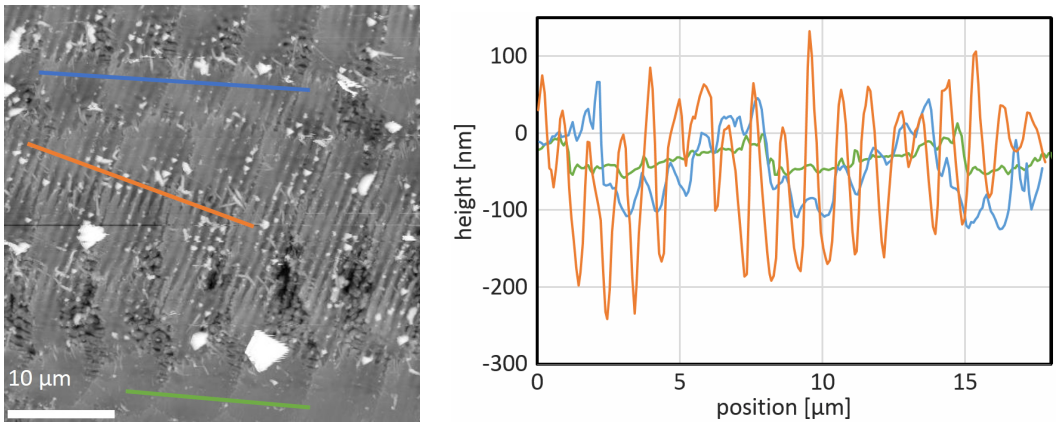


Figure 54: An AFM image of a LIPSS nanostructured FS surface with indicated positions of line profile plots shown in the graph. Chaotic variation of the line spacing significantly affects the LIPSS formation process. A surface tilt inside of the individual processing shots, as well as onset of the LIPSS formation with an increasing line overlap is clearly visible.

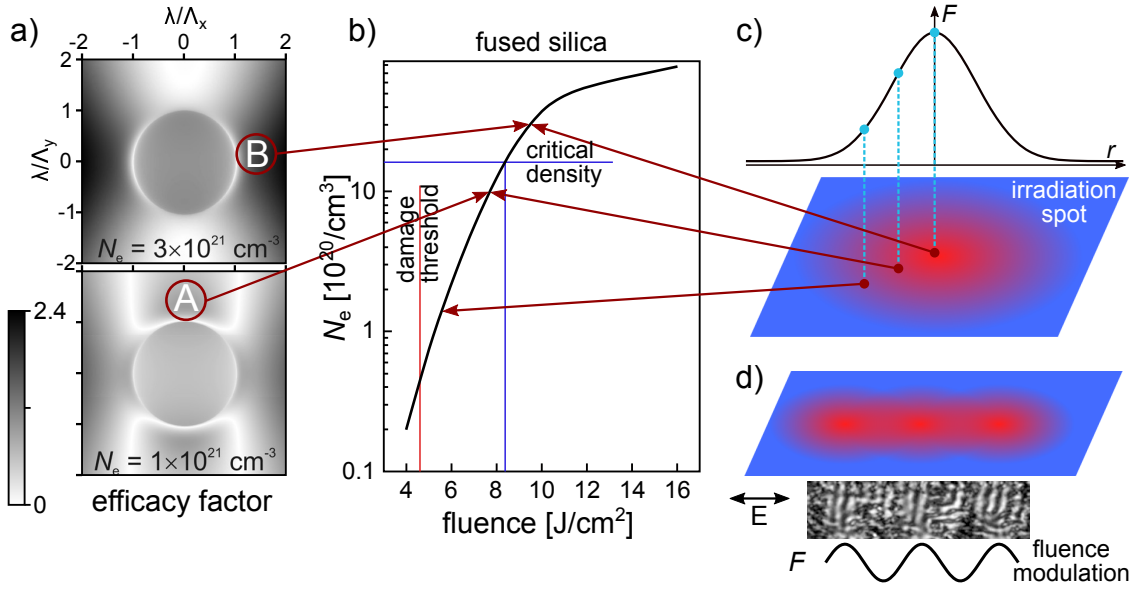


Figure 55: Possible explanation of the LIPSS orientation change: a) an efficacy factor (adapted from [45]) is dependent on excited electron density concentration. b) This density varies with the laser pulse fluence (adapted from [174]), which c) is locally non-homogeneous for the spatially Gaussian beam. d) Periodically modulated fluence distribution within the scan is then responsible for change of the LIPSS orientation.

### 3.4.2 Periodic structuring of fused silica

As can be seen in Fig. 54, scanning uniformity of the galvo scanner was poor. Therefore, after acquisition of a precise commercial in-situ scanning setup, LIPSS structuring of FS was revisited one more time. Investigation approach by a parametric search was similar as in the previous attempts. Additionally to the rectangular pulse arrangement, hexagonal arrangement with smaller variation of the accumulated incident fluence was used.

Figure 56 shows a parametric map of typical surface structures fabricated on FS for procesing parameters of $\lambda = 1030$ nm, $\tau = 265$ fs, $\omega_0 = 11.9$ $\mu$m and $f_{\mathrm{rep}} = 1.25$ kHz. When compared with analogical maps on silicon (Fig. 38, Fig. 43), it can be seen that appearance of the LIPSS (marked by green) is confined to a narrower parametric region between rough ablation and localized quasi-periodic structures, resulting from scattering on edges of adjacent ablation craters. Similarly narrow parametric range was observed in maps for single line scanning by Schwartz et.al. [175]. Additionally, for high overlaps and fluences around the damage threshold, structures with a double spatial frequency

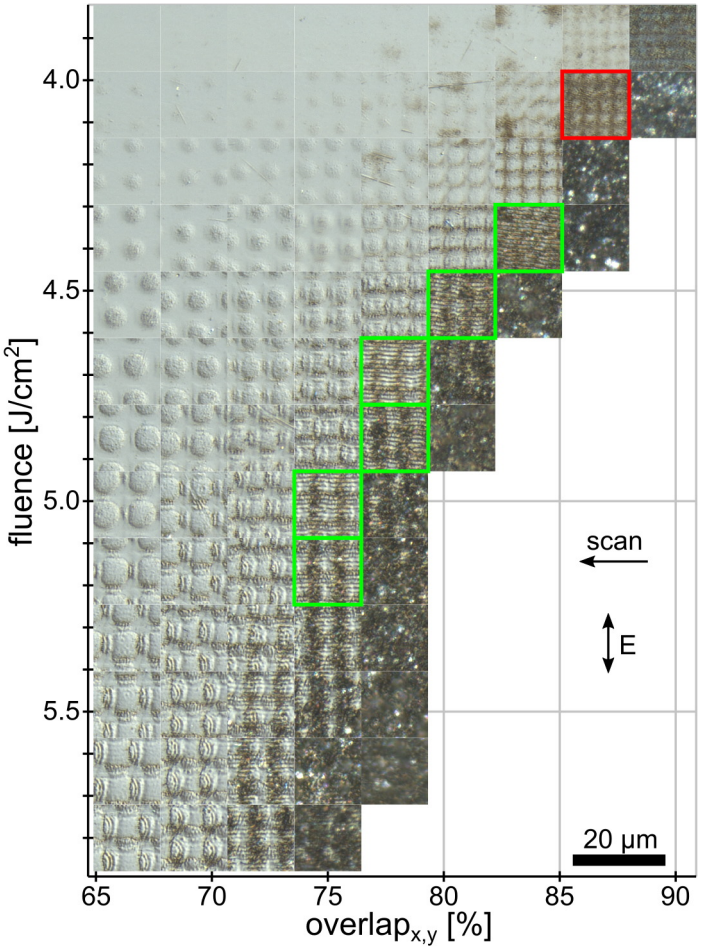


Figure 56: An OM-DIC map of the LIPSS scanning in a fluence – overlap ($\Psi_x = \Psi_y$, square grid) parametric space on FS. Green highlighted positions mark an appearance of the LSFL on larger area. In the red highlighted scan, 500 nm LIPSS are observed. Laser parameters: $\lambda = 1030$ nm, $\tau = 265$ fs, $\omega_0 = 11.9$ $\mu$m, $f_{\mathrm{rep}} = 1.25$ kHz.

(marked by red) can be found. Similar outcome was found also for the hexagonal pulse arrangement (not shown).

In FS, and dielectric materials in general, laser-induced generation of free electrons is a highly nonlinear effect. This in practice means a strong variation of the irradiation result on the processing parameters. As little as 0.5 % variation in both overlap and fluence leads to an observable changes. Obviously, such strict demand on stability of the processing parameters is not easy, nor cheap to achieve. Even in our case with a decent equipment and laboratory conditions it was verified, that a 2D surface scan, which was suspended for an hour and then continued, with exactly the same parameters, did not continue to generate exactly the same surface structures.

Nonetheless, generation of periodic surface structures was achieved on large areas. Figure 57 demonstrates LSFL structures on FS for scanning in a square (sq-scan) and hexagonal (hex-scan) grid. Minor differences between these two pulse alignments can be observed. It should be noted that no truly highly-regular and uniform structuring, as for silicon, was observed on FS and choice of the best quality LSFL is to some extent subjective. Even though, some general trends are observed. In the scan with pulses aligned in a square grid (Fig. 57a,b), variation of the modification amount, between pulse center vs pulse overlapping edge, is larger than for the hexagonally aligned pulses (Fig. 57d,e). AFM depth profiles are compared in Fig. 57h). Large-scale uniformity shows an opposite trend. Hex-scans often exhibit tilted streaks of no modification, as is clearly visible in Fig. 57f). Sq-scans seem to be more uniform in large scale, but often an oscillating pattern of increased/decreased modulation in odd/even columns is present. In any case, LSFL on FS written by Gaussian pulses are a combination of relatively smooth and rugged ablated ripples. Sadly, processing parameters for direct fabrication of continuous smooth LIPSS were not found. However, this does not exclude an option that such conditions exist. Processing with smaller spot size, higher repetition rate, different wavelength and pulse duration should be tested. There are hints from sapphire structuring [46], that large area of relatively uniform structures can be produced, just regularity needs to be improved. Irradiation with $\sim$ 6 ps, 1030 nm pulses was attempted, but instead of LIPSS generation, no modification, destructive ablation or self-focusing and ablation of the rear sample side was observed.

It is theoretized that quick etching of the rough FS LSFL in a diluted HF acid should improve the surface smoothness, but due to safety concerns, such option was not attempted. Another approach might be high temperature surface smoothing by bringing the sample up to the softening temperature [176] or by coating the surface with some filling material. The latter option was unintentionally tested, when a cleaning liquid (isopropylalkohol) with dissolved material, probably tape glue, wetted the structures in Fig. 57d and deposited the material into the ablation trenches. Resulting structures in Fig. 57g show no brown regions corresponding to the rough ablation. That means, the excessive roughness was indeed suppressed. However, surface coating modifies chemical and physical properties of the material and therefore is problematic for potential applications.

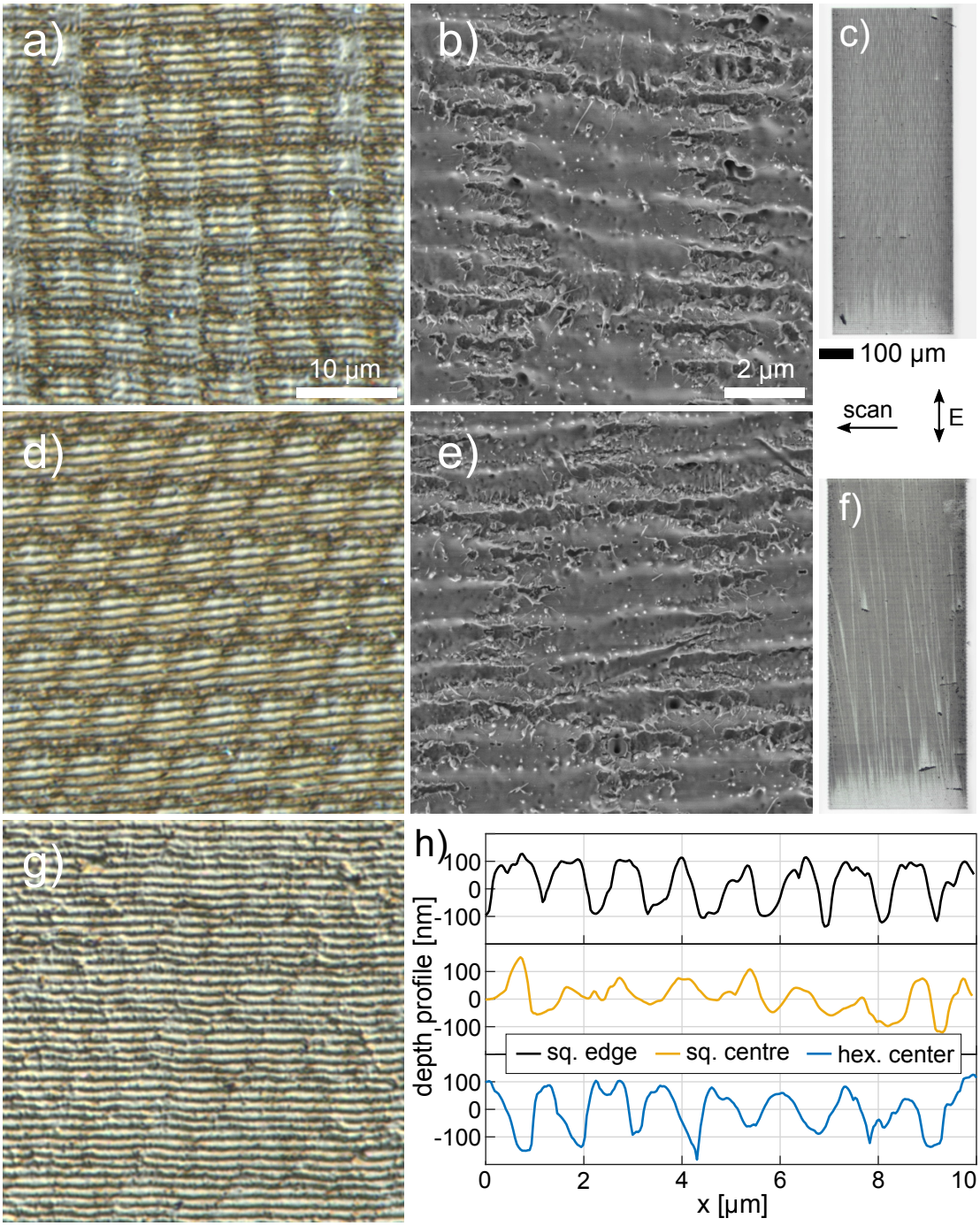


Figure 57: Demonstration of the FS structuring by LIPSS with Gaussian pulses. a, b, c) OM-DIC, SEM and OM images respectively of scanning in a square grid ($\omega_0 = 11.7$ $\mu$m, $\Psi = 76.4$ %, $F_{pk} = 4.82$ J/cm$^2$). d, e, f) OM-DIC, SEM and OM images respectively of scanning in a hexagonal grid ($\omega_0 = 11.7$ $\mu$m, $\Psi = 77.9$ %, $F_{pk} = 4.46$ J/cm$^2$). g) the structures in d) with a coating. h) AFM vertical profiles from square (sq.) and hexagonal (hex.) patterns.

# 4 Results and discussion: LIPSS and beam shaping attempts

Laser-material processing is often conducted with spatially Gaussian beam, as this is a fundamental laser mode. However, Gaussian energy distribution may not be ideal for all applications. When using a spatially shaped beam (flat-top, doughnut, etc.), higher control of position and amount of deposited energy is possible. This applies also for formation of LIPSS, which will be studied in the following sections by using a flat-top beam, and linearly focused Gaussian beam. Additionally, an effect of the Gaussian beam spot size on the LIPSS regularity is investigated as well as a short section on nanostructure fabrication by a doughnut beam is included.

## 4.1 Si nanostructures by a doughnut beam

Radially and azimuthally polarized doughnut-shaped beam with zero orbital momentum generated by an S-waveplate was used in our paper [148] focused on monocrystalline silicon surface structuring. By varying laser pulse energy and a pulse number, highly reproducible tubular (Fig. 58b) and needle-like structures (Fig. 58c) of height up to $\sim 2\,\mu$m (N = 8) were produced after focusing the Astrella laser beam by a 10× 0.12 NA microscope objective. However, typical height of the single-pulse needle structures was relatively small $\sim 0.6\,\mu$m at the structure width of $\sim 1\,\mu$m. It appears that usage of ultra-short pulses (< 100 fs) is crucial for highly reproducible fabrication of the tubular structures.

Possible explanation of the formation process was proposed as follows. Molten, non-ablated material in a ring shape is pushed by a recoil pressure of the ablation plume. The material moves both outwards and importantly inwards above the non-molten material, where it solidifies and forms extruded rims. The central tubular structure can be increased in height by increasing number of applied pulses. Eventually, with increasing pulse energy, such tubular structure is closed on the top, presumably forming a hollow core structure. Tubular and microneedle structures have an appropriate size for manipulation of processes at the cell interfaces and can find applications in targeted drug intracellular delivery or micro/electromechanical, photovoltaic and photonic devices.

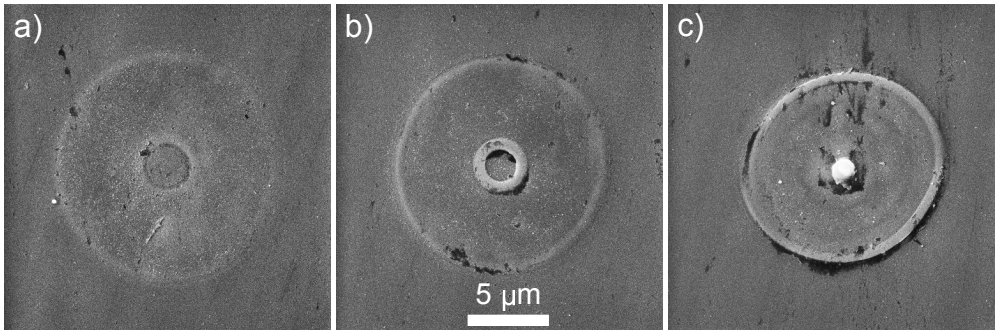


Figure 58: Irradiation spots on silicon by a doughnut-shaped laser pulses with pulse energies a) 0.67 $\mu$J, b) 1.02 $\mu$J and c) 1.26 $\mu$J. $\omega_0 = 2.6\,\mu$m.

## 4.2 Spot size effect

Variation of the Gaussian beam spot size is probably the simplest beam-shaping method, yet it may have an effect on the LIPSS regularity. So far, its effect was studied in detail on metals. Regularity of the LIPSS on metals was linked with a decay length of the surface electromagnetic waves (SEW), including surface plasmon polaritons (SPP) [77]. SEW, initiated by multiple distant surface scattering centers, can interact and lose their initial coherence properties. However, for rapidly decaying SEW, their interaction is reduced. This scenario would enable highly regular LIPSS structuring with relatively large spot sizes (e.g. 34 $\mu$m, steel [139] or 80 $\mu$m, Cr film [78]). Additionally, decoherence of the structures by parallel seeding should be suppressed by choosing a small beam spot size. It is suggested that scanning by a laser beam with size limited to $\lesssim 10$ wavelengths, coherence of the excited surface waves can be preserved more easily. Sequential creation of the nanostructures then enables formation of extremely uniform patterns, as was demonstrated by oxidation LIPSS on titanium [97].

A question remains, if the above conclusions transfer also to semiconductors. It is known, that SPPs can be generated on silicon, but only for a specific fluence window [52](0.7 – 5 J/cm$^2$, for 100 fs, 800 nm), which does not cover all the range, where LIPSS on Si can be created. Therefore, in the following experiment, a detailed investigation of the LIPSS formation was performed to verify, if similar significant effect of the Gaussian spot size on the Si LIPSS regularity exists.

To obtain sufficient data, three full parametric scans in the fluence–overlap space (with steps of 50 mJ/cm$^2$ and 3.3 %, Fig. 38 and similar) were performed. Each scan used a different spot size of 12.6, 22.2 or 43.0 $\mu$m. The spot size was adjusted with different focusing lenses with focal distances of 35, 75 and 150 mm respectively. Resulting effect of the spot size on the produced structures was evaluated in two ways.

First, parameters of the scans with smooth, low overlap, ablative LIPSS were identified and this parametric region was detailed by fitting an empirical parabolic range defined by Eq. 33. Figure 59a shows the resulting ranges of smooth ablative LIPSS. It can be seen that the ranges occupy almost the same parametric space and no clear trend is visible. Therefore, the second graph, showing only the width of these regions, gives a clearer picture. It seems, the smaller spot size is slightly more beneficial for fabrication of the smooth ablative LIPSS. However, it should be considered that visual evaluation of the surface structures is to some extent subjective and that steps in the overlap were 3.3 %, while the error of the presented data can be estimated to be approx. $\pm$ 2 %. That means, the first evaluation method shows no significant effect of the spot size variation from 12.5 to 43.1 $\mu$m in the parametric range, where the smooth LIPSS are fabricated.

The other approach of the data evaluation was by directly analyzing regularity of the LIPSS by the dispersion in the LIPSS orientation angle (DLOA, see Appendix B). Figure 60 shows the calculated DLOA maps. By marking a boundary for the DLOA = 10, three separate regions in the parametric space are found: low overlap ablative, high overlap ablative and amorphization based LIPSS. Size of these areas is clearly diminishing with an increasing spot size, in particular the region of low overlap ablative LIPSS. However, as in the previous approach, the estimated evaluation error of $\sim$1–1.5° is close to the observed variation. Therefore, the DLOA variation provides a strong hint on the spot

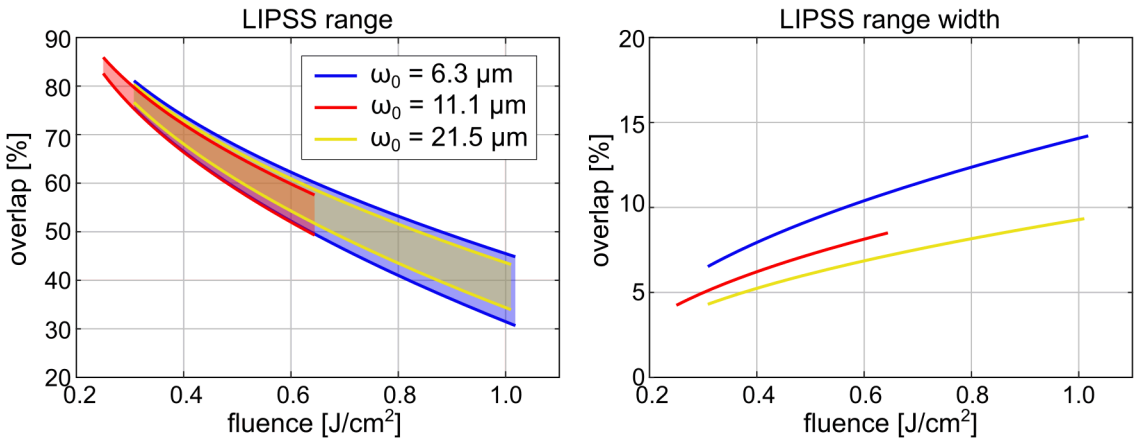


Figure 59: Overlap range and a width of this range, where the smooth ablative LIPSS are fabricated for 2D scanning with three different beam spot sizes.

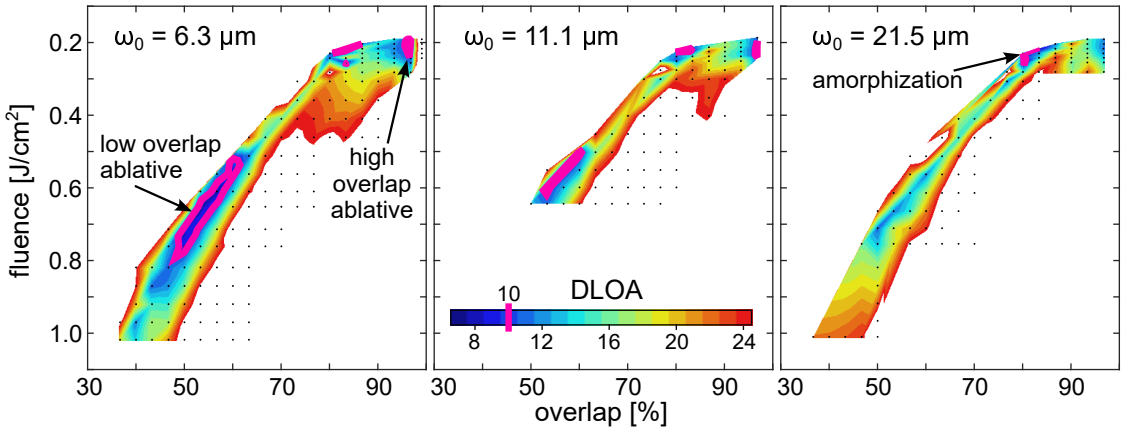


Figure 60: DLOA maps of the LSFL on Si, fabricated with three different laser spot sizes.

size effect existence, but it does not give a definite proof and further investigation is needed. A publication is being prepared on these experimental observations.

In conclusion, Gaussian beam spot size seems to have an effect on the range of the scanning parameters and regularity of the fabricated LIPSS on Si in a way, that smaller spot size produces more regular structures in a slightly extended range. But these effects on silicon are not significant for a spot size change within the range of 12.5 to 43.1 $\mu$m. Therefore, it seems reasonable to use a larger spot size to increase fabrication speed of the LIPSS in the soft ablation regime if a small decrease of the regularity can be accepted. On the other hand, in a case of the highly regular amorphization LSFL on Si, it was found that the smaller spot size leads to a better structure uniformity.

## 4.3 Beam shaping in scanning on Si and $SiO_2$

Another investigated beam shape was a square flat-top profile. Constant intensity over the beam profile have a positive effect on homogeneity of processing, well defined edges of the processed area, reduced collateral material damage and increased efficiency of the pulse energy utilization. This was demonstrated in static irradiation on well defined removal of thin surface layers [135], LIPSS covered areas [136] and increased energy efficiency in fabrication of spike structures [177]. In 1D scanning of the LIPSS, well defined edges of the structured area can be achieved [47], however, these edges may cause stitching defects in 2D scanning at low overlaps. Fabrication of large areas of uniform and regular LSFL was demonstrated on metals [139], but pulse overlap had to remain above ∼80 % for the structures to retain high regularity. Such a high overlap needed, which was also observed experimentally later, actually negate the inherent benefit, against the Gaussian beam, of fast low-overlap scanning.

In the following text, silicon and fused silica scanning with the square flat-top beam is investigated. Results are compared with the Gaussian beam scanning from previous sections to find out, if it provides an advantage for a large area LIPSS formation. In this

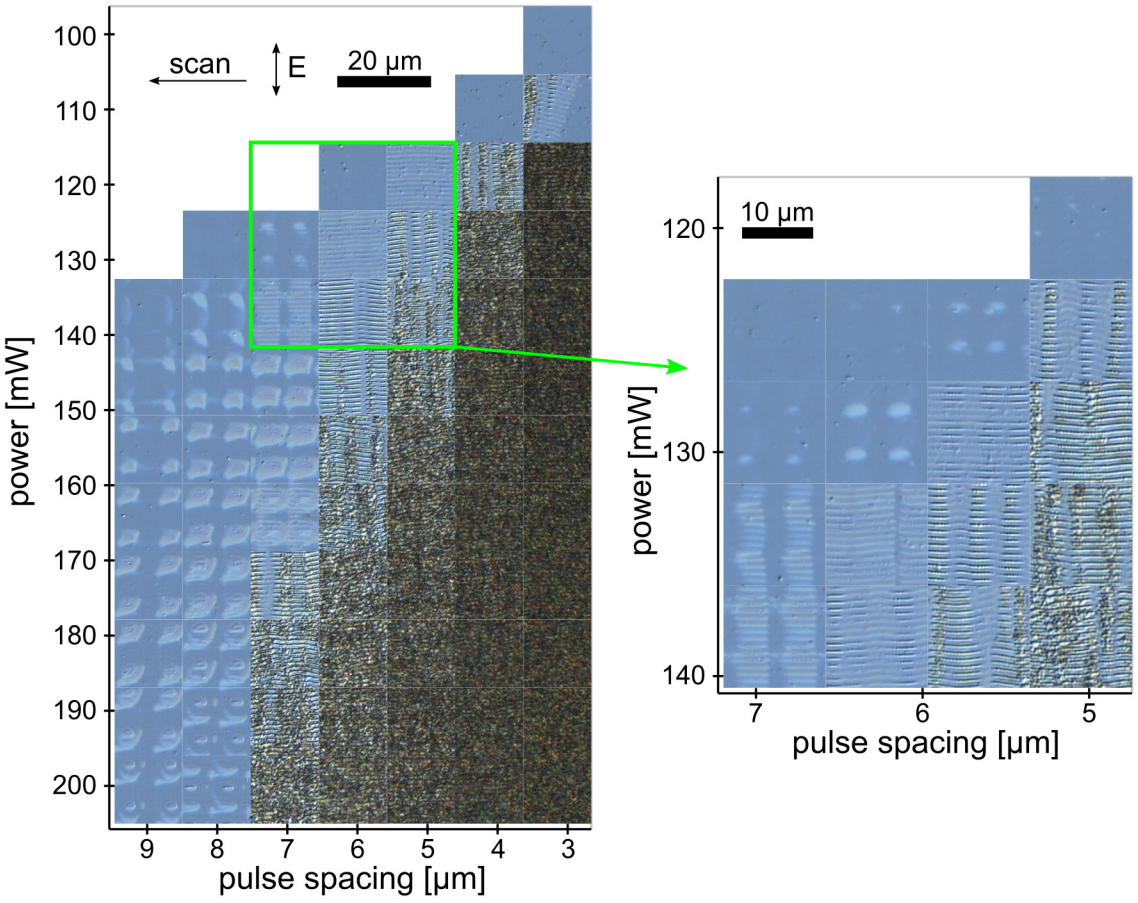


Figure 61: An OM-DIC map of the LIPSS scanning on silicon in a pulse spacing ($d_x = d_y$) × power (at 200 kHz) parametric space with a flat-top beam. Laser parameters: $\lambda$ = 1030 nm, $\tau$ = 265 fs, $f_{\mathrm{rep}}$ = 3 kHz.

experiment, commercial $x$-$y$-$z$ linear stage microprocessing setup was used to scan the samples with a 1030 nm laser beam. The beam was shaped by the FSB shaping element generating a square-like beam in the focal plane.

Figure 61 shows a parametric map of pulse spacing × power (at 200 kHz) of structures produced on silicon. Pulse repetition rate of 3 kHz was used for scanning. A lens with a focal distance of 5 cm would produce $2\omega_0 \approx 24\,\mu$m spot size for a Gaussian beam. It seems, a size of the shaped beam 1.25× bigger than that provides approximately correct values of overlap and fluence. In the main map (Fig. 38), these correspond to ranges $\Psi_x = \Psi_y$ =70–90 % and $F$ = 0.17–0.34 J/cm$^2$. The scanned parametric regions in Fig. 61 therefore correspond to the region of highly regular amorphous LSFL in Fig. 38. However, no increased rate of highly regular structure formation, in comparison with the Gaussian scanning, is observed here. Therefore, the flat-top beam unexpectedly does not provide a benefit of higher regularity, nor ease of LSFL generation in the investigated parametric range. Maybe the structures generated in a soft ablation regime for higher fluence and smaller overlaps could be of better quality, but already in this scan at higher powers, localized damages in the positions of overlapping square corners can be seen. For larger fluences localized ablation is expected to form in these positions, damaging the structure regularity.

It has to be noted that the shaped beam was able to produce damaged areas close to a square in $N$-on-1 irradiation. But from observing LSFL formation inside these areas, despite significant beam alignment effort, it was evident that, the fluence distribution was not precisely flat. Such deviations from an ideal flat-top profile may have been caused by wrong focusing conditions or mismatch of the input beam from an exact Gaussian profile.

Further, similar scans were repeated also on fused silica in the same scanning setup. Figure 62 shows the obtained maps. In the map in Fig. 62a we can see that with decreasing pulse spacing LSFL are created in the pulse centers. However, simultaneously when the LSFL are developed, strong surface ablation is already present between the scanning lines. Therefore, the second scan in Fig. 62b was scanned with increased scan line spacing to 1.15× the pulse in-line spacing. This have caused a shift of the structure generation towards smaller in-line overlaps, but did not solve the excessive ablation. The only solution to this problem was to decrease the fluence and increase pulse overlaps. In this regime, structures very similar to the ones fabricated with a Gaussian beam were produced (Fig. 57). Additionally, relatively uniform and regular structures were obtained for high overlaps ($d_x$ = 4.7 $\mu$m, 580 mW), but due to increased ablation, the structures were not smooth. Therefore, again no benefit in using the shaped beam was found.

On the contrary, a problem of scattering on the previous crater edges was emphasized. Such sharp oriented edges then strongly affect LSFL structures generated in its vicinity [79, 80]. Figure 63 shows three selected structures from the Fig. 62 with increasing overlaps. In Fig. 63a, formation of 2-3 LSFL vertical periods, parallel to the polarization, by scattering on the edge of a previous pulse, is clearly visible. Additionally, Fig. 63d shows an AFM topography scan of the scattering structures. Structure peak-to-peak height exceeding 200 nm was measured (Fig. 63e). Scattering from the pulse edge remains visible also for a larger pulse overlap in Fig. 63b. For even larger overlap and fluence close to a modification threshold, scattering from the vertical edges is no longer present, but the edges are still visible as vertical cuts in the LSFL. In this regime of high overlap and

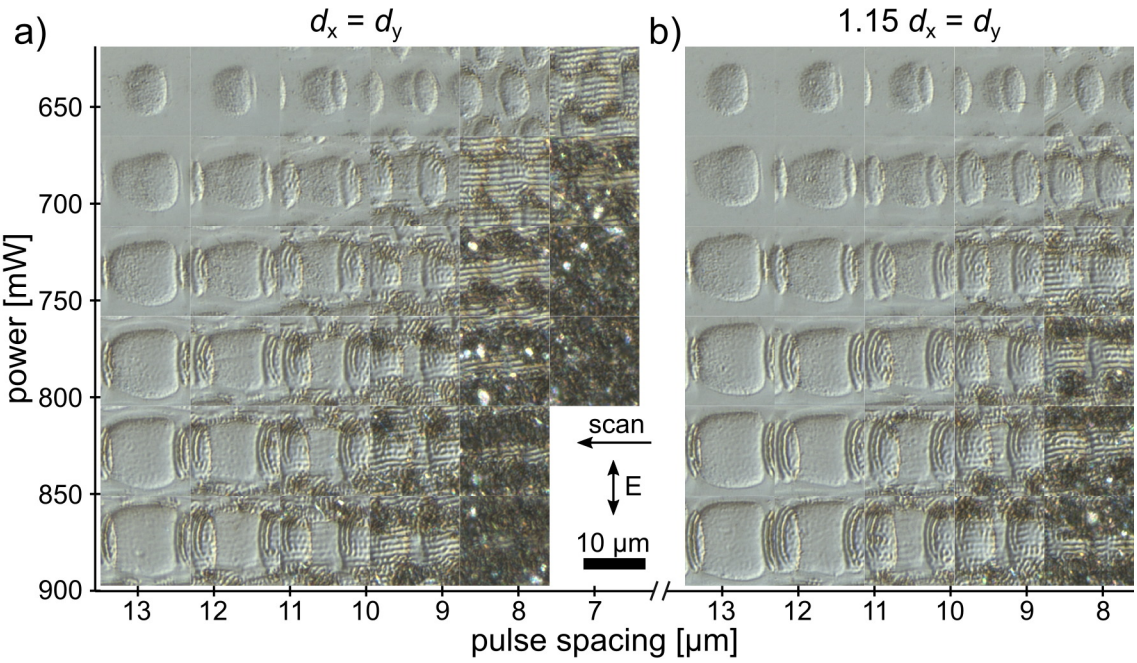


Figure 62: An OM-DIC map of the LIPSS scanning on fused silica in a pulse spacing × power (at 50 kHz) parametric space with a flat-top beam. Processing parameters: $\lambda = 1030$ nm, $\tau = 270$ fs, $f_{\text{rep}} = 1.7$ kHz, hexagonal arrangement.

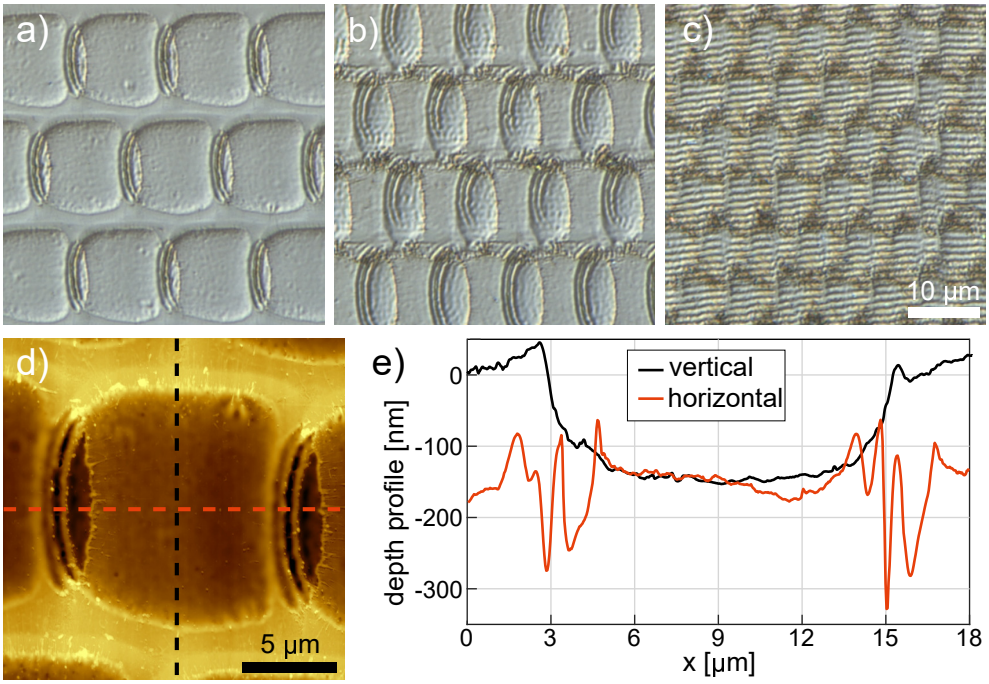


Figure 63: Diffraction on the crater edges on fused silica for parameters a) 870 mW, $d_x = 12.9$ $\mu$m, $d_y = 14.8$ $\mu$m, b) 830 mW, $d_x = 10.5$ $\mu$m, $d_y = 12.1$ $\mu$m and c) 640 mW, $d_x = d_y = 7.0$ $\mu$m. d) An AFM height image from a). e) Height profiles along the indicated lines in d). Vertical polarization, horizontal scanning, hexagonal pulse alignment.

fluence close to modification threshold, material processing has increased dependency on small variations of the beam profile. However, perfect flatness of the beam profile, as was stated before, is problematic. Therefore, this gives another argument against using of the flat-top for dielectric structuring.

## 4.4 Cylindrical lens focusing

The last investigated beam shaping method was focusing of a Gaussian beam by a cylindrical lens, which results in an elliptical focal spot with high eccentricity. Expected benefits of such focal beam shape are increased structuring speed together with enhanced LIPSS regularity.

Surface structuring speed scales with on the beam spot size multiplied by the laser repetition rate. Therefore, for constant repetition rate, if the beam radius in the minor axis is 10 $\mu$m and 5 mm in the non-focused major axis, fabrication efficiency is increased 500 times in comparison with a spherical lens focusing. In combination with high average power lasers in HiLASE, e.g. Perla-B, surface structuring speed above 10 cm$^2$/s should be possible. This is already a speed, that can find industrial applications.

Achievable regularity and uniformity of the LSFL fabricated by cylindrical lens scanning is often superior to the structures created by a spherical lens focusing. This is, perhaps, due to significant suppression of the scattering from non-straight edges of previous irradiation pulses. With a cylindrical lens focusing, highly periodic structures were produced in a single step [40, 94, 178, 179]. An option to use a two beam interference to further shape the beam into a series of line foci with even higher aspect ratios was also reported [180]. On silicon, however, the best results in terms of regularity were observed for two step processing. First, highly regular amorphous LSFL (e.g. Fig. 44c or Fig. 67d) are produced at low fluence scanning. These, practically flat structures, are subsequently wet etched to create topographical variation [181, 182]. Depth of the final LSFL can be adjusted by varying the etching conditions or by repeating the process.

In the following, two sets of results with cylindrical lens scanning are presented. The first attempt for LIPSS fabrication on silicon was with the high-power Perla-B laser system (1030 nm, 1400 fs, 10 kHz). An $x$-$y$-$z$ linear stage scanning setup (Fig. 20) was used for sample movement under static focus. The laser beam was focused by a $f = 10$ cm cylindrical lens, resulting in a $1/e^2$ focal spot of $23.8\times \sim 7200\,\mu$m.

Unfortunately, this set of experiments suffered from a yet unclear effect, that the LSFL are created and further propagate under a discreet angle with respect to the laser polarization. Figure 64a demonstrate an extreme case of such behavior. Plus and minus the specific angle at which the LSFL are extended by scanning from right to left is clearly visible. The dark central area is a result of increased ablation, but at the periphery of the scanned area, regions with highly regular LSFL can be typically found (Fig. 64c). Changing the irradiation conditions so that the LSFL are observed already along the center of the scanned area (Fig. 64b), still shows some lateral inhomogeneity of the fabricated structures. Typically, three regions are observed. The central region contains pronounced ablative LSFL of low quality. The low quality is most probably due to coexistence of competitive LSFL under the two propagation angles, which renders resulting orientation of the structures poorly defined. Such LSFL interference may also explain the intriguing

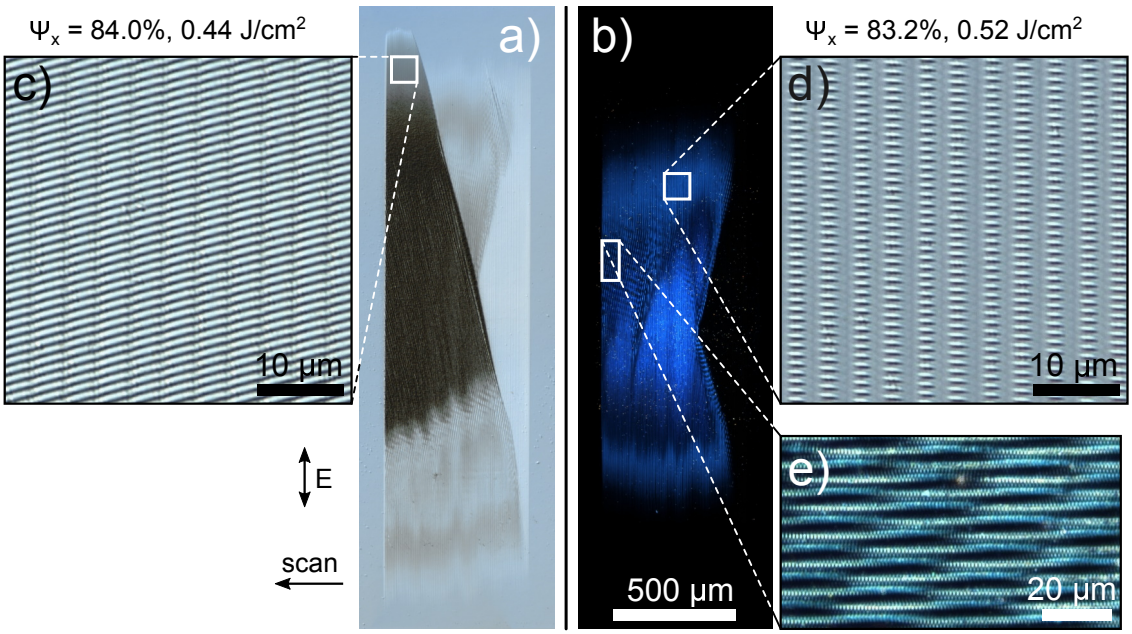


Figure 64: Surface scanning by a Gaussian beam focused by a cylindrical lens. a) (OM-DIC) a particular case of strong nonuniformity of the irradiated area. b) (OM-DF) a typical case of a structured area with unordered periodic structures in the scan center and ordered structures at the scan periphery. c), d), e) magnified sections from a) and b). Image e) (OM-DF) is rotated by 90°.

pattern of an interleaved structure of LSFL columns (Fig. 64e). Straight LSFL columns in this case form the outer two regions on the scanned area (Fig. 64c). The dark intermediate regions (i.e. no diffracting periodic structures) between the central and outer LSFL regions resembles the gap in the LIPSS parametric space mapping in Fig. 38f. We assume, it is of the same origin.

Fabrication of large area, uniform and regular LSFL across the full width of the focal spot was achieved only for the discontinuous lines of LIPSS as in the Fig. 64d. Larger areas of continuous and regular LSFL were observed only away from the laser spot center. Figure 65 demonstrates, how such LSFL are created, when the pulse overlap is changing.

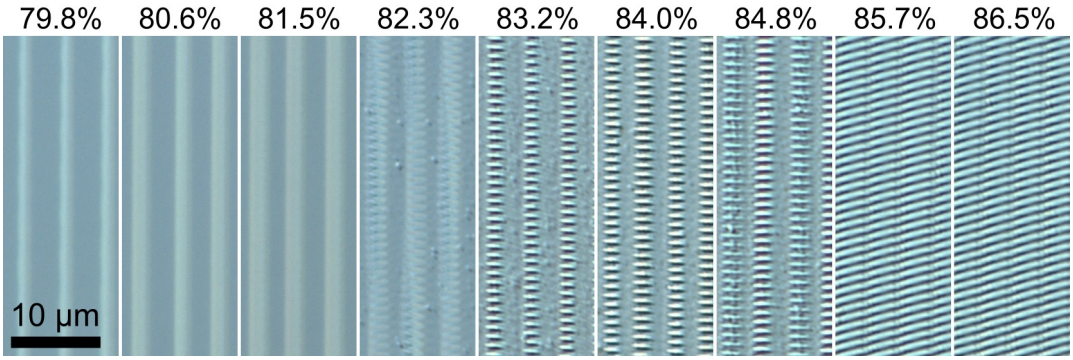


Figure 65: Evolution of the surface structures with the pulse overlap in a cylindrical lens focusing regime. Scanning parameters: horizontal scanning, vertical polarization, $F = 0.42$ J/cm$^2$.

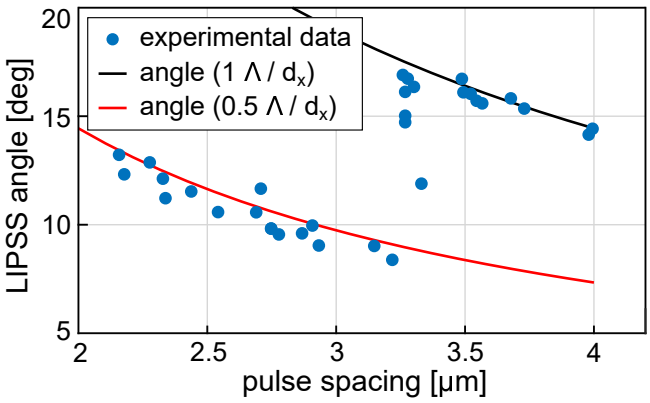


Figure 66: Dependency of the LIPSS orientation angle with respect to the vertical polarization on pulse spacing in a cylindrical lens focusing regime.

For larger pulse spacing (79 – 81.5 %), only amorphization from individual pulses is visible. Increasing the overlap beyond ∼ 82 % leads to creation of the LSFL lines, which are joined into continuous structuring for even larger overlap. Interestingly, this suggests to fabricate periodic amorphous structures on silicon in a simpler way where, under tight focusing, each pulse will create directly one period of the pattern.

The orientation angle of the LSFL mentioned above and visible in Fig. 64 and 65 is not constant, but depends on the pulse spacing. Figure 66 shows this trend for off-center LSFL scanned at various fluences (∼0.45 – 0.52 J/cm$^2$). This intriguing bi-stable behavior shows, that the LSFL angle, with respect to the vertical polarization, is equal to an angle of half the LSFL period ($\Lambda \approx 1.02\,\mu$m) against the pulse spacing $d_x$ for spacing less than $\sim 3.25\,\mu$m and an angle of one LSFL period against the pulse spacing for larger spacing. Mathematical expressions $\theta_1 = \arctan(\Lambda/d_x)$ and $\theta_{0.5} = \arctan(\Lambda/2d_x)$ are used to plot the solid line curves in the figure. In the transitional region of pulse spacing, coexistence of the LSFL domains with both orientations is observed. Related effect was already observed for the LIPSS stripes scanning (Section 3.3.2). There, adjacent stripes of LSFL were aligned in phase for larger stripe spacing, but aligned in anti-phase for stripe doubling, where spacing of the stripes was tighter. An attempt was made to evaluate the LSFL angle also for structures scanned by a spherical lens from the previous sections. It seems, the $\theta_1$ angle is an upper border of the angle also in other LSFL scanning cases. However, mostly due to substantial evaluation errors of low regularity LSFL, the sharp transition between the angles was not observed elsewhere.

As can be seen in Fig. 64a, the LSFL angle is mirrored on the sides of the scanned area. This may suggest nonuniformity of the laser beam along its major axis, maybe a wavefront curvature. Additionally, one would assume the scan in Fig. 64b was scanned for lower fluence than the one in Fig. 64a, which is not the case. These scans originate from two separate samples, which raises a suspicion that the precise focal position or the beam size was not stable. Due to spatial restrictions in the laboratory, the scanning setup was located several meters away from the laser, what may have caused these adverse effects. Therefore, to verify the cause of these problems and improve the results, the cylindrical lens scanning experiment was repeated in a different laboratory, with the Pharos laser (1030 nm, 260 fs, 10 kHz) and the commercial microprocessing setup (Fig. 21).

The microprocessing setup, with a threaded mount for an objective, originally did not have means for processing with a cylindrical lens. Therefore, I designed a lens adapter, which was 3D printed and attached to the z-stage of the setup. The cylindrical lens with a focal distance of 40 mm created a $\sim 4800 \times 13.4\,\mu$m $1/e^2$ focal spot.

Figure 67 demonstrate selected results, with horizontal scanning and major beam spot axis along the vertical direction. Irradiation parameters are given in the figure caption. Values of the fluence may have a larger error due to lower precision in the beam size measurement along the major axis. In the Fig. 67a, scanning was along the polarization. Highly oriented structures can be easily produced, but their period variation with the pulse spacing period is often clearly visible. Figures 67b,c show some of the possible outcomes of scanning with the polarization perpendicular to the scanning direction. In this case, the LSFL are formed in vertical columns, where the periods of the adjacent columns are in antiphase. Two (Fig. 67b), three, four and five (Fig. 67c) such columns per pulse spacing were observed. Similarly to the previous experiment, also here the scanned areas are not fully homogeneous in the lateral (vertical) direction, as the fluence naturally decreases along the beam profile. When there are ablative LSFL on the optical axis, it is typical to observe highly regular amorphous LSFL (Fig. 67d) at the edges of the scanned area. For precisely selected parameters, it is expected to produce these structures also along the center of the scanning beam.

Insets in the Fig. 67a,b,c are AFM height scans of the corresponding structures. Height profiles along the indicated dashed lines are then plotted in Fig. 67e. The height variation in most of the structures is $\sim$ 100 nm, except particular part of the structures in Fig. 67c, where topographical modulation exceeds 200 nm.

Explanation of the unique patterns shown in Fig. 67b,c seems to correlate with the problematic LSFL extension under specific angles in the previous experiment, even though, this effect is no longer directly visible in the scanned regions. Figure 67f shows a spatial spectra of the Fig. 67b. Three main spatial frequencies are clearly visible. The two spatial frequencies with a $|k|$ vector of 1 $\mu$m$^{-1}$ are tilted from the vertical direction (direction of polarization) by $\pm 16.1°$. This angles match perfectly the trend from Fig. 66. Based on the first experiment (Fig. 64) with LSFL on the lateral edges, under opposite angles, a hypothesis is that the periodic structures observed in Fig. 67b are an interference pattern of the two independent LSFL orientations.

In the case of finer structure, e.g. five columns per pulse spacing in Fig. 67c, the spatial spectra (Fig. 67g) is slightly modified. The three main spatial components as in Fig. 67f are still visible, but additional points, suggesting a convolution with the pulse spacing vector, are present.

In addition to the laser fluence, overlap and polarization orientation, effect of the repetition rate and misfocusing was investigated. The effect of the repetition rate was tested only for 1 and 10 kHz, due to hardware restrictions. For power 1500 mW ($\sim$ 0.59 J/cm$^2$), overlaps in the range of 53.3 – 70.0 % and scanning along the polarization, a very small difference can be seen. The structures scanned at 1 kHz at given overlaps are comparable with the ones scanned at 10 kHz at overlaps $\sim$ 0.5 % smaller.

Further, the effect of focusing was investigated to verify if misfocusing can cause strong processing nonuniformity as was observed in the first experiment. Several processed areas, with four powers in a range of 1400 – 1900 mW ($\sim$0.55 – 0.75 J/cm$^2$) and overlaps in

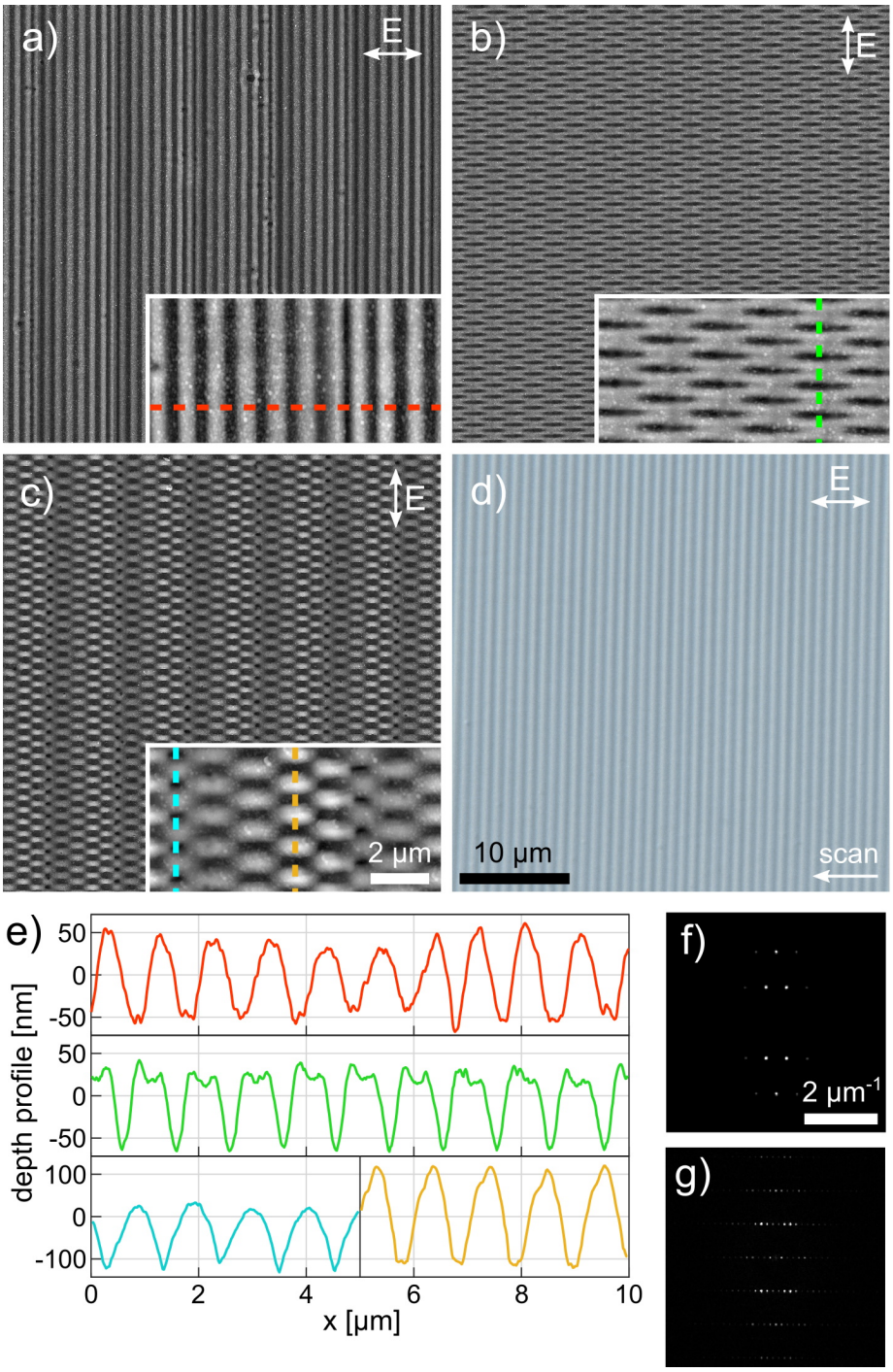


Figure 67: Silicon surface scanned by a Gaussian beam focused by a cylindrical lens. a), b) and c) SEM images measured at the beam center with corresponding AFM height scans. d) (OM-DIC) highly-regular amorphization LSFL. e) AFM height profiles along the dashed lines indicated in a), b) and c). Zero level does not match the initial surface position. f) and g) FFTs of the structures in b) and c) respectively. Irradiation parameters: 10 kHz, $\omega_{0,x} = 6.73\ \mu$m, $\omega_{0,y} \approx 2400\,\mu$m, a) 1700 mW ($\sim 0.67$ J/cm$^2$), 46.7 %, b) 900 mW ($\sim 0.36$ J/cm$^2$), 86.7 %, c) 1700 mW ($\sim 0.67$ J/cm$^2$), 53 %, d) 900 mW ($<0.36$ J/cm$^2$, side of the scanned area), 90.0 %.

a range of 37 – 73 %, were compared, when scanned in focus and one Rayleigh length (120 $\mu$m) above and below the focus. Fluence was not adjusted for the increased spot size on the sample, when the beam was out of the focus. Resulting structures in all focusing conditions were fairly similar with no fundamental changes, contrary to the findings of San-Blas *et.al.* [113]. In fact, some scans, with sample positioned after the focus, showed slightly higher uniformity and less pronounced pulse spacing. In most cases, generated structures were similar, if a shift of the pulse overlap by up to 5 % in the comparison was allowed. The only difference was the scan at 1400 mW ($\sim$0.55 J/cm$^2$), where for positioning the sample before the focus, regularity of the structures was completely destroyed. In general, it was observed that positioning the sample after the focus by one Rayleigh range did not induce any adverse effects, while positioning the sample before the focus had an effect similar to small decrease in fluence. However, it has to be noted that such asymmetry around the focal position was also observed during an initial search for the focal position. Here, size variation of the modified surface along the major axis as a function of the focal position was also asymmetric, showing a sharper decrease when the sample was moved before the focus. Observed effect of the structure change can be therefore rather attributed to a lens aberration than to a specific property of the laser-material interaction.

# 5 Results and discussion: Multiphoton modification in the mid-IR

Ultra-short laser pulses are a beneficial tool for processing of optical and semiconductor materials. An action of the commonly used conventional NIR (800 and 1030 nm) ultra-short laser pulses on silicon is limited to surface modification, since the material is opaque in this spectral region. However, it has been demonstrated that by tightly focusing mid-IR ultra-short laser pulses inside the silicon, local nonlinear (NL) optical absorption can be initiated [183, 184]. The laser-generated free carriers lead to optical breakdown and can induce volumetric modification [185] for controlled manufacturing of structures.

Use of longer wavelengths for volumetric modification of narrow bandgap materials is beneficial in terms of the possibility to use multiphoton ionization (MPI) as a free electron generation mechanism. Higher order of the nonlinearity relates to higher localization of the deposited energy. On the other hand, depending on the material and irradiation conditions, other excitation mechanisms such as indirect absorption or tunneling may play a significant role. Unfortunately, MPI cannot guarantee a highly localized material volumetric modification in all cases, because of competition with other nonlinear volumetric effects such as plasma scattering and plasma density self-limitation [186, 187].

Moreover, laser beam focusing inside the material bulk is accompanied by self-focusing and other NL processes along the beam propagation. This poses difficulties in determination of the exact intensity, fluence and depth at which the absorption occurs. To avoid effects of volumetric nonlinearities and parametric uncertainity, we studied the NL absorption behavior by placing a focal spot on the material surface, in order to determine laser intensities corresponding to surface modification threshold. In this section, first results on material modification and NL absorption for Si using 2 ps laser pulses at wavelengths of 1.6 and 3.15 $\mu$m are presented. Similar measurements were carried out also for germanium. However, the available laser power was not sufficient to obtain relevant data.

Fig. 68 illustrates an optical setup used for this experiment. The laser source is an experimental 1030 nm Perla-C (Hilase) laser with a tunable OPA downconversion into the

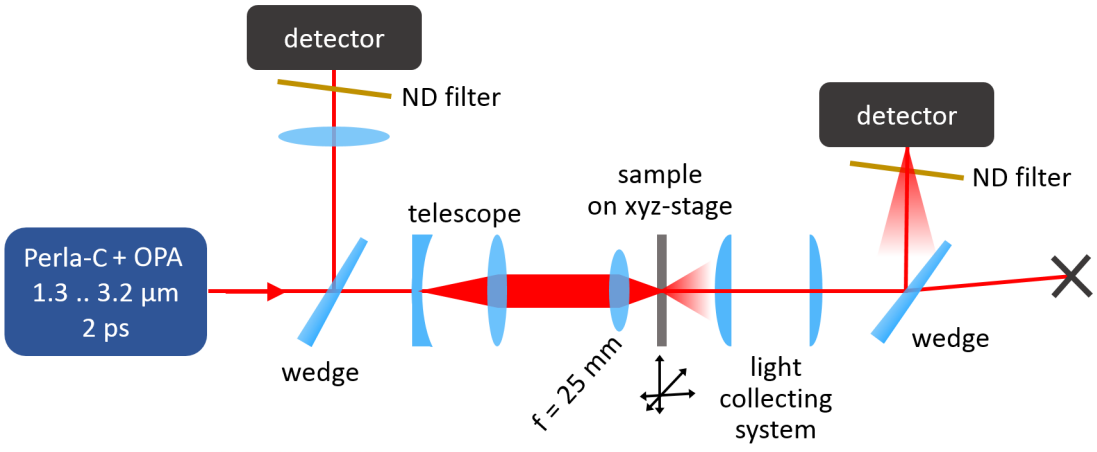


Figure 68: Optical setup for semiconductor transmission measurement in the mid-IR wavelength range.

mid-IR range. It was operated at 2 ps pulses, tunable output wavelength from 1.5 to 3.2 $\mu$m and a repetition rate of 89 kHz. The pulse energy was controlled with a combination of a halfwave plate and a Si-based Brewster polarizer (not shown). A part of the beam was reflected to a reference detector, whose signal was calibrated before every measurement. The calibration was later used for compensation of pulse energy fluctuations. After the sampling wedge, the main beam was expanded and focused by a short focal length lens onto the sample surface. This resulted in beam spot size diameters of 21 and 28 $\mu$m for 1.6 and 3.15 $\mu$m wavelengths respectively. The sample was mounted on a tilt adjustable mount connected to a partially computer controlled $x$-$y$-$z$ stage. Light transmitted through the sample was collected and focused into the second detector. This detector, similarly to the reference one was calibrated before every measurement to account for the actual system adjustment. The first adjustment of the system to the optical axis was done with an alignment laser and later with a help of a bolometric camera.

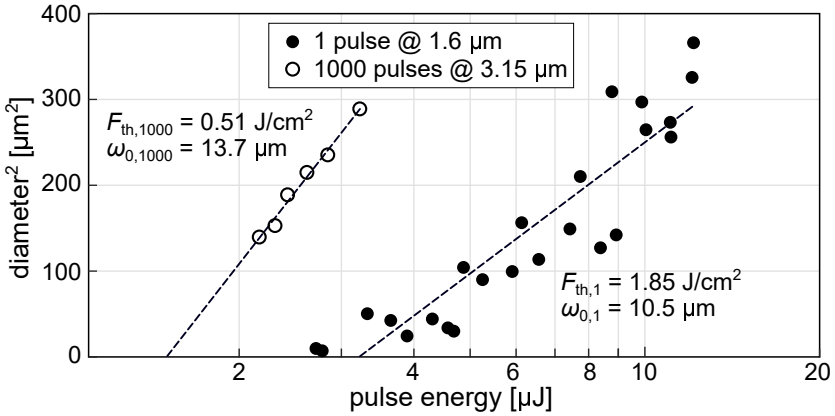


Figure 69: Single pulse damage threshold of silicon for 2 ps, 1.6 $\mu$m and 1000 pulse burst damage threshold for 2 ps, 3.15 $\mu$m.

Fig. 69 shows results of the damage threshold measurements for 1.6 and 3.15 $\mu$m wavelengths. For the 3.15 $\mu$m, the pulse energy was not sufficient to induce a single pulse damage. Therefore, bursts of 1000 pulses were used for each laser pulse energy to create laser-induced modification on the sample surface. However, for proper comparison of the single pulse thresholds, an extrapolation method based on the incubation effect (Section 1.2.1) or another high power laser should be used.

Further, normalized transmittance and absorptance of double-side polished Si sample measured at 1.6 $\mu$m wavelength was examined. The normalized transmittance $T_n$ was obtained by dividing the measured transmission $T$ by a low power, linear region transmission $T_0$, i.e. $T_n = T/T_0$. The absorptance $A$ is then derived as $A = (1-T_n)$. Theoretically, for bandgap materials, the NL absorption should follow an exponential dependency on the laser intensity $I$ as $A \sim I^k$, where $k$ is an order of the multiphoton absorption. That means, in presence of the NL multiphoton absorption a semilogarithmic plot of $A(I)$ should be linear. However, deviation from this trend may exist due to presence of other effects such as tunneling [183].

Fig. 70 and Fig. 71 show normalized transmittance and absorption plots for Si measured at excitation wavelengths 1.6 and 3.15 $\mu$m respectively. The transmittance plot

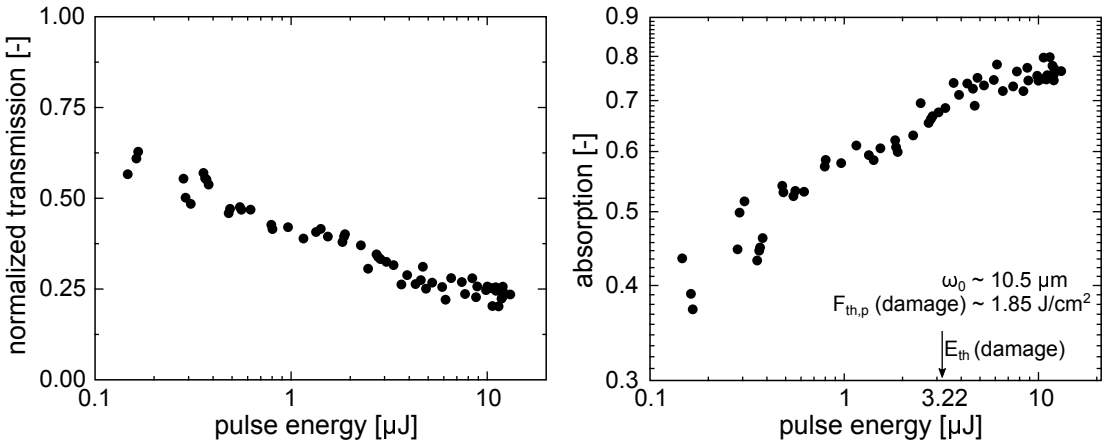


Figure 70: Normalized nonlinear transmittance $T_n$ of silicon for 2 ps, 1.6 $\mu$m pulses and corresponding calculated absorptance.

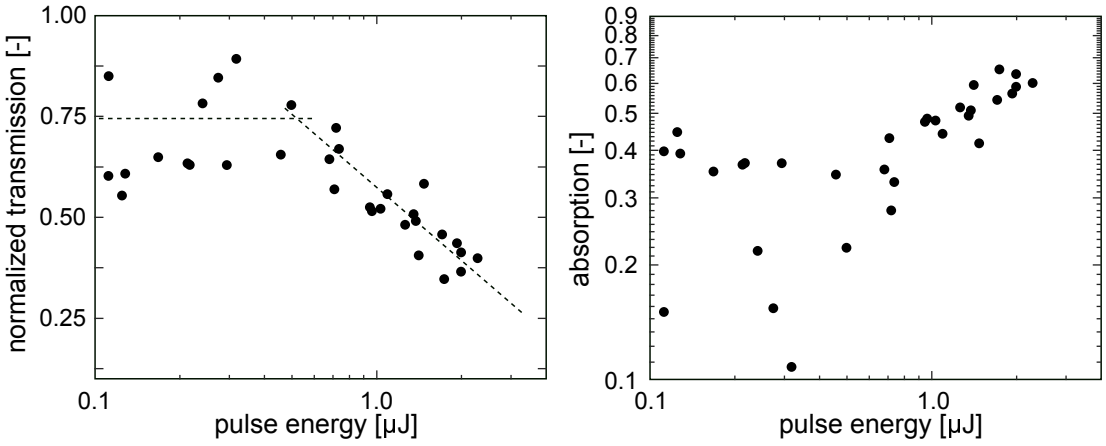


Figure 71: Normalized nonlinear transmittance $T_n$ of silicon for 2 ps, 3.2 $\mu$m pulses and corresponding calculated absorptance.

in Fig. 70 shows a continuous decline. It starts already from 0.1 $\mu$J pulse energy, what was the minimum adjustable measurable energy in our experimental setup. Theoretically, without any linear absorption one can expect a constant transmittance up to a certain pulse energy. For larger energies, with an onset of the NL absorption, transmittance will start to decrease. Starting from this energy, a logarithmic plot of $A(I)$ will show a linear behavior [183] and from a slope of this dependency we can estimate an order of the multiphoton absorption. Unfortunately, it was not possible to get this information from the experiment, as the logarithmic $A(I)$ plot is not exactly linear as expected (when only multiphoton absorption is expected). Moreover, deviations of the measured points are too large (see Fig. 71). Several reasons can be responsible for these errors. First, this behavior of the measurement can be attributed to instabilities of laser pulse energy together with beam shape changes and directional deviations due to thermal drift. But relatively long pulse duration (2 ps) also plays a significant role. Such long existence of the laser field within excited material may lead to an enhanced avalanche ionization and

domination of the tunneling mechanism.

The presented results contain significant uncertainity, what raises a question, to what extent they could be trusted. Therefore, additional experiments were planned with an OPA of the Astrela laser producing $\sim$ 100 fs mid-IR pulses. This should enable us to obtain more detailed data according to the model predictions. Unfortunately, due to time constraints and prioritization of other experiments, this experiment have not been done yet.

# 6 Conclusions and outlooks

Processing of bandgap materials with ultra-short laser pulses was investigated from an experimental point of view, with a particular focus on formation of regular laser-induced periodic surface structures (LIPSS).

In the Section 3, the experimental results obtained from irradiation with spatially Gaussian beam were presented. At the beginning, several experiments on material damage threshold (DT) are discussed. In spite of the apparent simplicity and known procedure in the laser processing community, it was possible to reveal the importance of several effects that point to fundamental aspects of the laser-matter interaction. It was indeed demonstrated that the single-pulse damage threshold of monocrystalline (100) silicon is dependent on the polarization orientation. A variation of more than 9 % was observed for 800 nm, 37 fs pulses. Further, damage and ablation thresholds were investigated in a double-pulse arrangement. Here, a 16 % increase in surface damage is observed, compared to a case of a single second harmonic pulse with double the energy, if the second harmonic pulse arrives within a window of 0 to 1 ps before the fundamental pulse. However, for other timing in the tested configuration (250 fs, 1030 and 515 nm, 4.5 $\mu$J, equal fluences), the bi-color irradiation performs less efficiently in material processing than more energetic single pulses. Further, material DT is affected by thin surface coatings. This was quantified in an experiment on silicon with a native and 300 nm thick artificial oxide layer [133], where the thick oxide layer increased the DT of the underlying silicon by 18 %. These investigations on silicon modification regimes without destruction of the oxide layer were later extended, when the same material was used to fabricate LIPSS on the Si surface under the $SiO_2$ layer. The periodic structure was replicated on the top of the oxide layer, where a graphene monolayer was deposited, either topographically, or by periodic modulation of the graphene doping level that allowed for its periodic functionalization [90]. Finally, investigation of the DT and crater morphology was also conducted on Kapton [129] and polystyrene. Elongation of the craters in the polarization direction and loss of the crater quality for ps pulses was reported. These morphological aspects can be of interest, for example, in order to control the process of periodic structuring of polystyrene Petri dishes for biological applications.

In Section 5, DT measurements and volumetric modification was also attempted on silicon and germanium in the midIR spectral range. However, instabilities in the used laser source, amplified by the nonlinear nature of the interaction processes, disabled us to reach novelty with these results. Further investigation would require a more stable source with larger pulse energy.

The main part of the results is focused on formation of the LIPSS, that has been experimentally studied on silicon and fused silica, for irradiation with fs and ps, Gaussian and beam-shaped (Section 4) pulses. For every set of these parameters, optimal laser processing conditions were determined, primarily by a parametric search in fluence–overlap space. Influence of several aspects on the LIPSS generation was investigated, such as an effect of the polarization orientation with respect to the scanning direction. It was revealed that for Gaussian beam raster scanning, polarization oriented under 45° with respect to the scanning direction towards the pristine surface maximizes positive feedback. In addition, an effect of the scanning mode, i.e. single direction with perpendicular

polarization, results in a slight tilt of the LIPSS towards the scan direction. It was also revealed that the beam spot size affects regularity of the LIPSS in a way that smaller spot size seems to generate structures of higher regularity.

Along with these experiments, it was repeatedly observed that the process of obtaining regular LIPSS is not straightforward. One of the striking points in the search for regularity is the precision required in both the scanning system and the pulse fluence, especially on dielectrics. This underlines the need for small steps in the processing parameters as well as detailed characterization of the focus, damage threshold and laser spot size. The latter stresses the importance of several aspects in the spot size and damage threshold effects mentioned above. Further, numerous problems that were encountered while fabricating LIPSS are summarized in Appendix C. Nonetheless, large area, regular and uniform LIPSS were achieved on both silicon (Fig. 44 and Fig. 67) and fused silica (Fig. 57). Additionally, specific processing conditions were discovered, where LIPSS are formed in regular stripes [65] with unstructured separating regions. LIPSS within the adjacent stripes are either in phase or in antiphase. The formation mechanism was attributed to a specific regime of surface amorphization, which supports LIPSS generation in between the irradiation pulses.

On fused silica, an effect of periodic LIPSS orientation change within a single scan was observed. A possible explanation is proposed based on variation of photoexcited electron density, which modulates glass properties, potentially leading to metalization. Such spatially nonhomogeneous conditions may result in LIPSS type modulation (LSFL-I vs LSFL-II). However, an effect of scattering on the pulse crater edges, as was observed for irradiation with flat-top pulses, that is capable of generating similar features, cannot be fully excluded.

The most unexpected results were obtained during scanning under a cylindrical lens focus. Along with typical 1D LSFL for scanning along the polarization, in perpendicular configuration more complex 2D highly periodic patterns were found. Their origin has a clear correlation with the LIPSS angle tilt with respect to polarization, however, additional investigation is needed to fully describe this effect.

On silicon, it was repeatedly observed that the highest LSFL regularity is obtained for the amorphous-crystalline structures. Unfortunately, these structures have no topographical features which are often required for applications. However, it is possible to chemically etch this surface, for example with KOH, to transform the crystallinity variation into a relief. Recently, such an option became possible and experiments are in progress.

# Appendices

## Appendix A: List of symbols

| Symbol | Unit | Description |
|---|---|---|
| $\omega_0$ | $\mu$m | Gaussian beam waist radius |
| $E$ | V/m | electric field intensity, polarization orientation |
| $I$ | W/m$^2$ | electric field intensity $I = \|E\|^2$ |
| x, y, z | m | geometric axes, position |
| $\Psi_{x,y}$ | % | pulse scanning overlap |
| $n_e$ | m$^{-3}$ | electron density |
| $\lambda$ | m | light wavelength |
| $\tau$ | s | laser pulse duration |
| $F$ | J/cm$^2$ | laser fluence |
| $F_{th}$ | J/cm$^2$ | (damage) threshold laser fluence |
| $F_{pk}$ | J/cm$^2$ | peak laser fluence (Gaussian beam) |
| $f_{rep}$ | Hz | laser repetition rate |
| $f$ | m | focal distance |
| $\Lambda$ | $\mu$m | LIPSS spatial period |
| OM | | optical microscopy |
| DIC | | differential interference contrast |
| CLSM | | confocal laser-scanning microscopy |
| DT | | damage threshold |
| NL | | non-linear |
| FS | | fused silica |

## Appendix B: DLOA structural parameter

In the process of periodic surface patterning, iterative approach of parametric search is often used to tune the processing parameters. After the processing, all the individual structures are rated and the most suitable parameters are chosen for further actions. Such process assumes we are able to rate and compare the structures, which is not necessarily a trivial task. Particularly in the case of LIPSS we have to assume several structural properties, e.g. are the LIPSS continuous, cover they all surface, are there phase discontinuities, is there change in orientation, is there ablation, etc.? Several such properties are usually changing in parallel and rating of the outcome is often subjective. One approach to create an objective comparison between two periodic structures with a focus on structure regularity (besides analyzing features in the Fourier transform), was introduced in the study by Gnilitskyi *et al.* [77]. Here, a parameter Dispersion of the LIPSS Orientation Angle (DLOA) was introduced. It is a result of a directional image analysis based on evaluation of the structure tensors (2x2 matrix of the local gradient of image intensity) in a local neighborhood of each image pixel. The method is implemented as a plug-in tool OrientationJ [188] for the image processing program ImageJ [189].

By analyzing the distribution of orientations in an image, we obtain a histogram of the amount of structures in the image being oriented in a specific angle (Fig. 72).

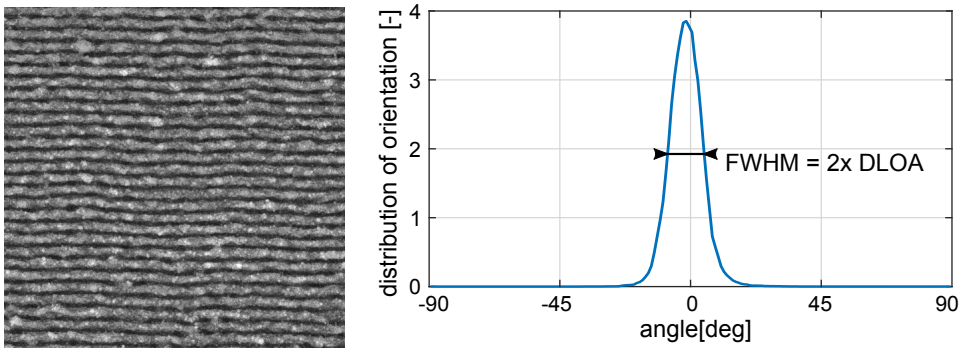


Figure 72: Example of ablative LIPSS on Si (SEM, 28x28 $\mu$m) and its orientation histogram calculated with OrientationJ (Gaussian weighting function, $w = 8$ pix).

Assuming there is one prevalent orientation, we can take a FWHM value of the orientation distribution peak and obtain the DLOA parameter. The narrower the peak is, the more uniform is the structure orientation.

However, after a closer investigation of the DLOA parameter several imperfections can be found. First, in the DLOA calculation, a local window ($w$ [pix]) is used, which size can be arbitrarily set. This, especially for noisy images, can result in almost arbitrary DLOA resulting from the same image, as can be seen in Fig. 73. Generally, different DLOA values can be obtained from the same structure measured with different magnification and/or resolution. This is especially true for ablative LIPSS, which in most cases, contain a large quantity of redeposited material in form of nano-particles. Having an input image with resolution better than the LIPSS period and setting a small processing window, orientation of the redeposited material will create a broadband angular distribution spectra resulting in a large DLOA and vice versa. This issue plays a role especially when two datasets measured at different imaging conditions should be compared.

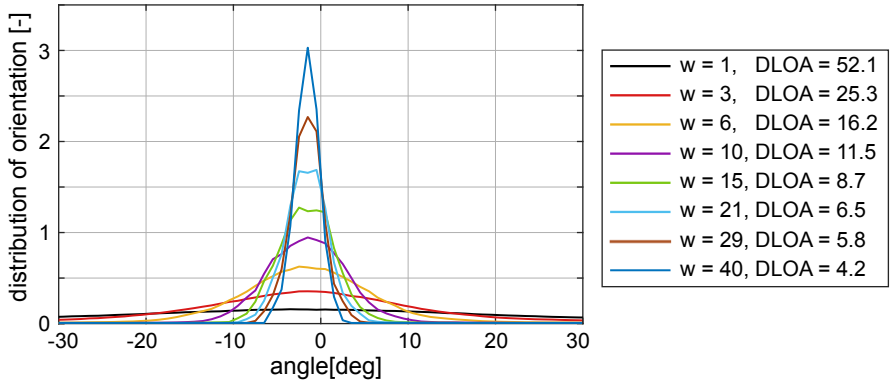


Figure 73: Distribution of orientation histograms of the image in Fig. 72 for a Gaussian gradient. Measured DLOA changes widely for different processing window sizes $w$.

Second issue with the DLOA definition is ambiguity of structure misorientation and noise. Both effects result in broadening of the angular distribution and can not be separated from a single DLOA scalar parameter. Figure 74 demonstrates this problem on

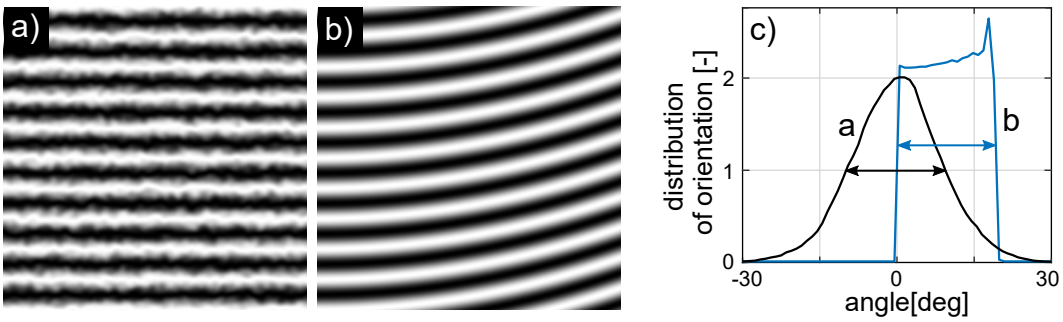


Figure 74: DLOA ambiguity: a) periodic structures containing noise and b) smooth periodic structures with a parabolic bend have the same DLOA of 10. c) distributions of orientation for a) and b).

simulated structures having the same DLOA parameter of 10 on a) $\sin(y)$ with noise and b) $\sin(y + \alpha x^2)$ with a parabolic phase bend.

It should be noted, that a statistically significantly large image of the structures must be evaluated.

From a mathematical point of view, any single scalar value defined by a 2D integration of the image will not describe the image uniquely. In the inverse problem, there will be more than one image resulting from a single scalar parameter. Still, DLOA, while not perfect, can provide some useful insight into evaluation and comparison of periodic structures. However the aforementioned limitations must be kept in mind.

## Appendix C: Challenges in the LIPSS scanning

An endeavor, to fabricate regular LIPSS uniformly on a large surface area, can be unfortunately compromised by a broad range of issues. Figure 75 exemplifies such issues, that are commonly encountered.

Assuming a laser-scanning setup is aligned perpendicular to the scanning laser beam (i.e. is not scanning in and out of focus), a beam shape is of acceptable quality and no pulse picker or attenuator leaks are present, first thing which could be noticed is insufficient sample cleanness or surface quality. Figure 75a gives an example of randomly distributed damages caused by laser interaction with surface particles.

A build-up phase exists in the LIPSS processing. It means, continuous surface modification will appear with some spatial delay up to hundreds of micrometers. Such delay, caused by gradually increasing positive feedback, may fluctuates for irradiation near threshold fluence (Fig. 75b). This has to be considered, when small regions are to be patterned. Perhaps, higher fluence in the initial few scan lines should be used. In addition, a rapid transition form no-modification to complete ablation is often observed for low fluence, large overlap regimes.

Surface particles can disrupt regularity of the LIPSS. This effects is the most pronounced, if such disruption occurs in the build-up phase of the LIPSS, as in the Fig. 75c.

Possibly the most problematic effect is spontaneous disordering and loss of directional coherency, demonstrated in Fig. 75d. This might be due to accumulation and amplifica-

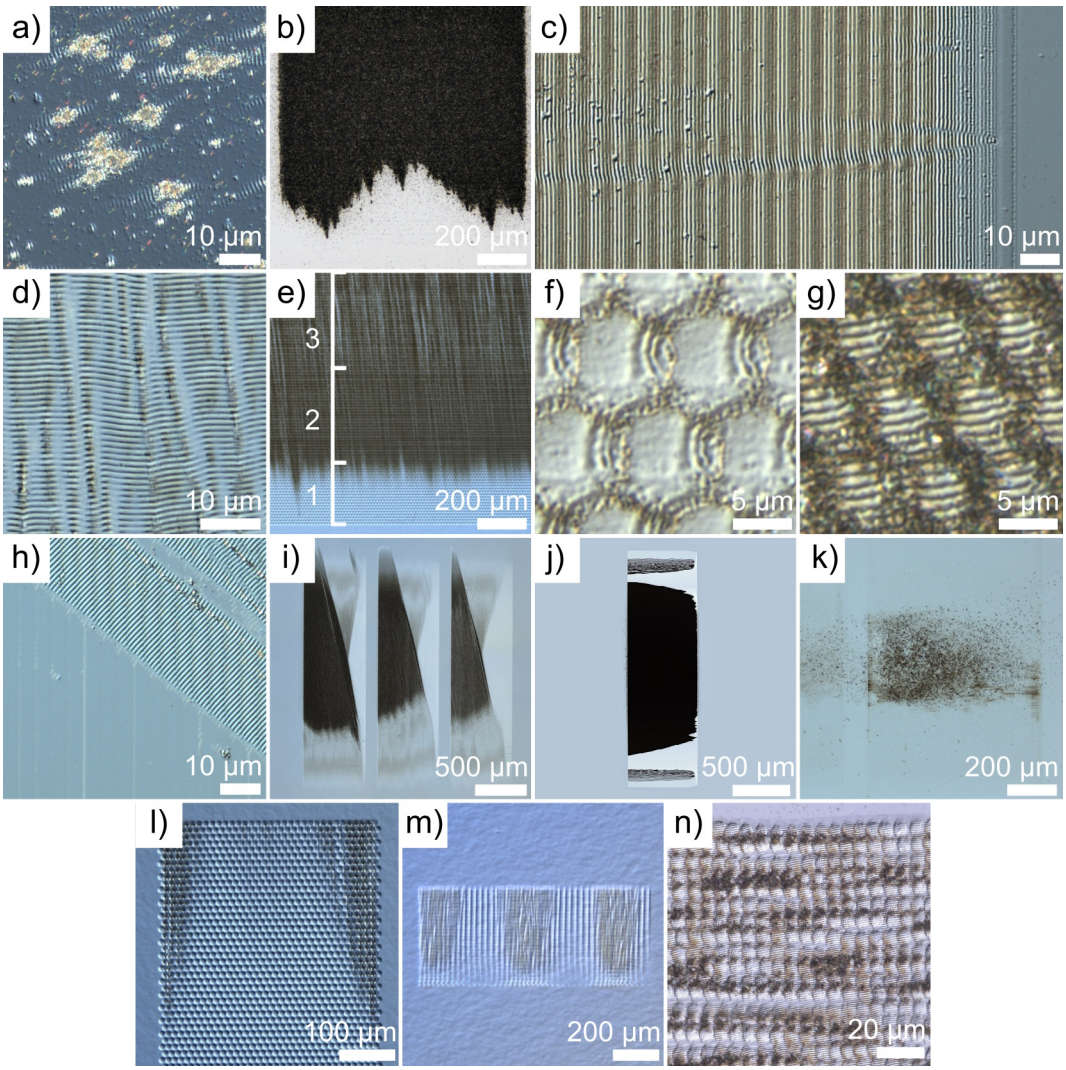


Figure 75: Challenges in the LIPSS scanning: a) dirty sample; b) delayed structure onset; c) disturbance in the build-up phase; d, e) disordering and loss of directional coherency; f, g) structures in the pulse border area for the same fluence and different overlaps; h) preferential extension direction; i) preferential extension direction and possible wavefront tilt; j) separation within the structured area; k) generation of nanoparticles; l) acceleration and deceleration phases of the scanning system; m) scanning velocity variation; n) low scanning position accuracy. Scanning from right to left. Silicon, except $SiO_2$ in f), g) and n).

tion of small deviations caused for example by fluence dependent spatial period, resulting from Gaussian fluence distribution. It is not rare to observe this effect to appear with some delay as in Fig. 75e, consisting of 1) the build-up phase, 2) a region of relatively homogeneous LIPSS and 3) a disordered regime. An opposite transition from disordered to aligned LIPSS is not observed. Disordering can be spontaneous or triggered by a glitch in the laser scanning (spacing, power). To suppress the disordering, another scanning/irradiation parameters should be used.

Figure 75f-g demonstrates overlap effects on fused silica (that are generally more pronounced than on silicon). For a given fluence, there may not be an overlap to produce

uniform structuring without partial ablation in the pulse overlapping area. Either the LIPSS are only in the overlapping area (note the change in the LIPSS orientation), or they cover the central part of the pulses, but the edges are already ablated. In this particular irradiation, fluence was too high. For lower fluence, homogeneous LIPSS patterning without ablation and blank spots was possible.

LIPSS on silicon are coherently extended preferentially in the direction perpendicular to the LIPSS. Figure 75h shows an irradiation through a cylindrical lens, where LIPSS are extended only in a collimated band, perpendicular to the LIPSS, even though all the area received the same fluence. Figure 75i shows a similar experiment also with cylindrical lens focusing, where the LIPSS emerge at the edges of the focal spot and propagate towards its center. In this case, we believe such result it is due to interplay of pulse wavefront tilt and specific fluence and overlap conditions. In another experiment with better control of the beam parameters far less pronounced signs of such geometrical distribution of the LIPSS were observed. Although, in both experiments we could observe LIPSS discontinuity along the focal spot. Figure 75j demonstrates an extreme case of such structuring separation into three zones. The separating regions typically show amorphization, with no periodic structuring by LSFL. On the other hand, highly regular amorphous LSFL are often found in the side regions. The gap in an otherwise continuous structuring closely resembles a gap in the parametric space in the Fig. 38f, resulting form a peculiar interplay of fluence, spot size and pulse overlap. Therefore, to remove this effect, a flat-top beam profile along the focusing axis should be used, to maintain constant fluence outside of the no-LIPSS parametric range.

In some occasions, scanning of silicon resulted in a barely modified surface, but with a large quantity of redeposited nanoparticles (Fig. 75j), which can spread to a surrounding area. Therefore an air suction system should be used even in "non-ablative" regime, creating flow of the air above a sample from the pristine surface towards the scanned area.

Lastly, there are problems connected with the laser scanning precision, which are exemplified in Fig. 75k,l,m. In Fig. 75k acceleration and deceleration at the ends of the scanning lines is visible. Figure 75l shows scanning stage speed oscillation, probably due to controller PID loop instability at very low speed. Finally, Fig. 75m shows a result of the scanning with low positioning accuracy. The issues l) and m) should be possible to solve by correct software settings, while the low accuracy problem requires a change of the hardware.

## Appendix D: Linear motion stage synchronization

Throughout the experiments, there was a need to synchronize motion of the linear stages with the laser systems. In particular for the DDS100 (Thorlabs) stages with KBD101 controllers used in an $x$-$y$ configuration, as described in the Section 2.1.5. Unfortunately, these controllers do not have a direct hardware support for such task. However, thanks to two programmable IO ports, there are two options how to circumvent this problem.

1) The stage motion will be started by a laser pulse signal and after a predefined delay laser pulse picker is opened. This option was attempted, but was unsuccessful due to large stage positioning jitter. That means, position of the moving stage after a fixed time

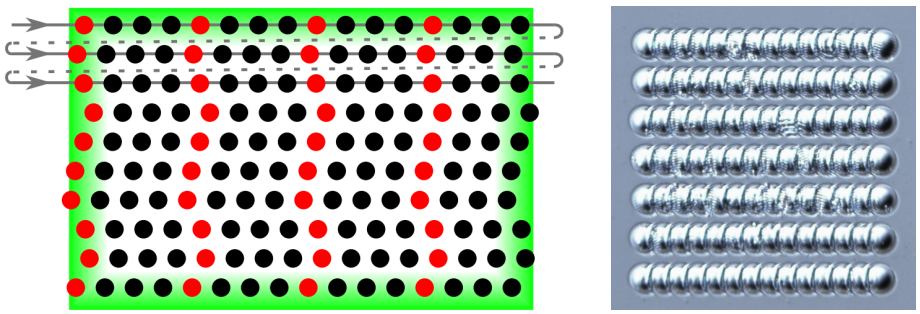

Figure 76: A rectangular region (green) scanned by a non-synchronized laser. Sequence of the laser scanning is indicated by arrows. When taking every N-th pulse (here $N = 4$) a semi-synchronized pattern emerges (red). b) An image of laser-scanned area with equidistantly spaced pulses produced by this method.

after issuing a move signal was not repeatable.

2) The other option is to externally divide the laser repetition frequency and synchronize this lower frequency to the stage. From the nature of a pulsed laser system, the other way around of triggering the laser by an external device at arbitrary time is not possible. If triggered, i.e. pulse picker (PP) is opened, a pulse is emitted only when the pulse is present at the laser internal repetition frequency. If an area is scanned without synchronization, pulses in two consequent lines are mutually randomly offset, as illustrated in Fig. 76. That means the synchronization error (jitter) is the whole period (time or distance) between 2 pulses at a given laser repetition rate and scanning speed. If the scanning controller is able to precisely detect a specific stage position, this position can be set as an edge of the area to be scanned. Next, we will use only every $N$-th laser pulse for the irradiation. When the scanner crosses the border of the area to be scanned, the first and every $N$-th available laser pulse will be used for irradiation, as illustrated by red positions in Fig. 76. As a consequence, the relative positioning error will be reduced $N$-times compared to the non-synchronized case. For a sufficiently large $N$, pseudosynchronization is achieved.

This approach, was used in several experiments reported in the Results, for example in Section 3.3.2. Practical implementation was realized by an electronic circuit, which I designed and built. Fig. 77 shows its schematics. There are two input signals. Laser outputs the SYNC IN signal on a default repetition rate, which starts to be divided by 18 as soon as the stage motion controller sends a GATE IN pulse. GATE IN pulse indicates the time during which the stage is moving over the area to be scanned. The counter is reset after 18 pulses and counting restarts. The divided frequency is then delayed by an RC element, as shown in the oscilloscope trace in Fig. 77, to match the PP open window with a next pulse.

The circuit in Fig. 77 shows that the division ratios are 18/10/6× depending on the SW1 switch, however the chip was faulty, resetting the Q2 output to high. Therefore the counting cycle was by 4 shorter. Division by 14 was more suitable for our scanning conditions than 10 or 18, so we considered this bug as a feature and left it unchanged.

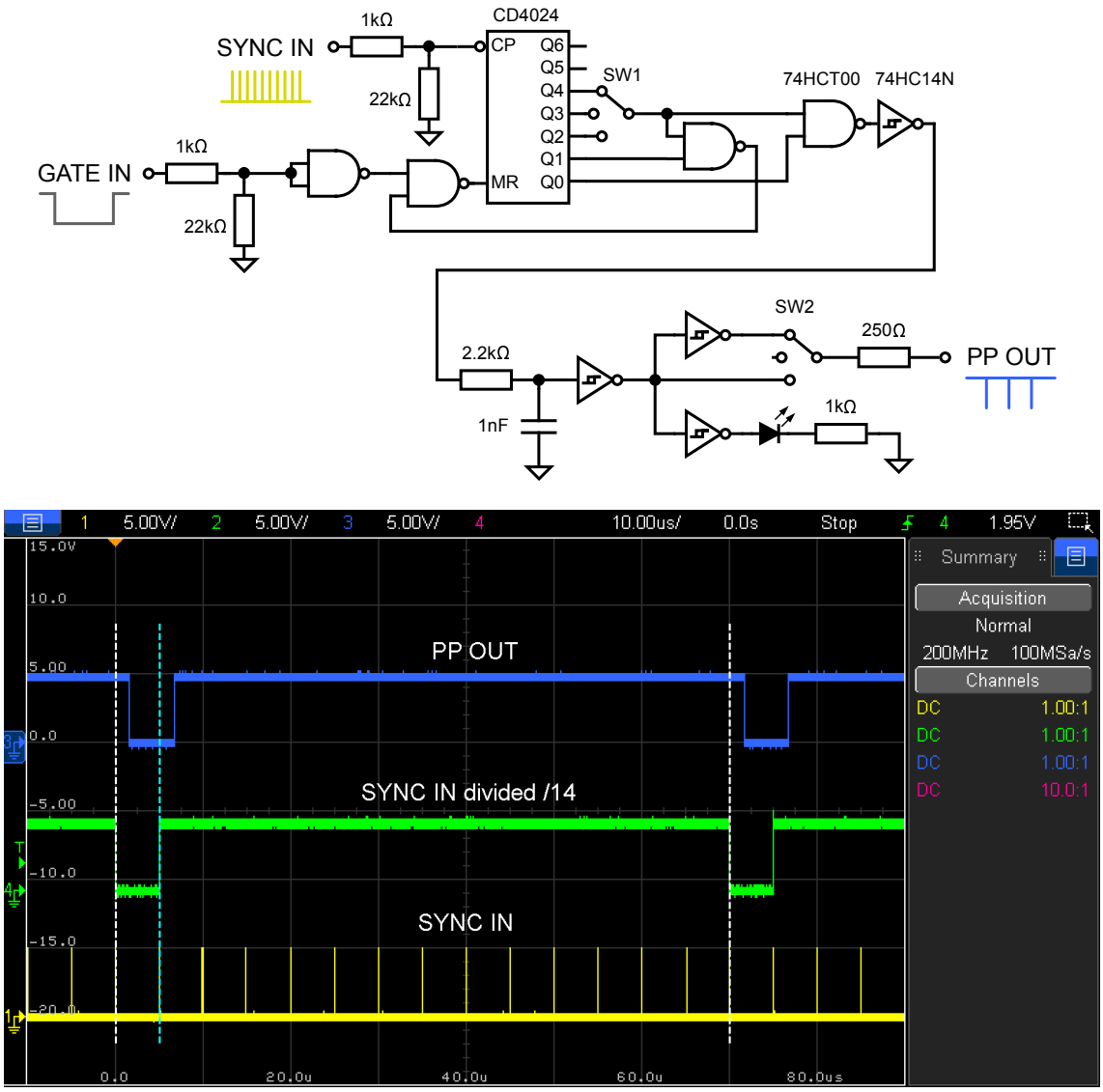


Figure 77: Pseudo-synchronization circuit of the laser to a linear stage. Binary counter, counting at the laser repetition frequency provided by the SYNC IN signal, is gated by the GATE IN signal from the motion controller. SYNC IN frequency is divided by 18/10/6x depending on the SW1 position. Output PP enable signal is delayed by an RC delay element and polarity of the output PP OUT is set by the switch SW2. The oscilloscope traces demonstrate timing sequence of the circuit. 200 kHz SYNC IN signal from the laser is divided by 14 (see text), expanded to 5 $\mu$s and delayed by $\sim 1.7\mu$s (PP OUT) to match the window with a next pulse.

## Appendix E: Motion stage controller

Due to a stage driver malfunction, we were not able to operate two stages (Standa 8MT160-300 – linear, Standa 8MR151 – rotational). It was problematic at the time (Covid) to acquire new drivers, therefore I decided to build them myself. As both stages are powered by a low power bipolar stepper motor, it is relatively easy to build a decent driver based on an Arduino micro-controller (Arduino Micro) and a stepper driver module (A4988).

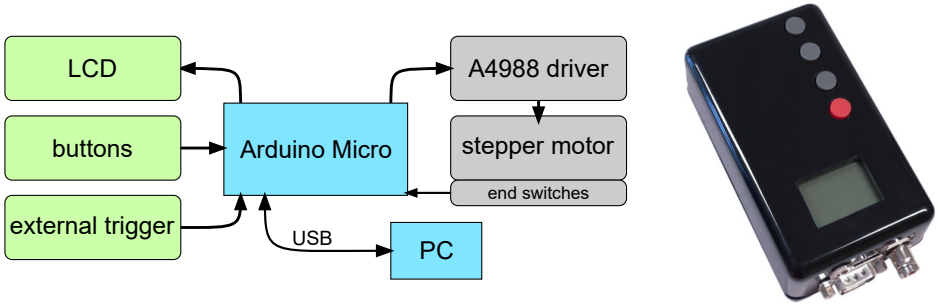


Figure 78: A function block schema of the stepper controller / driver and its complete version.

Fig. 78 shows a block diagram of the controller and the Fig. 79 shows the used circuit in detail. Arduino was running an own, fully custom program. It gets inputs from an external trigger, 4 user buttons and two stage end-switches. It is also sending instructions to a Nokia 5510 LCD, showing the real time stage position, triggering status, current cycle, etc. Arduino commands the driver module, to control motion of the stepper motor. A precise motion is achieved by proper ramp-up and ramp-down speed sequences (ATMEL AVR Application note AVR446) implemented on a 16-bit timer.

Despite the possibility to use the controller as a standalone unit, it is better to interact with it by a serial line. A set of basic instructions (start, stop, set speed, set acceleration, set triggering parameters, driver disable, driver reset, stage home, jogging, mode linear/rotational, position zero, debug information and command help) is available. The driver motor input requires an external power supply of 12-24V. The rest of the circuits are powered by a 5V delivered either through the USB or by a 5V linear regulator from the main motor voltage. The the finished driver is depicted in Fig. 78.

The controlled rotation stage was used to study the dependence of the damage threshold on the polarization orientation with respect to the crystalline orientation of silicon (Section 3.1.2).

## Appendix F: Automatic laser spot evaluation

In laser-material modification experiments, material damage/modification threshold is a key variable, as it defines the range of laser power used for processing. During some experiments, it was necessary to repeatedly measure and evaluate damage thresholds in large datasets. Evaluation of such datasets by hand is not only time consuming, but also brings a potential for errors due to subjective decisions, where the damage boundary lies. This is especially true, when a single dataset is evaluated over multiple sessions.

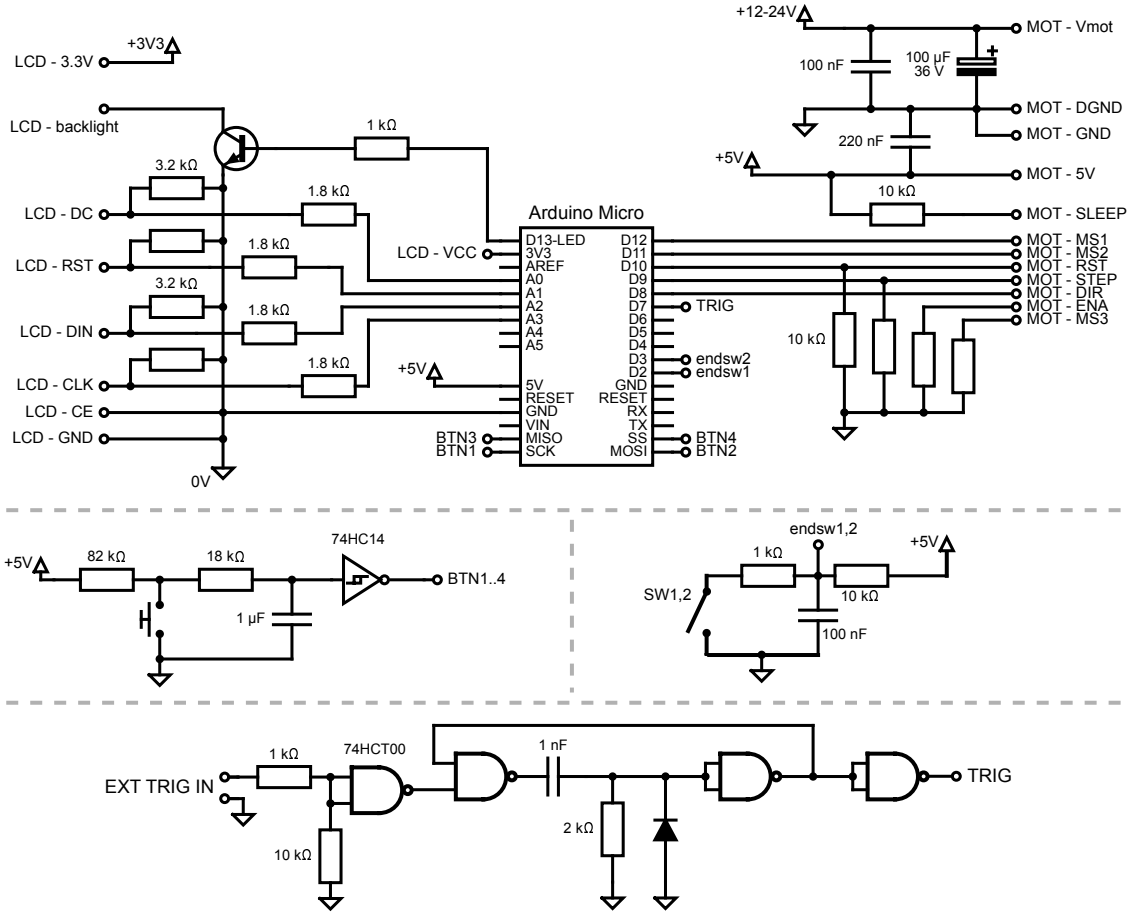


Figure 79: A scheme of the stepper motor controller. The main circuit block shows the Arduino Micro and connections to an LCD and motor driver modules. The three sub-circuits correspond to a button and end-switch de-bouncing circuits, and an external trigger pulse shaping circuit.

Automatic, or more precisely computer assisted, data evaluation can greatly reduce evaluation time and increase precision and repeatability of the measurement. The following text is focused on such task, where the individual steps of the process I developed and implemented are discussed in detail. Reminding the Section 2.1.3.1, to evaluate material laser damage threshold, it is required to analyze sizes of $N$ modified areas, each corresponding to a different pulse energy. The automatic procedure therefore needs to find these areas and determine its size. Figure 80 shows a typical workflow of the data evaluation process. Preliminary steps, needed to be considered already in the experiment planning, include: a) spacing of the data points – data points must not interfere with each other, however b) small experiment size – to limit the effects of possible sample nonhomogenities and misfocusing due to a potential sample tilt; c) experiment duration – due to fluctuation in laser power and environmental conditions longer experiments may have larger error; d) clear experiment layout with marking points – to ease later analysis.

*Image acquisition* (Fig. 80-1) – Laser irradiated sites can be imaged individually ($N$ sites = $N$ images, N-in-N) or in an automated image acquisition as a single image of the whole experiment (all-in-1). In the latter case the acquisition is error prone to

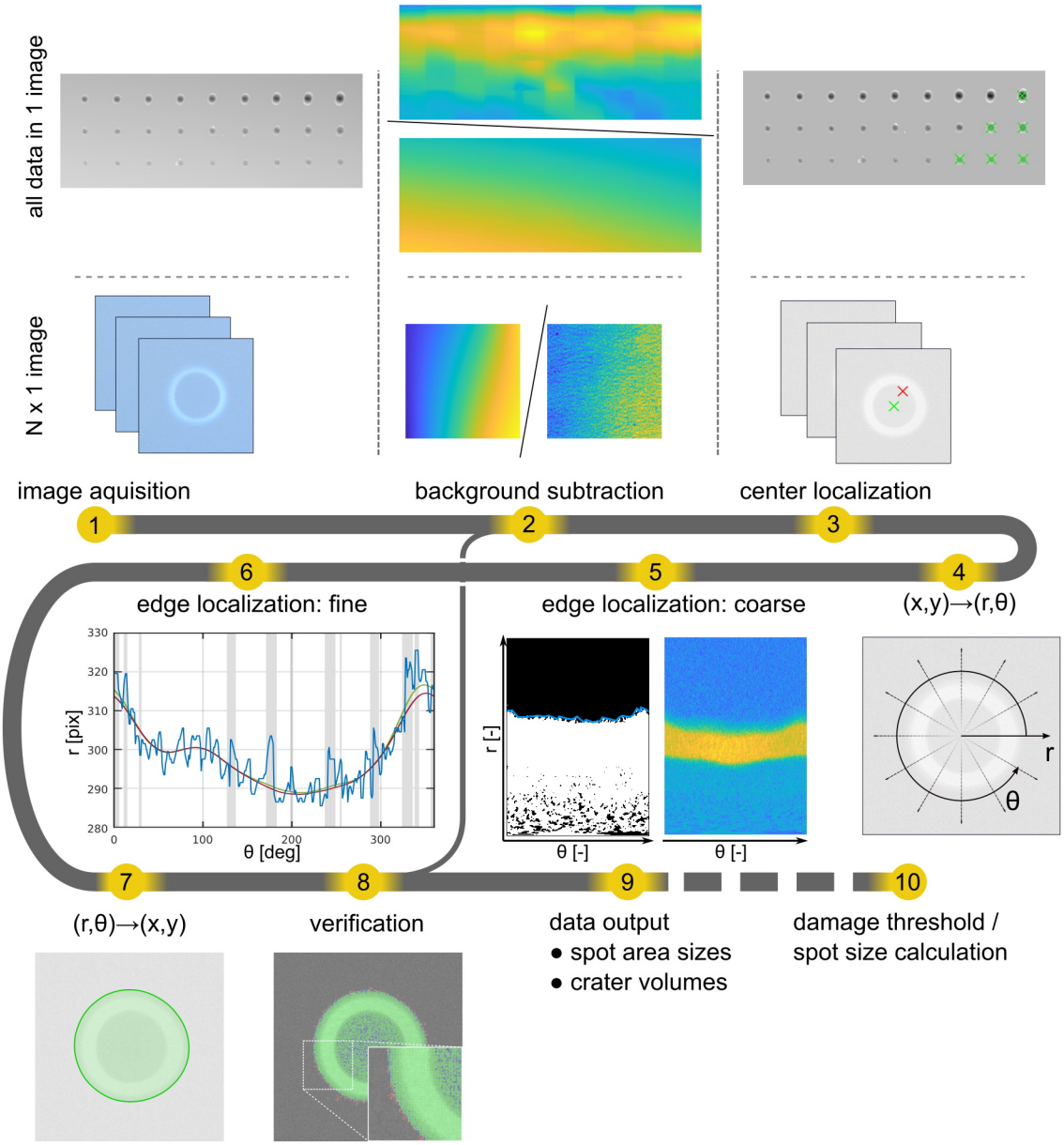


Figure 80: Diagram of the computer assisted spot size / damage threshold batch processing. Steps are explained in detail in the main text.

skipped/unordered images or misfired points, but may suffer data stitching offset errors and ∼500 Mpix dataset, which is common, is problematic to work with. In the N-in-N case, image settings must be set to manual and must not change during the whole acquisition. It is also a good practice to center the areas of interest into the middle of the image, to set only one exposure in a way to use the full bit depth of the camera without over/under-exposure and keep the images in focus. During the experiments on silicon it was discovered the blue channel of the RGB image from the DIC optical image has the highest contrast for the silicon amorphization (the lowest modification threshold) and therefore was used in further data evaluation. Even better contrast is obtained in the

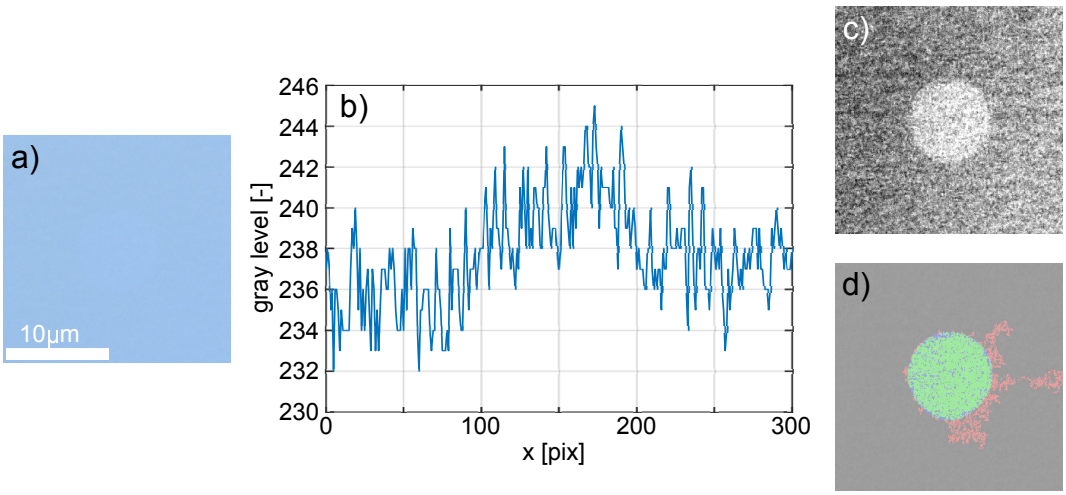


Figure 81: Importance of the background subtraction demonstrated on a typical 2 ps, low fluence irradiation spot on silicon. a) The input data image (OM DIC image with a barely visible damage). b) Its horizontal profile (blue color channel). c) The same image with an enhanced contrast. d) A green overlay verification mask confirming correct area evaluation.

intensity images from the laser scanning confocal microscope using a 405 nm laser diode, but acquisition speed was too slow for large experiments.

*Background subtraction* (Fig. 80-2) – Background subtraction is a critical part in many evaluations, which if not done correctly, renders further evaluation impossible. As demonstrated in Fig. 81b, the image data may have contrast as low as a few levels of gray (LG) for an 8 bit image. Therefore the background of more than ±2 LG can pose a significant problem in evaluation. The background correction procedure depends on the input data type and data contrast. For the N-in-N case, a simple polynomial background fit is sufficient for high-contrast data. Only the modified region itself must be excluded from the fit. Better results were achieved, when several images of clean unmodified area were averaged and used for background correction, as it was found that our imaging system has a static noise of approximately ±2.5 LG. For the all-in-1 data, background can be subtracted by a polynomial fit over the whole image. However, there may be a specific type of the background fluctuation resulting from the image stitching, as shown in Fig. 80-2 up, which can be removed by an iterative spline fitting in x and y direction, while excluding the irradiation sites. If the N-in-N images were measured in sets, it is useful to subtract also an average in every set, which reduces background approximately by another ±4 LG. This step corrects brightness, while the previous correction removes static noise and background tilt. Also later during final processing an average of every individual image is corrected based on its border region values correcting additional ±0.5 LG. It is important to note that the images must be converted to floating point numbers prior to background correction and left as such by the end of the evaluation.

*Center localization and transformation to polar coordinates* (Fig. 80-3,4) – Further processing requires transformation of the image from Cartesian to polar coordinates. Therefore, centers of the modified areas have to be found first. It is possible to automatize this task, but in case the data were acquired aligned or spaced in regular grid,

their positions are already known and usually only a few low fluence points require manual correction.

*Edge localization* (Fig. 80-5,6) – Edge localization is the main part of the evaluation. Its success depends on the data signal to noise ratio. The image data, in the polar coordinates, are thresholded a few LG above the background. A resulting mask is median filtered and a continuous connected region is found (Fig. 80-5 left). The upper border of this region presents a coarse outline of the modified region, which is to be found. However, unlike in this example, this borderline may be strongly corrupted. Therefore a second step follows, where this outline is iteratively approximated by a smooth function, rejecting and restoring strongly deviating parts of the profile. This implicitly requires the laser spot to be close to circular.

*Inverse transformation of coordinates* (Fig. 80-7) – Transforming the iteratively refined profile from the previous step back to the Cartesian coordinates results in an outline path of the modified region, whose area is easily calculated. Further, if height data are available, multiplying this 2D area with the CLSM depth data provides an ablated volume.

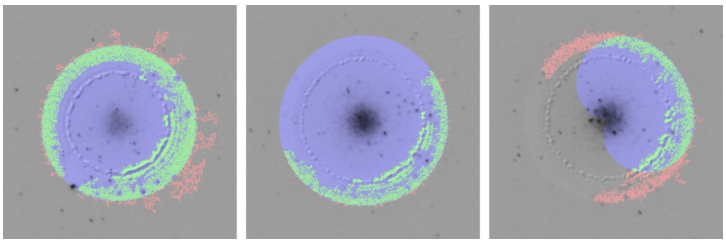

Figure 82: A series of verification images. Left - correct evaluation of the modified area; center - still correct evaluation, even though half of the input area was not registered; right - failed evaluation.

*Verification* (Fig. 80-8) – The above procedure can fail in several steps, especially when the image data contain scratches, ablation debris, have variable exposure, wrong center position, etc. Usually, only a few data points are corrupted due to local defects. Still, these need to be excluded from further calculations. The verification process can be done visually. For that, the full input data set (the N-in-N data are organized into a single joint image matrix) is overlaid by color-coded binary masks, as used in Fig. 80-8, Fig. 81d and Fig. 82. These masks correspond to the regions selected by a single grayscale level thresholding of the background-subtracted image (red), regions selected by the above procedure as the damage area (blue) and an overlap of these two regions (green).

*Data output and damage threshold/spot size calculation* – Finaly, resulting data are used directly for spot size and damage threshold calculation or are output to a .csv file.

This procedure was implemented using Matlab and was used in several experiments reported in this work, in particular in the orientation-dependent damage threshold of Si in the Section 3.1.2.

# References


[1] J. Bonse and S. Gräf. Ten open questions about laser-induced periodic surface structures. *Nanomaterials*, **11**(12):3326, 2021.

[2] M. V. Shugaev, Ch. Wu, O. Armbruster, A. Naghilou, N. Brouwer, D. S. Ivanov, T. J.-Y. Derrien, N. M. Bulgakova, W. Kautek, B. Rethfeld, and L. V. Zhigilei. Fundamentals of ultrafast laser–material interaction. *MRS Bulletin*, **41**(12):960–968, 2016.

[3] S. I. Anisimov, B. L. Kapeliovich, and T. L. Perelman. Electron emission from metal surfaces exposed to ultrashort laser pulses. *JETP Lett.*, **39**:375–377, 1974.

[4] N. Bulgakova. Fundamentals of ultrafast laser processing. In Ya Cheng, editor, *Ultrafast Laser Processing*, pages 99–181. Pan Stanford Publishing, 2013.

[5] C.-K. Sun, F. Vallée, L. H. Acioli, E. P. Ippen, and J. G. Fujimoto. Femtosecond-tunable measurement of electron thermalization in gold. *Phys. Rev. B*, **50**(20):15337–15348, 1994.

[6] S. E. Kirkwood, Y. Y. Tsui, R. Fedosejevs, A. V. Brantov, and V. Yu. Bychenkov. Experimental and theoretical study of absorption of femtosecond laser pulses in interaction with solid copper targets. *Phys. Rev. B*, **79**(14):144120, 2009.

[7] S. Leyder, D. Grojo, P. Delaporte, W. Marine, M. Sentis, and O. Utéza. Non-linear absorption of focused femtosecond laser pulses at 1.3 $mu$m inside silicon: Independence on doping concentration. *Appl. Surf. Sci.*, **278**:13–18, 2013.

[8] H. M. Van Driel. Kinetics of high-density plasmas generated in Si by 1.06 and 0.53 $mu$m picosecond laser pulses. *Phys. Rev. B*, **35**(15):8166–8176, 1987.

[9] M. B. Agranat, S. I. Ashitkov, S. I. Anisimov, A. V. Ovchinnikov, A. B. Shvartsburg, D. S. Sitnikov, and V. E. Fortov. Formation of absorbing heterogeneous plasma layer by femtosecond laser-induced melting and ablation of silicon. *Appl. Phys. A*, **94**(4):879–887, 2009.

[10] A. Mermillod-Blondin, I. M. Burakov, Yu. P. Meshcheryakov, N. M. Bulgakova, E. Audouard, A. Rosenfeld, A. Husakou, I. V. Hertel, and R. Stoian. Flipping the sign of refractive index changes in ultrafast and temporally shaped laser-irradiated borosilicate crown optical glass at high repetition rates. *Phys. Rev. B*, **77**(10):104205, 2008.

[11] J. Song, X. Wang, X. Hu, Ye Dai, J. Qiu, Ya Cheng, and Z. Xu. Formation mechanism of self-organized voids in dielectrics induced by tightly focused femtosecond laser pulses. *Appl. Phys. Lett.*, **92**(9):092904, 2008.

[12] S. Gräf, C. Kunz, and F. Müller. Formation and properties of laser-induced periodic surface structures on different glasses. *Materials*, **10**(8):933, 2017.

[13] Y. Shimotsuma, P. G. Kazansky, J. Qiu, and K. Hirao. Self-organized nanogratings in glass irradiated by ultrashort light pulses. *Phys. Rev. Lett.*, **91**(24):247405, 2003.

[14] R. Buividas, G. Gervinskas, A. Tadich, B. C. C. Cowie, V. Mizeikis, A. Vailionis, D. de Ligny, E. G. Gamaly, A. V. Rode, and S. Juodkazis. Phase transformation in laser-induced micro-explosion in olivine $(Fe,Mg)_2$ $SiO_4$. *Adv. Eng. Mater.*, **16**(6):767–773, 2014.

[15] P. Martin, S. Guizard, Ph. Daguzan, G. Petite, P. D'Oliveira, P. Meynadier, and M. Perdrix. Subpicosecond study of carrier trapping dynamics in wide-band-gap crystals. *Phys. Rev. B*, **55**(9):5799–5810, 1997.

[16] S. S. Mao, F. Quéré, S. Guizard, X. Mao, R. E. Russo, G. Petite, and P. Martin. Dynamics of femtosecond laser interactions with dielectrics. *Appl. Phys. A*, **79**(7):1695–1709, 2004.

[17] K. Tanimura, H. Fujiwara, and T. Suzuki. Time resolved spectroscopy for radiation damage processes induced by electronic excitation in insulators. *Nucl. Instrum. Methods Phys. Res. B*, **116**(1-4):26–32, 1996.

[18] A. Rosenfeld, M. Lorenz, R. Stoian, and D. Ashkenasi. Ultrashort-laser-pulse damage threshold of transparent materials and the role of incubation. *Appl. Phys. A*, **69**(7):S373–S376, 1999.

[19] N. M. Bulgakova, R. Stoian, and A. Rosenfeld. Laser-induced modification of transparent crystals and glasses. *Quantum Electron.*, **40**(11):966–985, 2010.

[20] M. O. Thompson, J. W. Mayer, A. G. Cullis, H. C. Webber, N. G. Chew, J. M. Poate, and D. C. Jacobson. Silicon melt, regrowth, and amorphization velocities during pulsed laser irradiation. *Phys. Rev. Lett.*, **50**(12):896–899, 1983.

[21] M. Henyk, D. Wolfframm, and J. Reif. Ultra short laser pulse induced charged particle emission from wide bandgap crystals. *Appl. Surf. Sci.*, **168**(1-4):263–266, 2000.

[22] R. Kelly and A. Miotello. Comments on explosive mechanisms of laser sputtering. *Appl. Surf. Sci.*, 96-98:205–215, 1996.

[23] L. V. Zhigilei, Z. Lin, and D. S. Ivanov. Atomistic modeling of short pulse laser ablation of metals: connections between melting, spallation, and phase explosion. *J. Phys. Chem. C*, **113**(27):11892–11906, 2009.

[24] W. G. Roeterdink, L. B. F. Juurlink, O. P. H. Vaughan, J. Dura Diez, M. Bonn, and A. W. Kleyn. Coulomb explosion in femtosecond laser ablation of Si(111). *Appl. Phys. Lett.*, **82**(23):4190–4192, 2003.

[25] N. M. Bulgakova, R. Stoian, A. Rosenfeld, I. V. Hertel, and E. E. B. Campbell. Electronic transport and consequences for material removal in ultrafast pulsed laser ablation of materials. *Phys. Rev. B*, **69**(5):054102, 2004.

[26] R. Stoian, D. Ashkenasi, A. Rosenfeld, and E. E. B. Campbell. Coulomb explosion in ultrashort pulsed laser ablation of $Al_2O_3$. *Phys. Rev. B*, **62**(19):13167–13173, 2000.

[27] K. Sokolowski-Tinten, J. Bialkowski, and D. Von Der Linde. Ultrafast laser-induced order-disorder transitions in semiconductors. *Phys. Rev. B*, **51**(20):14186–14198, 1995.

[28] A. Rousse, C. Rischel, S. Fourmaux, I. Uschmann, S. Sebban, G. Grillon, P. Balcou, E. Forster, J. P. Geindre, P. Audebert, J. C. Gauthier, and D. Hulin. Non-thermal melting in semiconductors measured at femtosecond resolution. *Nature*, **410**:65–68, 2001.

[29] Y. Jee, M. F. Becker, and R. M. Walser. Laser-induced damage on single-crystal metal surfaces. *J. Opt. Soc. Am. B*, **5**(3):648–659, 1988.

[30] P. T. Mannion, J. Magee, E. Coyne, G. M. O'Connor, and T. J. Glynn. The effect of damage accumulation behaviour on ablation thresholds and damage morphology in ultrafast laser micro-machining of common metals in air. *Appl. Surf. Sci.*, **233**(1-4):275–287, 2004.

[31] S. Nolte, C. Momma, H. Jacobs, B. N. Chichkov, B. Wellegehausen, and H. Welling. Ablation of metals by ultrashort laser pulses. *J. Opt. Soc. Am. B*, **14**(10):2716–2722, 1997.

[32] C. Kerse, H. Kalaycioglu, P. Elahi, B. Cetin, D. K. Kesim, Ö. Akcaalan, S. Yavas, M. D. Asık, B. Öktem, H. Hoogland, R. Holzwarth, and F. Ö. Ilday. Ablation-cooled material removal with ultrafast bursts of pulses. *Nature*, **537**(7618):84–88, 2016.

[33] C. Kerse, H. Kalaycioglu, P. Elahi, K. Yavuz, I. Mirza, N. M. Bulgakova, and F. Ö Ilday. Ultrafast micromachining of Cu and Si at ultra-high repetition rates with pulse bursts. In *2015 11th Conference on Lasers and Electro-Optics Pacific Rim (CLEO-PR)*, pages 1–2, Busan, Korea (South), 2015. IEEE.

[34] F. Caballero-Lucas, J. Sládek, I. Mirza, N. M. Bulgakova, K. Obata, and K. Sugioka. Ultrafast pulse GHz burst mode laser ablation for efficient surface microprocessing. Dresden, Germany, 2020. [poster session].

[35] K. Obata, F. Caballero-Lucas, and K. Sugioka. Material processing at GHz burst mode by femtosecond laser ablation. *J. Laser Micro Nanoeng.*, **16**(1):19–23, 2021.

[36] S. M. Klimentov, T. V. Kononenko, P. A Pivovarov, S. V. Garnov, V. I. Konov, A. M. Prokhorov, D. Breitling, and F. Dausinger. The role of plasma in ablation of materials by ultrashort laser pulses. *Quantum Electron.*, **31**(5):378–382, 2001.

[37] A. V. Bulgakov, I. Mirza, N. M. Bulgakova, V. P. Zhukov, R. Machulka, O. Haderka, E. E. B. Campbell, and T. Mocek. Initiation of air ionization by ultrashort laser pulses: evidence for a role of metastable-state air molecules. *J. Phys. D: Appl. Phys.*, **51**(25):25LT02, 2018.

[38] A. Weck, T. H. R. Crawford, D. S. Wilkinson, H. K. Haugen, and J. S. Preston. Laser drilling of high aspect ratio holes in copper with femtosecond, picosecond and nanosecond pulses. *Appl. Phys. A*, **90**(3):537–543, 2008.

[39] A. Ben-Yakar and R. L. Byer. Femtosecond laser ablation properties of borosilicate glass. *J. Appl. Phys.*, **96**(9):5316–5323, 2004.

[40] M. Ardron, N. Weston, and D. Hand. A practical technique for the generation of highly uniform LIPSS. *Appl. Surf. Sci.*, **313**:123–131, 2014.

[41] P. M. Fauchet and A. E. Siegman. Surface ripples on silicon and gallium arsenide under picosecond laser illumination. *Appl. Phys. Lett.*, **40**(9):824–826, 1982.

[42] J. Bonse, M. Munz, and H. Sturm. Structure formation on the surface of indium phosphide irradiated by femtosecond laser pulses. *J. Appl. Phys.*, **97**(1):013538, 2005.

[43] I. Gnilitskyi, V. Gruzdev, N. M. Bulgakova, T. Mocek, and L. Orazi. Mechanisms of high-regularity periodic structuring of silicon surface by sub-MHz repetition rate ultrashort laser pulses. *Appl. Phys. Lett.*, **109**(14):143101, 2016.

[44] Y. Fuentes-Edfuf, M. Garcia-Lechuga, D. Puerto, C. Florian, A. Garcia-Leis, S. Sanchez-Cortes, J. Solis, and J. Siegel. Coherent scatter-controlled phase-change grating structures in silicon using femtosecond laser pulses. *Sci. Rep.*, **7**(1):4594, 2017.

[45] S. Höhm, A. Rosenfeld, J. Krüger, and J. Bonse. Femtosecond laser-induced periodic surface structures on silica. *J. Appl. Phys.*, **112**(1):014901, 2012.

[46] S. Schwarz. Two-dimensional low spatial frequency laser-induced periodic surface structuring of sapphire. *J. Laser Micro Nanoeng.*, **12**(2):67–71, 2017.

[47] S. Schwarz, S. Rung, C. Esen, and R. Hellmann. Homogeneous low spatial frequency LIPSS on dielectric materials generated by beam-shaped femtosecond pulsed laser irradiation. *J. Laser Micro Nanoeng.*, **13**(2):90–94, 2018.

[48] K. Bischoff, P. Quigley, A. Hohnholz, P. Jäschke, and S. Kaierle. Generation of laser-induced periodic surface structures on different glasses by a picosecond-pulsed laser. *Procedia CIRP*, **94**:924–929, 2020.

[49] R. J. Nemanich, D. K. Biegelsen, and W. G. Hawkins. Aligned, coexisting liquid and solid regions in laser-annealed Si. *Phys. Rev. B*, **27**(12):7817–7819, 1983.

[50] J. Bonse, S. Baudach, J. Krüger, W. Kautek, and M. Lenzner. Femtosecond laser ablation of silicon–modification thresholds and morphology. *Appl. Phys. A*, **74**(1):19–25, 2002.

[51] J. Bonse and J. Krüger. Pulse number dependence of laser-induced periodic surface structures for femtosecond laser irradiation of silicon. *J. Appl. Phys.*, **108**(3):034903, 2010.

[52] T. J.-Y. Derrien, T. E. Itina, R. Torres, T. Sarnet, and M. Sentis. Possible surface plasmon polariton excitation under femtosecond laser irradiation of silicon. *J. Appl. Phys.*, **114**(8):083104, 2013.

[53] J. Bonse, A. Rosenfeld, and J. Krüger. On the role of surface plasmon polaritons in the formation of laser-induced periodic surface structures upon irradiation of silicon by femtosecond-laser pulses. *J. Appl. Phys.*, **106**(10):104910, 2009.

[54] D. C. Emmony, R. P. Howson, and L. J. Willis. Laser mirror damage in germanium at 10.6 um. *Appl. Phys. Lett.*, **23**(11):598–600, 1973.

[55] J. E. Sipe, Jeff F. Young, J. S. Preston, and H. M. van Driel. Laser-induced periodic surface structure. I. Theory. *Phys. Rev. B*, **27**(2):1141–1154, 1983.

[56] J. Bonse, S. Höhm, S. V. Kirner, A. Rosenfeld, and J. Krüger. Laser-induced periodic surface structures— a scientific evergreen. *IEEE J. Select. Topics Quantum Electron.*, **23**(3):7581030, 2017.

[57] J. Bonse and S. Gräf. Maxwell meets Marangoni - A review of theories on laser-induced periodic surface structures. *Laser Photonics Rev.*, **14**(10):2000215, 2020.

[58] J. Bonse, J. Krüger, S. Höhm, and A. Rosenfeld. Femtosecond laser-induced periodic surface structures. *J. Laser Appl.*, **24**(4):042006, 2012.

[59] J. Gottmann, D. Wortmann, and R. Wagner. Manufacturing of periodical nanostructures by fs-laser direct writing. In R. Myllylä, A. V. Priezzhev, M. Kinnunen, V. I. Pustovoy, M. Y. Kirillin, and A. P. Popov, editors, *Proceedings of SPIE*, volume **7022**, page 702202, Levi, Finland, 2007.

[60] M. Huang, F. Zhao, Ya Cheng, N. Xu, and Z. Xu. Origin of laser-induced near-subwavelength ripples: Interference between surface plasmons and incident laser. *ACS Nano*, **3**(12):4062–4070, 2009.

[61] J. F. Young, J. E. Sipe, J. S. Preston, and H. M. Van Driel. Laser-induced periodic surface damage and radiation remnants. *Appl. Phys. Lett.*, **41**(3):261–264, 1982.

[62] R. Yen, J. M. Liu, H. Kurz, and N. Bloembergen. Space-time resolved reflectivity measurements of picosecond laser-pulse induced phase transitions in (111) silicon surface layers. *Appl. Phys. A*, **27**(3):153–160, 1982.

[63] D. Puerto, M. Garcia-Lechuga, J. Hernandez-Rueda, A. Garcia-Leis, S. Sanchez-Cortes, J. Solis, and J. Siegel. Femtosecond laser-controlled self-assembly of amorphous-crystalline nanogratings in silicon. *Nanotechnology*, **27**(26):265602, 2016.

[64] M. Garcia-Lechuga, D. Puerto, Y. Fuentes-Edfuf, J. Solis, and J. Siegel. Ultrafast moving-spot microscopy: birth and growth of laser-induced periodic surface structures. *ACS Photon.*, **3**(10):1961–1967, 2016.

[65] J. Sládek, Y. Levy, T. J.-Y. Derrien, Z. Bryknar, and N. M. Bulgakova. Silicon surface patterning by regular stripes of laser-induced periodic surface structures. *Appl. Surf. Sci.*, **605**:154664, 2022.

[66] M. Birnbaum. Semiconductor surface damage produced by ruby lasers. *J. Appl. Phys.*, **36**(11):3688–3689, 1965.

[67] D. Dufft, A. Rosenfeld, S. K. Das, R. Grunwald, and J. Bonse. Femtosecond laser-induced periodic surface structures revisited: A comparative study on ZnO. *J. Appl. Phys.*, **105**(3):034908, 2009.

[68] K. Sokolowski-Tinten, A. Barty, S. Boutet, U. Shymanovich, *et al.* Short-pulse laser induced transient structure formation and ablation studied with time-resolved coherent XUV-scattering. In *AIP Conference Proceedings*, volume **1278**, pages 373–379, Santa Fe, (New Mexico), 2010.

[69] J. Z. P. Skolski, G. R. B. E. Römer, J. V. Obona, V. Ocelik, A. J. Huis In 'T Veld, and J. Th. M. De Hosson. Laser-induced periodic surface structures: Fingerprints of light localization. *Phys. Rev. B*, **85**(7):075320, 2012.

[70] J. Z. P. Skolski, G. R. B. E. Römer, J. Vincenc Obona, and A. J. Huis in 't Veld. Modeling laser-induced periodic surface structures: Finite-difference time-domain feedback simulations. *J. Appl. Phys.*, **115**(10):103102, 2014.

[71] G. D. Tsibidis, M. Barberoglou, P. A. Loukakos, E. Stratakis, and C. Fotakis. Dynamics of ripple formation on silicon surfaces by ultrashort laser pulses in subablation conditions. *Phys. Rev. B*, **86**(11):115316, 2012.

[72] J. Reif, O. Varlamova, S. Varlamov, and M. Bestehorn. The role of asymmetric excitation in self-organized nanostructure formation upon femtosecond laser ablation. *Appl. Phys. A*, **104**(3):969–973, 2011.

[73] S. Höhm, A. Rosenfeld, J. Krüger, and J. Bonse. Area dependence of femtosecond laser-induced periodic surface structures for varying band gap materials after double pulse excitation. *Applied Surface Science*, **278**:7–12, 2013.

[74] S. Höhm, A. Rosenfeld, J. Krüger, and J. Bonse. Femtosecond diffraction dynamics of laser-induced periodic surface structures on fused silica. *Appl. Phys. Lett.*, **102**(5):054102, 2013.

[75] A. Rudenko, A. Abou-Saleh, F. Pigeon, C. Mauclair, F. Garrelie, R. Stoian, and J. P. Colombier. High-frequency periodic patterns driven by non-radiative fields coupled with Marangoni convection instabilities on laser-excited metal surfaces. *Acta Mater.*, **194**:93–105, 2020.

[76] M. V. Shugaev, I. Gnilitskyi, N. M. Bulgakova, and L. V. Zhigilei. Mechanism of single-pulse ablative generation of laser-induced periodic surface structures. *Phys. Rev. B*, **96**(20):205429, 2017.

[77] I. Gnilitskyi, T. J.-Y. Derrien, Y. Levy, N. M. Bulgakova, T. Mocek, and L. Orazi. High-speed manufacturing of highly regular femtosecond laser-induced periodic surface structures: physical origin of regularity. *Sci. Rep.*, **7**(1):8485, 2017.

[78] A. Ruiz de la Cruz, R. Lahoz, J. Siegel, G. F. de la Fuente, and J. Solis. High speed inscription of uniform, large-area laser-induced periodic surface structures in Cr films using a high repetition rate fs laser. *Opt. Lett.*, **39**(8):2491–2494, 2014.

[79] R. D. Murphy, B. Torralva, D. P. Adams, and S. M. Yalisove. Polarization dependent formation of femtosecond laser-induced periodic surface structures near stepped features. *Appl. Phys. Lett.*, **104**(23):231117, 2014.

[80] J. Geng, L. Shi, X. Sun, W. Yan, and M. Qiu. Artificial seeds-regulated femtosecond laser plasmonic nanopatterning. *Laser Photon. Rev.*, **16**(11):2200232, 2022.

[81] A. Y. Vorobyev and Ch. Guo. Colorizing metals with femtosecond laser pulses. *Appl. Phys. Lett.*, **92**(4):041914, 2008.

[82] B. Dusser, Z. Sagan, H. Soder, N. Faure, J. P. Colombier, M. Jourlin, and E. Audouard. Controlled nanostructrures formation by ultra fast laser pulses for color marking. *Opt. Express*, **18**(3):2913–2924, 2010.

[83] A. Y. Vorobyev and Ch. Guo. Laser turns silicon superwicking. *Opt. Express*, **18**(7):6455–6460, 2010.

[84] X. Shen, L. Yang, S. Fan, Q. Yang, W. Wu, and B. Zhang. Colorful and superhydrophobic titanium surfaces textured by obliquely incident femtosecond laser induced micro/nano structures. *Opt. Commun.*, **466**:125687, 2020.

[85] A. H. A. Lutey, L. Gemini, L. Romoli, G. Lazzini, F. Fuso, M. Faucon, and R. Kling. Towards laser-textured antibacterial surfaces. *Sci. Rep.*, **8**(1):10112, 2018.

[86] E. Stratakis, J. Bonse, J. Heitz, J. Siegel, G. D. Tsibidis, E. Skoulas, A. Papadopoulos, A. Mimidis, A.-C. Joel, P. Comanns, J. Krüger, C. Florian, Y. Fuentes-Edfuf, J. Solis, and W. Baumgartner. Laser engineering of biomimetic surfaces. *Mater. Sci. Eng. R*, **141**:100562, 2020.

[87] J. Bonse, S. V. Kirner, M. Griepentrog, D. Spaltmann, and J. Krüger. Femtosecond laser texturing of surfaces for tribological applications. *Materials*, **11**(5):801, 2018.

[88] E. Maggiore, I. Mirza, D. Dellasega, M. Tommasini, and P. M. Ossi. Sliding on snow of AISI 301 stainless steel surfaces treated with ultra-short laser pulses. *Appl. Surf. Sci. Adv.*, **7**:100194, 2022.

[89] M. Kasischke, S. Maragkaki, S. Volz, A. Ostendorf, and E. L. Gurevich. Simultaneous nanopatterning and reduction of graphene oxide by femtosecond laser pulses. *Appl. Surf. Sci.*, **445**:197–203, 2018.

[90] K. A. Drogowska-Horna, I. Mirza, A. Rodriguez, P. Kovaříček, J. Sládek, T. J.-Y. Derrien, M. Gedvilas, G. Račiukaitis, O. Frank, N. M. Bulgakova, and M. Kalbáč. Periodic surface functional group density on graphene via laser-induced substrate patterning at Si/SiO2 interface. *Nano Res.*, **13**(9):2332–2339, 2020.

[91] E. Rebollar, M. Castillejo, and T. A. Ezquerra. Laser induced periodic surface structures on polymer films: From fundamentals to applications. *Eur. Polym. J.*, **73**:162–174, 2015.

[92] J. Schille, L. Schneider, S. Mauersberger, S. Szokup, S. Höhn, J. Pötschke, F. Reiß, E. Leidich, and U. Löschner. High-rate laser surface texturing for advanced tribological functionality. *Lubricants*, **8**(3):33, 2020.

[93] J. Eichstädt, G. R. B. E. Römer, and A. J. Huis in 't Veld. Determination of irradiation parameters for laser-induced periodic surface structures. *Appl. Surf. Sci.*, **264**:79–87, 2013.

[94] L. Wang, Q.-D. Chen, X.-W. Cao, R. Buividas, X. Wang, S. Juodkazis, and H.-B. Sun. Plasmonic nano-printing: large-area nanoscale energy deposition for efficient surface texturing. *Light Sci. Appl.*, **6**(12):e17112–e17112, 2017.

[95] M. Mezera and G. R. B. E. Römer. Model based optimization of process parameters to produce large homogeneous areas of laser-induced periodic surface structures. *Opt. Express*, **27**(5):6012–6029, 2019.

[96] X. Yu, Q. Zhang, D. Qi, S. Tang, S. Dai, P. Zhang, Y. Xu, and X. Shen. Femtosecond laser-induced large area of periodic structures on chalcogenide glass via twice laser direct-writing scanning process. *Opt. Laser Technol.*, **124**:105977, 2020.

[97] B. Öktem, I. Pavlov, S. Ilday, H. Kalaycıoğlu, A. Rybak, S. Yavaş, M. Erdoğan, and F. Ö. Ilday. Nonlinear laser lithography for indefinitely large-area nanostructuring with femtosecond pulses. *Nat. Photonics*, **7**(11):897–901, 2013.

[98] C. Lopez-Santos, D. Puerto, J. Siegel, M. Macias-Montero, C. Florian, J. Gil-Rostra, V. López-Flores, A. Borras, A. R. González-Elipe, and J. Solis. Anisotropic resistivity surfaces produced in ITO films by laser-induced nanoscale self-organization. *Adv. Opt. Mater.*, **9**(2):2001086, 2021.

[99] Y. Zhang, Q. Jiang, K. Cao, T. Chen, K. Cheng, S. Zhang, D. Feng, T. Jia, Z. Sun, and J. Qiu. Extremely regular periodic surface structures in a large area efficiently induced on silicon by temporally shaped femtosecond laser. *Photon. Res.*, **9**(5):839–847, 2021.

[100] E. Kifle, P. Loiko, C. Romero, J. R. Vázquez de Aldana, *et al.* Fs-laser-written erbium-doped double tungstate waveguide laser. *Opt. Express*, **26**(23):30826–30836, 2018.

[101] K. Sugioka, Y. Cheng, and K. Midorikawa. Three-dimensional micromachining of glass using femtosecond laser for lab-on-a-chip device manufacture. *Appl. Phys. A*, **81**(1):1–10, 2005.

[102] O. Tokel, A. Turnali, G. Makey, P. Elahi, *et al.* In-chip microstructures and photonic devices fabricated by nonlinear laser lithography deep inside silicon. *Nat. Photonics*, **11**(10):639–645, 2017.

[103] N. M. Bulgakova, V. P. Zhukov, A. R. Collins, D. Rostohar, T. J.-Y. Derrien, and T. Mocek. How to optimize ultrashort pulse laser interaction with glass surfaces in cutting regimes? *Appl. Surf. Sci.*, **336**:364–374, 2015.

[104] I. M. Burakov, N. M. Bulgakova, R. Stoian, A. Mermillod-Blondin, E. Audouard, A. Rosenfeld, A. Husakou, and I. V. Hertel. Spatial distribution of refractive index variations induced in bulk fused silica by single ultrashort and short laser pulses. *J. Appl. Phys.*, **101**(4):043506, 2007.

[105] K. Sugioka. Progress in ultrafast laser processing and future prospects. *Nanophotonics*, **6**(2):393–413, 2017.

[106] S. M. Eaton, H. Zhang, Peter R. Herman, F. Yoshino, L. Shah, J. Bovatsek, and Alan Y. A. Heat accumulation effects in femtosecond laser-written waveguides with variable repetition rate. *Opt. Express*, **13**(12):4708–4716, 2005.

[107] M. Shimizu, M. Sakakura, M. Ohnishi, Y. Shimotsuma, T. Nakaya, K. Miura, and K. Hirao. Mechanism of heat-modification inside a glass after irradiation with high-repetition rate femtosecond laser pulses. *J. Appl. Phys.*, **108**(7):073533, 2010.

[108] T. Gertus, A. Michailovas, K. Michailovas, and V. Petrauskienė. Laser beam shape converter using spatially variable waveplate made by nanogratings inscription in fused silica. In *Laser resonators, microresonators, and beam control XVII*, volume **9343**, page 93431S, San Francisco, California, United States, 2015. SPIE.

[109] R. Taylor, C. Hnatovsky, and E. Simova. Applications of femtosecond laser induced self-organized planar nanocracks inside fused silica glass. *Laser Photonics Rev.*, **2**(1-2):26–46, 2008.

[110] N. Goodfriend, J. Sládek, M. Flimelová, W. Marine, I. Mirza, and N. M Bulgakova. Laserová laboratoř zabývající se studiem nových režimů ozařování materiálů v rámci centra HiLASE. *Čs. čas. fyz.*, **70**(6):417–425, 2020.

[111] J. Sládek, K. Hlinomaz, I. Mirza, Y. Levy, T. J.-Y. Derrien, M. Cimrman, S. S. Nagisetty, J. Čermák, T. H. Stuchlíková, J. Stuchlík, and N. M. Bulgakova. Highly regular LIPSS on thin molybdenum films: Optimization and generic criteria. *Materials*, **16**(7):2883, 2023.

[112] A. E. Siegman. *Lasers*. University Science Books, Mill Valley, California, 1986.

[113] A. San-Blas, M. Martinez-Calderon, E. Granados, M. Gómez-Aranzadi, A. Rodríguez, and S.M. Olaizola. LIPSS manufacturing with regularity control through laser wavefront curvature. *Surf. Interfaces*, **25**:101205, 2021.

[114] J. M. Liu. Simple technique for measurements of pulsed Gaussian-beam spot sizes. *Opt. Lett.*, **7**(5):196–198, 1982.

[115] G. Fibich and A. L. Gaeta. Critical power for self-focusing in bulk media and in hollow waveguides. *Opt. Lett.*, **25**(5):335–337, 2000.

[116] A. Couairon and A. Mysyrowicz. Femtosecond filamentation in transparent media. *Phys. Rep.*, **441**(2-4):47–189, 2007.

[117] A. V. Smith and B. T. Do. Bulk and surface laser damage of silica by picosecond and nanosecond pulses at 1064 nm. *Appl. Opt.*, **47**(26):4812–4832, 2008.

[118] A. Couairon, L. Sudrie, M. Franco, B. Prade, and A. Mysyrowicz. Filamentation and damage in fused silica induced by tightly focused femtosecond laser pulses. *Phys. Rev. B*, **71**(12):125435, 2005.

[119] J. H. Marburger. Self-focusing: theory. *Prog. Quantum Electron.*, **4**(1):35–110, 1975.

[120] V. N. Lednev, M. N. Filippov, A. F. Bunkin, and S. M. Pershin. Laser ablation comparison by picosecond pulses train and nanosecond pulse. *Laser Phys. Lett.*, **12**(12):126001, 2015.

[121] J. Winter, M. Spellauge, J. Hermann, C. Eulenkamp, H. P. Huber, and M. Schmidt. Ultrashort single-pulse laser ablation of stainless steel, aluminium, copper and its dependence on the pulse duration. *Opt. Express*, **29**(10):14561–14581, 2021.

[122] D. Bachman, Z. Chen, R. Fedosejevs, Y. Y. Tsui, and V. Van. Threshold for permanent refractive index change in crystalline silicon by femtosecond laser irradiation. *Appl. Phys. Lett.*, **109**(9):091901, 2016.

[123] C. Florian, D. Fischer, K. Freiberg, M. Duwe, M. Sahre, S. Schneider, A. Hertwig, J. Krüger, M. Rettenmayr, U. Beck, A. Undisz, and J. Bonse. Single femtosecond laser-pulse-induced superficial amorphization and re-crystallization of silicon. *Materials*, **14**(7):1651, 2021.

[124] S. Hermann, N.-P. Harder, R. Brendel, D. Herzog, and H. Haferkamp. Picosecond laser ablation of $SiO_2$ layers on silicon substrates. *Appl. Phys. A*, **99**(1):151–158, 2010.

[125] C. W. Carr, H. B. Radousky, and S. G. Demos. Wavelength dependence of laser-induced damage: Determining the damage initiation mechanisms. *Phys. Rev. Lett.*, **91**(12):127402, 2003.

[126] J. H. Campbell, F. Rainer, M. R. Kozlowski, C. R. Wolfe, I. M. Thomas, and F. P. Milanovich. Damage resistant optics for a megajoule solid state laser. In H. E. Bennett, L. L. Chase, A. H. Guenther, B. E. Newnam, and M. J. Soileau, editors, *Proceedings of SPIE*, volume **1441**, pages 444–456, Boulder, CO, 1991.

[127] B. C. Stuart, M. D. Feit, A. M. Rubenchik, B. W. Shore, and M. D. Perry. Laser-induced damage in dielectrics with nanosecond to subpicosecond pulses. *Phys. Rev. Lett.*, **74**(12):2248–2251, 1995.

[128] M. Mero, J. Liu, W. Rudolph, D. Ristau, and K. Starke. Scaling laws of femtosecond laser pulse induced breakdown in oxide films. *Phys. Rev. B*, **71**(11):115109, 2005.

[129] J. Hrabovský, Ch. Liberatore, I. Mirza, J. Sládek, J. Beránek, A. V. Bulgakov, and N. M. Bulgakova. Surface structuring of kapton polyimide with femtosecond and picosecond IR laser pulses. *Interfacial Phenom. Heat Transf.*, **7**(2):113–121, 2019.

[130] R. House, J. Bettis, and A. Guenther. Surface roughness and laser damage threshold. *IEEE J. Quantum Electron.*, **13**(5):361–363, 1977.

[131] N. Bloembergen. Role of cracks, pores, and absorbing inclusions on laser induced damage threshold at surfaces of transparent dielectrics. *Appl. Opt.*, **12**(4):661–664, 1973.

[132] J. Thorstensen and S. E. Foss. Temperature dependent ablation threshold in silicon using ultrashort laser pulses. *J. Appl. Phys.*, **112**(10):103514, 2012.

[133] J. Sládek and I. Mirza. Laser induced damage threshold of silicon with native and artificial $SiO_2$ layer. *MM Sci. J.*, **2019**(05):3579–3583, 2019.

[134] J. Xu, Y. Cheng, and K. Sugioka. Optics for beam shaping in laser processing. In K. Sugioka, editor, *Handbook of Laser Micro- and Nano-Engineering*, pages 527–543. Springer International Publishing, Cham, 2021.

[135] G. Račiukaitis, E. Stankevičius, P. Gečys, M. Gedvilas, Ch. Bischoff, E. Jäger, U. Umhofer, and F. Volklein. Laser processing by using diffractive optical laser beam shaping technique. *J. Laser Micro Nanoeng.*, **6**(1):37–43, 2011.

[136] J. Choi, W. Choi, Y.-G. Shin, S. Han, K.-S. Kim, and S.-H. Cho. Enhancement periodic regularity of surface nano ripple structures on Si wafer using a square shaped flat-top beam femtosecond NIR laser. *Appl. Phys. A*, **128**(1):46, 2022.

[137] Q. Zhan. Cylindrical vector beams: from mathematical concepts to applications. *Adv. Opt. Photon.*, **1**(1):1–57, 2009.

[138] J. Baltrukonis, O. Ulčinas, S. Orlov, and V. Jukna. Void and micro-crack generation in transparent materials with high-energy first-order vector Bessel beam. *J. Opt. Soc. Am. B*, **37**(7):2121–2127, 2020.

[139] A. Möhl, S. Kaldun, C. Kunz, F. A. Müller, U. Fuchs, and S. Gräf. Tailored focal beam shaping and its application in laser material processing. *J. Laser Appl.*, **31**(4):042019, 2019.

[140] J. Adamonis, A. Aleknavičius, K. Michailovas, S. Balickas, V. Petrauskienė, T. Gertus, and A. Michailovas. Implementation of a SVWP-based laser beam shaping technique for generation of 100-mJ-level picosecond pulses. *Appl. Opt.*, **55**(28):8007–8015, 2016.

[141] Workshop of photonics. S-waveplate: Radial polarization converter, 2022.

[142] K. S. Youngworth and T. G Brown. Focusing of high numerical aperture cylindrical-vector beams. *Opt. Express*, **7**(2):77–87, 2000.

[143] L. A. Moore and Ch. M. Smith. Fused silica as an optical material. *Opt. Mater. Express*, **12**(8):3043–3059, 2022.

[144] E. D. Palik. *Handbook of optical constants of solids*. Academic Press, 1985.

[145] D. Bäuerle. *Laser processing and chemistry*. Springer, Heidelberg ; New York, fourth edition edition, 2011.

[146] Ch. Brandmaier, K. R. Spring, and M. W. Davidson. Reflected light DIC microscopy, 2022.

[147] J. Bonse, K.-W. Brzezinka, and A. J. Meixner. Modifying single-crystalline silicon by femtosecond laser pulses: an analysis by micro Raman spectroscopy, scanning laser microscopy and atomic force microscopy. *Appl. Surf. Sci.*, **221**(1-4):215–230, 2004.

[148] M. Zukerstein, J. Hrabovský, J. Sládek, I. Mirza, Y. Levy, and N. M. Bulgakova. Formation of tubular structures and microneedles on silicon surface by doughnut-shaped ultrashort laser pulses. *Appl. Surf. Sci.*, **592**:153228, 2022.

[149] G. Račiukaitis, M Brikas, and M. Gečys, P.and Gedvilas. Accumulation effects in laser ablation of metals with high-repetition-rate lasers. In Claude R. Phipps, editor, *Proceedings of SPIE*, page 70052L, Taos, NM, 2008. SPIE.

[150] Z. Sun, M. Lenzner, and W. Rudolph. Generic incubation law for laser damage and ablation thresholds. *J. Appl. Phys.*, **117**(7):073102, 2015.

[151] G. F. B. Almeida, L. K. Nolasco, G. R. Barbosa, A. Schneider, A. Jaros, I. Manglano Clavero, C. Margenfeld, A. Waag, T. Voss, and C. R. Mendonça. Incubation effect during laser micromachining of GaN films with femtosecond pulses. *J. Mater. Sci: Mater. Electron.*, **30**(18):16821–16826, 2019.

[152] X. Sedao, C. Maurice, F. Garrelie, J.-P. Colombier, S. Reynaud, R. Quey, and F. Pigeon. Influence of crystal orientation on the formation of femtosecond laser-induced periodic surface structures and lattice defects accumulation. *Appl. Phys. Lett.*, **104**(17):171605, 2014.

[153] M. Gertsvolf, H. Jean-Ruel, P. P. Rajeev, D. D. Klug, D. M. Rayner, and P. B. Corkum. Orientation-dependent multiphoton ionization in wide band gap crystals. *Phys. Rev. Lett.*, **101**(24):243001, 2008.

[154] X. Li, W. Rong, L. Jiang, K. Zhang, C. Li, Q. Cao, G. Zhang, and Y. Lu. Generation and elimination of polarization-dependent ablation of cubic crystals by femtosecond laser radiation. *Opt. Express*, **22**(24):30170–30176, 2014.

[155] L. Jiang, W. Han, X. Li, Q. Wang, F. Meng, and Y. Lu. Crystal orientation dependence of femtosecond laser-induced periodic surface structure on (100) silicon. *Opt. Lett.*, **39**(11):3114–3117, 2014.

[156] M. Kozák, T. Otobe, M. Zukerstein, F. Trojánek, and P. Malý. Anisotropy and polarization dependence of multiphoton charge carrier generation rate in diamond. *Phys. Rev. B*, **99**(10):104305, 2019.

[157] F. Theberge and S. L. Chin. Enhanced ablation of silica by the superposition of femtosecond and nanosecond laser pulses. *Appl. Phys. A*, **80**(7):1505–1510, 2005.

[158] S. Zoppel, R. Merz, J. Zehetner, and G.A. Reider. Enhancement of laser ablation yield by two color excitation. *Appl. Phys. A*, **81**(4):847–850, 2005.

[159] W. Zhao, W. Wang, X. Mei, G. Jiang, and B. Liu. Investigations of morphological features of picosecond dual-wavelength laser ablation of stainless steel. *Opt. Laser Technol.*, **58**:94–99, 2014.

[160] K. Sugioka, T. Akane, K. Obata, K. Toyoda, and K. Midorikawa. Multiwavelength excitation processing using $F_2$ and KrF excimer lasers for precision microfabrication of hard materials. *Appl. Surf. Sci.*, 197-198:814–821, 2002.

[161] T. Q. Jia, H. X. Chen, M. Huang, F. L. Zhao, J. R. Qiu, R. X. Li, Z. Z. Xu, X. K. He, J. Zhang, and H. Kuroda. Formation of nanogratings on the surface of a ZnSe crystal irradiated by femtosecond laser pulses. *Phys. Rev. B*, **72**(12):125429, 2005.

[162] S. Höhm, M. Herzlieb, A. Rosenfeld, J. Krüger, and J. Bonse. Dynamics of the formation of laser-induced periodic surface structures (LIPSS) upon femtosecond two-color double-pulse irradiation of metals, semiconductors, and dielectrics. *Appl. Surf. Sci.*, **374**:331–338, 2016.

[163] K. Gaudfrin, J. Lopez, L. Gemini, M. Delaigue, C. Hönninger, R. Kling, and G. Duchateau. Fused silica ablation by double ultrashort laser pulses with dual wavelength and variable delays. *Opt. Express*, **30**(22):40120–40135, 2022.

[164] J.-M. Guay, A. Villafranca, F. Baset, K. Popov, L. Ramunno, and V. R. Bhardwaj. Polarization-dependent femtosecond laser ablation of poly-methyl methacrylate. *New J. Phys.*, **14**(8):085010, 2012.

[165] S. Zhou, R. Li, S. Jiang, and M. Huang. Hybrid periodic microstructures fabricated on chromium metal surface using ns-DLIP scanning combined with LIPSS. *Opt. Laser Technol.*, **153**:108261, 2022.

[166] M. Huang, Y. Cheng, F. Zhao, and Z. Xu. The significant role of plasmonic effects in femtosecond laser-induced grating fabrication on the nanoscale. *Annalen der Phys.*, **525**(1-2):74–86, 2013.

[167] S. Hou, Y. Huo, P. Xiong, Y. Zhang, S. Zhang, T. Jia, Z. Sun, J. Qiu, and Z. Xu. Formation of long- and short-periodic nanoripples on stainless steel irradiated by femtosecond laser pulses. *J. Phys. D: Appl. Phys.*, **44**(50):505401, 2011.

[168] X. Zhang, L. Zhang, S. Mironov, R. Xiao, L. Guo, and T. Huang. Effect of crystallographic orientation on structural response of silicon to femtosecond laser irradiation. *Appl. Phys. A*, **127**(3):196, 2021.

[169] K. Bronnikov, A. Dostovalov, A. Cherepakhin, E. Mitsai, A. Nepomniaschiy, S. A. Kulinich, A. Zhizhchenko, and A. Kuchmizhak. Large-scale and localized laser crystallization of optically thick amorphous silicon films by near-IR femtosecond pulses. *Materials*, **13**(22):5296, 2020.

[170] Y. Fuentes-Edfuf, M. Garcia-Lechuga, D. Puerto, C. Florian, A. Garcia-Leis, S. Sanchez-Cortes, J. Solis, and J. Siegel. Fabrication of amorphous micro-ring arrays in crystalline silicon using ultrashort laser pulses. *Appl. Phys. Lett.*, **110**(21):211602, 2017.

[171] S. Höhm, M. Herzlieb, A. Rosenfeld, J. Krüger, and J. Bonse. Formation of laser-induced periodic surface structures on fused silica upon two-color double-pulse irradiation. *Appl. Phys. Lett.*, **103**(25):254101, 2013.

[172] D. Ashkenasi, A. Rosenfeld, H. Varel, M. Wähmer, and E. E. B Campbell. Laser processing of sapphire with picosecond and sub-picosecond pulses. *Appl. Surf. Sci.*, **120**(1-2):65–80, 1997.

[173] R. Wagner and J. Gottmann. Sub-wavelength ripple formation on various materials induced by tightly focused femtosecond laser radiation. *J. Phys.: Conf. Ser.*, **59**:333–337, 2007.

[174] I. Mirza, N. M. Bulgakova, J. Tomáštík, V. Michálek, O. Haderka, L. Fekete, and T. Mocek. Ultrashort pulse laser ablation of dielectrics: Thresholds, mechanisms, role of breakdown. *Sci. Rep.*, **6**(1):39133, 2016.

[175] S. Schwarz, C. Rung, S. Esen, and R. Hellmann. Surface plasmon polariton triggered generation of 1D-low spatial frequency LIPSS on fused silica. *Appl. Sci.*, **8**(9):1624, 2018.

[176] S. Gräf, C. Kunz, S. Engel, T. J.-Y. Derrien, and F. Müller. Femtosecond laser-induced periodic surface structures on fused silica: The impact of the initial substrate temperature. *Materials*, **11**(8):1340, 2018.

[177] A. Sikora, S. Nourry, M. Faucon, B. Chassagne, R. Kling, and G. Mincuzzi. Role of the intensity profile in femtosecond laser surface texturing: An experimental study. *Appl. Surf. Sci. Adv.*, **6**:100136, 2021.

[178] S. K. Das, K. Dasari, A. Rosenfeld, and R. Grunwald. Extended-area nanostructuring of $TiO_2$ with femtosecond laser pulses at 400 nm using a line focus. *Nanotechnology*, **21**(15):155302, 2010.

[179] M. S. Sidhu, P. Munjal, and K. P. Singh. High-fidelity large area nano-patterning of silicon with femtosecond light sheet. *Appl. Phys. A*, **124**(1):46, 2018.

[180] K. Cao, L. Chen, H. Wu, J. Liu, K. Cheng, Y. Li, Y. Xia, Ch. Feng, S. Zhang, D. Feng, Z. Sun, and T. Jia. Large-area commercial-grating-quality subwavelength periodic ripples on silicon efficiently fabricated by gentle ablation with femtosecond laser interference via two cylindrical lenses. *Opt. Laser Technol.*, **131**:106441, 2020.

[181] J. Huang, L. Jiang, X. Li, Q. Wei, Z. Wang, B. Li, L. Huang, A. Wang, Z. Wang, M. Li, L. Qu, and Y. Lu. Cylindrically focused nonablative femtosecond laser processing of long-range uniform periodic surface structures with tunable diffraction efficiency. *Adv. Opt. Mater.*, **7**(20):1900706, 2019.

[182] X. Li, R. Li, Z. Yu, J. Xing, W. Kong, Y. Wang, and J. Yang. Deepening of nanograting structures on Si by a two-step laser spatial-selective amorphization strategy combined with chemical etching. *Appl. Surf. Sci.*, **589**:152965, 2022.

[183] D. Grojo, S. Leyder, P. Delaporte, W. Marine, M. Sentis, and O. Utéza. Long-wavelength multiphoton ionization inside band-gap solids. *Phys. Rev. B*, **88**(19):195135, 2013.

[184] E. Mareev, A. Pushkin, E. Migal, K. Lvov, S. Stremoukhov, and F. Potemkin. Single-shot femtosecond bulk micromachining of silicon with mid-IR tightly focused beams. *Sci. Rep.*, **12**(1):7517, 2022.

[185] M. Mori, Y. Shimotsuma, T. Sei, M. Sakakura, K. Miura, and H. Udono. Tailoring thermoelectric properties of nanostructured crystal silicon fabricated by infrared femtosecond laser direct writing. *Phys. Status Solidi A*, **212**(4):715–721, 2015.

[186] E. V. Zavedeev, V. V. Kononenko, and V. I. Konov. Delocalization of femtosecond laser radiation in crystalline Si in the mid-IR range. *Laser Phys.*, **26**(1):016101, 2016.

[187] A. Mouskeftaras, A. V. Rode, R. Clady, M. Sentis, O. Utéza, and D. Grojo. Self-limited underdense microplasmas in bulk silicon induced by ultrashort laser pulses. *Appl. Phys. Lett.*, **105**(19):191103, 2014.

[188] Z. Püspöki, M. Storath, D. Sage, and M. Unser. Transforms and operators for directional bioimage analysis: A survey. In *Focus on bio-image informatics*, volume **219**, pages 69–93. Springer International Publishing, Cham, Switzerland, 2016.

[189] C. A. Schneider, W. S. Rasband, and K. W. Eliceiri. NIH Image to ImageJ: 25 years of image analysis. *Nat. Methods*, **9**(7):671–675, 2012.

# List of author's publications

Below, the reader can find the list of publications in indexed journals and conference proceedings, authored or co-authored by the author during his doctoral studies. The publications are listed in chronological order.

J. Hrabovský, Ch. Liberatore, I. Mirza, J. Sládek, J. Beránek, A. V. Bulgakov, and N. M. Bulgakova. Surface structuring of kapton polyimide with femtosecond and picosecond IR laser pulses. *Interfacial Phenomena and Heat Transfer* **7**(2):113–21, 2019. (JCI = 0.17, cited: 4)

J. Sládek, and I. Mirza. Laser induced damage threshold of silicon with native and artificial $SiO_2$ layer. *MM Science Journal*, **2019**(5):3579–83. 2019. (JCI = 0.16, cited: 5)

K. A. Drogowska-Horna, I. Mirza, A. Rodriguez, P. Kovaříček, J. Sládek, T. J.-Y. Derrien, M. Gedvilas, *et al.* Periodic surface functional group density on graphene via laser-induced substrate patterning at Si/SiO2 Interface. *Nano Research* **13**(9):2332–39, 2020. (IF = 10.269, cited: 12)

M. Zukerstein, J. Hrabovský, J. Sládek, I. Mirza, Y. Levy, and N. M. Bulgakova. Formation of tubular structures and microneedles on silicon surface by doughnut-shaped ultrashort laser pulses. *Applied Surface Science*, **592**:153228, 2022. (IF = 7.392, cited: 7)

J. Sládek, Y. Levy, T.J.-Y. Derrien, Z. Bryknar, and N. M. Bulgakova. Silicon surface patterning by regular stripes of laser-induced periodic surface structures. *Applied Surface Science* **605**:154664, 2022. (IF = 7.392, cited: 3)

J. Sládek, K. Hlinomaz, I. Mirza, Y. Levy, T. J.-Y. Derrien, M. Cimrman, S. S. Nagisetty, *et al.* Highly regular LIPSS on thin molybdenum films: Optimization and generic criteria. *Materials* **16**(7):2883, 2023. (IF = 3.748, cited: 0)

### Publications in conference proceedings

N. M. Bulgakova, V. P. Zhukov, J. Sládek, I. Mirza, and A. V. Bulgakov. Dual wavelength laser excitation of bandgap materials: challenges for efficient energy coupling. In Conference on Lasers and Electro-Optics, STh1H.4. Washington, Optica Publishing Group, 2020. (cited: 1)

I. Mirza, K.A. Drogowska, A. Rodriguez, P. Kovaříček, J. Sládek, T. J.-Y. Derrien, *et al.* Periodic surface functional group density on graphene induced by pulsed laser patterning of SiO2/Si substrate. In Conference Proceedings - Lasers and Electro-Optics Society Annual Meeting-LEOS, 9192282, SW3G.4, Piscataway, IEEE, 2020.